

Alkaline Earth Element Partitioning in Simplified Magmatic Systems

Thesis by

Sarah Ann Miller

In Partial Fulfillment of the Requirements

for the Degree of

Doctor of Philosophy

California Institute of Technology

Pasadena, California

2007

(Defended December 6, 2006)

© 2007

Sarah Ann Miller

All Rights Reserved

Acknowledgments

First and foremost, I would like to thank my research advisors Paul Asimow and Don Burnett for their guidance, support, and mentorship during my time at Caltech. Their continued enthusiasm for the fundamental nature of the work we were doing was inspiring and motivating. I also benefited from their willingness to undertake the more adventurous project of radium partitioning, which required more attention to safety considerations than the typical geoscience experimental investigation. Thanks to my thesis committee (Paul Asimow, Don Burnett, Ed Stolper, George Rossman, and John Eiler) for attending TAC meetings over the years and their casting sharp eyes over this thesis document. I am grateful to George Rossman, my academic advisor, for always keeping his office and lab doors open for questions of all sorts and generously making his analytical equipment available. I would also like to extend a special note of appreciation to George and John Eiler; it was a pleasure to TA the classes they taught and observe their distinctive, effective pedagogical styles. They deserve recognition not only for engaging teaching but their behind-the-scenes availability and support of the TAs with whom they work. Thank you to all the attendees of Petrology Reading Group over the years for the memories-watch out for sediments on the Earth's core and guard your papers closely if you don't remember what is in them!

Julie Heather was a constant source of experimental and analytical know-how; I am also thankful for the expertise shared by Ma Chi, John Beckett, Mike Baker, Jed Mosenfelder, Harold Connolly, Jr., Liz Miura Boyd, Caroline Seaman, and Lindsey Hedges. Haick Issaian and André Jefferson in the Safety Office went above and beyond

the call of duty to help handle and characterize the radium source material. By the same token, I am grateful to our collaborators Ian Hutcheon and Doug Phinney at Lawrence Livermore National Laboratory for hosting the radium analytical work. Thanks also go to Ric in the Machine Shop, the Bio stockroom, and the Carpentry Shop. Jan Haskell, Carolyn Porter, Marcia Hudson, Michelle Medley, and Terry Gennaro made getting things done within the division infinitely easier.

A special thank you goes out to all the friends I made at Caltech, both inside and out of GPS, during my time here and who know who they are. I also thank my family and Nathan Lamarre-Vincent, husband and new father extraordinaire, for his unflagging confidence and support as well as his strength of character, raw determination, keen scientific mind, generous spirit, and sense of humor, all of which are a constant source of inspiration to me.

Nothing is written.

-Lawrence of Arabia (1962)

Abstract

Trace element distributions between mineral and melt phases have proven to be important recorders of igneous differentiation histories, but this utility depends on thorough understanding of their partitioning behavior. We propose a theory for crystal-melt trace element partitioning that considers the energetic consequences of crystal-lattice strain, of multi component major-element silicate liquid mixing, and of trace element activity coefficients in melts. We demonstrate application of the theory using newly determined partition coefficients for Ca, Mg, Sr, and Ba between pure anorthite and seven CMAS liquid compositions at 1330 °C and 1 atm. By selecting a range of melt compositions in equilibrium with a common crystal composition at equal liquidus temperature and pressure, we have isolated the contribution of melt composition to divalent trace element partitioning in this simple system. The partitioning data are fit to Onuma curves with parameterizations that can be thermodynamically rationalized in terms of the melt major element activity product ($a_{\text{Al}_2\text{O}_3} a_{\text{SiO}_2}^2$) and lattice strain theory modeling. Residuals between observed partition coefficients and the lattice strain plus major oxide melt activity model are then attributed to non-ideality of trace constituents in the liquids. The activity coefficients of the trace species in the melt are found to vary systematically with composition. Accounting for the major and trace element thermodynamics in the melt allows a good fit in which the parameters of the crystal lattice strain model are independent of melt composition.

We also present the first experimental measurements of mineral-melt radium partitioning. Ion probe analyses of coexisting anorthite and CMAS glass phases produce

a molar $D_{\text{Ra}} = 0.040 \pm 0.006$ and $D_{\text{Ra}}/D_{\text{Ba}} = 0.23$ at 1400 °C and 1 atm. Our results indicate that lattice strain partitioning models fit the divalent (Ca, Sr, Ba, Ra) partition coefficient data of this study well, supporting previous work on crustal melting and magma chamber dynamics that has relied on such models to approximate radium partitioning behavior in the absence of experimentally determined values.

Table of Contents

| | | |
|------------|---|------|
| | Acknowledgments..... | iii |
| | Abstract..... | vi |
| | Table of Contents..... | viii |
| | List of Figures and Tables..... | ix |
| Chapter 1 | Introduction | 1 |
| Chapter 2 | Determination of Melt Influence on Divalent Element Partitioning between Anorthite and CMAS Melts | 6 |
| Chapter 3 | Reoptimization of the Berman (1983) CMAS Liquidus Model in Anorthite Phase Space | 51 |
| Chapter 4 | Experimental Techniques for Radium Partitioning Measurements | 64 |
| Chapter 5 | Experimental Study of Radium Partitioning between Anorthite and Melt at 1 atm | 86 |
| Chapter 6 | Future Work | 99 |
| Appendix 1 | Experimental Design | 103 |
| Appendix 2 | Crystal Selection | 112 |
| Appendix 3 | Crystal Growth Dynamics | 123 |
| Appendix 4 | CAI Composition: Divalent Element Partitioning and Cathodoluminescence | 147 |
| Appendix 5 | Anorthite-Melt Partitioning and Varying Melt Silica Contents | 158 |
| Appendix 6 | Thesis Run Table | 167 |
| | References | 170 |

Figures and Tables

| Chapter 2 | | Page |
|------------------|--|-------------|
| Figure 2.1 | Study liquid compositions within the CMAS tetrahedron | 12 |
| Table 2.1 | Glass compositions from controlled cooling experiments | 23 |
| Table 2.2 | Anorthite compositions from controlled cooling experiments | 23 |
| Figure 2.2 | Back-scattered electron image of representative sample 2b-3-2 | 24 |
| Table 2.3 | Normalized CMAS melt compositions and alkaline earth element partition coefficients | 26 |
| Figure 2.3 | Relationship between $D_{\text{MgO}}^{\text{m}}$ and melt activity product for Mg^{2+} partitioning onto IV and VIII anorthite coordination sites | 31 |
| Figure 2.4 | Prediction of Mg fractionation between IV (T) and VIII (M) sites in anorthite | 32 |
| Figure 2.5 | Comparison of model parameterizations to molar partition coefficients between anorthite and seven melt compositions | 36 |
| Table 2.4 | Comparison of measured data with model parameterization predictions of anorthite/melt partition coefficients | 39 |
| Figure 2.6 | Calculated melt γ_{BaO} and γ_{SrO} values plotted with γ_{CaO} for the seven liquid compositions | 42 |
| Figure 2.7 | Exchange partition coefficients for Ca-Sr, Ca-Ba, and Sr-Ba. | 44 |
| Figure 2.8 | Relationship between D^{m} and optical basicity | 46 |

| Chapter 3 | | Page |
|----------------------|---|-------------|
| Table 3.1 | Anorthite and liquid oxide component standard state properties and heat capacity equation coefficients | 56 |
| Figure 3.1 | Literature anorthite-CMAS melt liquidus data | 58 |
| Figure 3.2 | Reduction of $(\Delta T_L)^2$ as a function of Margules parameter adjustments made during reoptimization | 60 |
| Table 3.2 | Reoptimized Margules parameters for a portion of the anorthite liquidus field in CMAS | 61 |
| Figure 3.3 | Comparison of (ΔT_L) versus melt X CaO for experimental and predicted anorthite liquidus temperatures before and after reoptimization | 62 |
| Chapter 4 | | |
| Figure 4.1 | ^{238}U decay series ending in stable ^{206}Pb | 66 |
| Figure 4.2 | Flow line configuration for activated charcoal heating pre-treatment under vacuum prior to sample runs in furnace | 76 |
| Figure 4.3 | Flow line for ^{222}Rn removal from gas exiting furnace | 78 |
| Figure 4.4 | Geiger counter and γ -spectrometry measurement of post-experiment ^{226}Ra activity with furnace thermal profile | 81 |
| Chapter 5 | | |
| Figure 5.1 | Back-scattered electron image of experiment 2-1*-Ra | 89 |
| Figure 5.2 | Ion probe mass scan over region surrounding mass 226 for glass of radium-free and radium-bearing samples | 91 |
| Table 5.1 | Starting material, standard, radium-free, and radium-bearing compositions and alkaline earth element partition coefficients | 95 |
| Figure 5.3 | Onuma curve (D vs. ionic radius) of Ca, Sr, Ba, and Ra molar partition coefficients | 97 |

Appendix 1

| | | |
|-------------|---|-----|
| Figure A1.1 | Crystals grown isothermally and by dynamic crystallization | 103 |
| Figure A1.2 | Controlled cooling path of dynamic crystallization experiments | 104 |
| Table A1.1 | Comparison of three CMAS2 anorthite/melt molar partition coefficient data sets for Ba, Sr, and Be | 106 |
| Figure A1.3 | Anorthite/silicate melt divalent element partitioning of tetrahedral and octahedral coordination site occupancy | 109 |
| Figure A1.4 | Major element rim to rim CMAS2b crystal traverses | 111 |

Appendix 2

| | | |
|-------------|--|-----|
| Figure A2.1 | BSE imaging of locations of CMAS2b crystal 2-D grid analyses | 112 |
| Figure A2.2 | Sample 2b-1-2: MgO, SrO, BaO maps (wt. %) | 114 |
| Figure A2.3 | Sample 2b-2-2: MgO, SrO, BaO maps (wt. %) | 115 |
| Figure A2.4 | Sample 2b-3-2: MgO, SrO, BaO maps (wt. %) | 116 |
| Figure A2.5 | Sample 2b-4-2: MgO, SrO, BaO maps (wt. %) | 117 |
| Figure A2.6 | Sample 2b-5-2: MgO, SrO, BaO maps (wt. %) | 118 |
| Figure A2.7 | Sample 2b-6-2: MgO, SrO, BaO maps (wt. %) | 119 |
| Figure A2.8 | Sample 2b-7-2: MgO, SrO, BaO maps (wt. %) | 120 |
| Figure A2.9 | Transects summarizing zoning trends in the A2.2 crystals | 122 |

Appendix 3

| | | |
|--------------|---|-----|
| Figure A3.1 | BSE crystal images quenched at three intermediate time points | 123 |
| Table A3.1 | Starting compositions of glasses fused for three hours | 124 |
| Table A3.2 | CMAS glass compositions at three intermediate time steps | 125 |
| Table A3.3 | Final melt compositions after 96.5 hours | 125 |
| Figure A3.2 | Crystal fraction increases as a function of time and temperature | 126 |
| Figure A3.3 | Heterogeneity index (HI) for melt major element oxide contents | 129 |
| Table A3.4 | Melt Al ₂ O ₃ variations relative to analytical error | 130 |
| Figure A3.4 | BSE images of melt grid locations for runs quenched at 67 hours | 132 |
| Figure A3.5 | Sample 2b-1-5: grid melt maps of MgO, SrO, and BaO data | 133 |
| Figure A3.6 | Sample 2b-4-5: grid melt maps of MgO, SrO, and BaO data | 134 |
| Figure A3.7 | Sample 2b-7-5: grid melt maps of MgO, SrO, and BaO data | 135 |
| Table A3.5 | JEOL JXA-8200 and JEOL 733 electron microprobe analytical error for MgO, SrO, and BaO | 137 |
| Figure A3.8 | BSE imaging of 2-D grid areas for 20 °C/hr cooling experiments | 137 |
| Figure A3.9 | Sample 2b-1-7: MgO, SrO, BaO maps (wt. %) | 138 |
| Figure A3.10 | Sample 2b-4-7: MgO, SrO, BaO maps (wt. %) | 139 |
| Figure A3.11 | Sample 2b-7-9: MgO, SrO, BaO maps (wt. %) | 140 |
| Figure A3.12 | Trace element summary transects from 20 °C/hr cooling runs | 141 |
| Table A3.6 | Comparison of 20 °/hr to 2°/hr Mg, Sr, Ba D rim values | 142 |
| Table A3.7 | Cpx-melt D _U and D _{Th} for 0.1 °C/hr and 1.7 °C/hr cooling | 143 |
| Table A3.8 | Lattice strain parameterizations for 2 °C/hr and 20 °C/hr cooling | 144 |
| Figure A3.13 | D vs. ionic radius curves for 2 °C/hr and 20 °C/hr cooling data | 146 |

Appendix 4

| | | |
|-------------|---|-----|
| Table A4.1 | Glass and anorthite compositions for 224SAM run products | 147 |
| Table A4.2 | D values and lattice strain parameterization of anorthite/melt data of CAI (CMAST) and run 2b-2-2 (CMAS) compositions | 148 |
| Figure A4.1 | SEM cathodoluminescence intensity of 224SAM21 anorthite | 151 |
| Figure A4.2 | 224SAM21 anorthite correlation plots against MgO content | 152 |
| Table A4.3 | Summary table of cathodoluminescence reconnaissance study | 153 |
| Figure A4.3 | SEM CL intensity images of Ti- and Eu-bearing experiments | 155 |
| Figure A4.4 | SEM-CL intensity images of Ti+Eu-, Mn-, and Ge-bearing runs | 156 |
| Figure A4.5 | SEM-CL intensity of anorthites with varying excess silica | 157 |

Appendix 5

| | | |
|-------------|---|-----|
| Figure A5.1 | CMAS1 melt compositions projected onto the CAS ternary | 159 |
| Table A5.1 | Initial CMAS1 melt compositions | 160 |
| Table A5.2 | CMAS1 anorthite compositions | 160 |
| Table A5.3 | CMAS1 final glass compositions | 161 |
| Figure A5.2 | Excess silica component []Si ₄ O ₈ in CMAS1 anorthites | 161 |
| Figure A5.3 | Glass Na ₂ O content change as a function of time in furnace | 162 |
| Figure A5.4 | CMAS1 D^{molar}_{MgO} and melt activity products relationship for Mg ²⁺ partitioning onto IV and VIII anorthite coordination sites | 164 |
| Table A5.4 | Anorthite/melt partitioning in CMAS1 compositions at ~1400 °C | 164 |
| Table A5.5 | Lattice strain model parameterization of CMAS1 divalent element (Mg, Ca, Sr, Ba) partitioning data | 166 |
| Figure A5.5 | CMAS1 alkaline earth element D vs. ionic radius curves | 166 |

Appendix 6

| | | |
|------------|------------------|-----|
| Table A6.1 | Thesis run table | 167 |
|------------|------------------|-----|

Chapter 1: Introduction

1.1 BACKGROUND

Most magmatic differentiation processes occur in regions within the Earth that are inaccessible to direct study. Crystal fractionation, partial melting, magma mixing, assimilation, and transport may occur simultaneously as magmas evolve, yet surficial exposures of their products frequently provide our only clues as to how these processes progress and interact at depth. Trace elements are particularly useful recorders of petrogenetic and geochemical histories due to equilibrium partitioning behavior independent of their concentrations. Unfortunately, knowledge of trace element partition coefficients (D_i^j , defined as [concentration of i in mineral j]/[concentration of i in coexisting melt]) in magmatic and fluid systems remains incomplete, and experimental determination of D values for all geologically relevant elements, compositional systems, pressures, and temperature conditions is not feasible. In the absence of more specific knowledge of partitioning behavior, partition coefficients are often assumed constant throughout simulated igneous processes. Such gross approximations, while reasonable representations of partitioning in some systems, can severely limit understanding of processes in others. Therefore theoretical models of magma evolution should account for the dynamic dependence of D values on both intensive and extensive magmatic system variables.

Partition coefficients can be complex functions of pressure, temperature, and phase composition, and covariances amongst these variables frequently obscure their respective influences on partitioning. This is illustrated in literature compilations of

partitioning between silicate melts and olivine (Bedard, 2005) and plagioclase (Bedard, 2006), where efforts to relate D values to various parameters such as melt MgO and SiO₂ contents yield relatively loose correlations, suggesting more complex controls on partitioning behavior. In particular, efforts to separate the effects of the two most important variables, anorthite content (An) and temperature, in data for $D^{\text{plagioclase}}$ tend to show a considerable amount of scatter (Blundy and Wood, 1991). Many partitioning studies note empirical correlations between partition coefficients and various melt parameters (e.g., Kohn and Schofield, 1994; Mysen and Virgo, 1980; Toplis and Corgne, 2002), but such observations often have limited relevance for predicting absolute D values in other systems. Isolating the contribution of melt composition to partitioning behavior requires a targeted study that varies composition of the liquid phase while holding T , P , and mineral composition constant. Resulting systematic variations in D values then may be attributed to melt composition and rationalized in terms of an appropriate thermodynamic melt model.

1.2 THESIS APPROACH AND SCOPE

This work was motivated by a continuing need to systematically quantify the role of melt thermodynamics on trace element partitioning behavior between mineral and coexisting liquid phases in order to more accurately model magma differentiation. Formulating a general model of equilibrium partitioning applicable to any magmatic system requires rigorous treatment of both the liquid and solid phases. This study builds its explicit thermodynamic treatment of melt major oxide activities and trace element activity coefficients on the lattice strain model of Blundy and Wood (1994), which relates

partition coefficients to temperature and an expression for crystal lattice strain energy proposed by Brice (1975). The lattice strain model relegates any melt compositional effects, along with mineral fusion and trace element energetics aside from lattice strain in the mineral phase, into a single fit parameter, the pre-exponential term D_o of equation (2.1). Our objective here is to specifically quantify the role of melt composition on partitioning behavior and possibly further elucidate the physical meanings of parameters used in the lattice strain model of partitioning.

This thesis is composed of two principal parts: (1) experimental determination of partition coefficients in a simple system to develop a general partitioning model explicitly accounting for melt thermodynamics, and (2) testing model predictive capabilities by comparing calculated anorthite/melt radium partition coefficients with actual measurements of D_{Ra} , for which no experimental data have been hitherto available. The experimental study of alkaline earth element partition coefficients (Mg, Ca, Sr, and Ba) for anorthite and a range of CMAS liquids described in chapter 2 calibrates a proposed general formalism for partitioning, equation (2.11), that augments existing crystal chemical modeling. Chapter 3 provides details of the Berman (1983) CMAS liquid thermodynamic model reoptimization used in chapter 2 and documents its improved performance in the 40–50 wt. % SiO_2 composition space of interest.

In the second part of this work we undertook the first-ever experimental study of radium partitioning between anorthite and a CMAS liquid. Chapter 4 describes a multi-step gas flow line built for containing radon and other radioactive daughter products emitted over the course of ^{226}Ra -bearing dynamic crystallization experiments. Also discussed are results of γ -spectroscopic analyses evaluating the extent of radium

volatilization, which were conducted upon completion of the experimental work. Chapter 5 describes measurement of ^{226}Ra experimental run products by ion microprobe and compares the partitioning results with model predictions. The 1600 year half-life of ^{226}Ra makes it an important chronometer of relatively recent (<8000 years) magmatic processes, and ^{226}Ra excesses relative to its radioactive parent ^{230}Th , where the activity ratio ($^{226}\text{Ra}/^{230}\text{Th}$)>1, have been recorded for young volcanics across a wide range of geologic environments (Turner et al., 2001). The significance of these data for radium transport and storage in plagioclase-bearing systems are discussed, as are implications for model predictions of radium partitioning behavior between clinopyroxene and melt within the mantle melting column. Proposed directions for future work are outlined in chapter 6.

Appendix material is divided into six sections. Appendix 1 provides additional description of the experimental design and analytical approaches adopted for the study of chapter 2. Partitioning data from compositions doped at different concentrations of Ba and measured at different locations within anorthite crystals (centers vs. edges) are compared. Ion microprobe data for Be^{2+} partitioning are presented and contrasted with previous D_{Be} plagioclase/melt measurements (Bindeman et al., 1998). Appendix 2 shows the complete data set, in the form of two-dimensional (2-D) compositional maps of crystal transects and surrounding glass, used to calculate D values reported in chapter 2. Appendix 3 documents the crystal growth dynamics throughout the controlled cooling experiments of chapter 2 with analyses of experiments quenched at intermediate times during the cooling history. Extent of anorthite crystallization and evolution of melt heterogeneities are tracked, and important anorthite trace element (Mg, Sr, and Ba)

contents in glass adjacent to crystals have been mapped to investigate the possibility of concentration gradient development. Since crystals can incorporate elevated, nonequilibrium amounts of trace elements into their structures under rapid cooling conditions (e.g., LaTourrette, 1993; Watson and Liang, 1995), anorthites were grown from three representative compositions of chapter 2 by lowering furnace temperature 20 °C/hr to determine the effect of cooling rate on alkaline earth element partition coefficients in these systems. *D* values from those experiments are slightly higher than those from the 2 °C/hr cooling experiments considered in chapter 2, but the effect of cooling rate is minimal.

Appendix 4 presents anorthite/melt partitioning data from a CAI (meteoritic Ca, Al-rich inclusion)-like CMAS+Ti composition based on that of Simon et al. (1994) and compares results with those of composition 2b-2 in chapter 2. The presence of 2 wt. % titanium in the melt apparently has little impact on divalent element partitioning behavior. Pronounced cathodoluminescence was observed by scanning electron microscope (SEM) in anorthites grown from the CMAS+Ti composition and investigated with a series of doping experiments, but attempts at replicating the phenomenon proved unsuccessful. Appendix 5 consists of data from a preliminary study that measured anorthite/melt divalent element partition coefficients grown from liquids ranging from 40 to 60 wt. % SiO₂. Erratic Na and increasing Si solid solution in anorthite run products rendered these experiments unsuitable for isolating melt effects on partitioning but produced discernable systematic partitioning trends. A complete list of experiments discussed in the text of this thesis is provided in appendix 6.

Chapter 2: Determination of Melt Influence on Divalent Element Partitioning between Anorthite and CMAS melts*

2.1 INTRODUCTION

Trace element distributions between mineral and melt phases have proven to be important tools in understanding differentiation histories of lunar and terrestrial rocks. One important basis for their value is the apparent simplicity in trace element behavior that arises from Henry's Law – at low concentrations, the partition coefficient D_i , defined after Nernst as [concentration of element i in crystal phase]/[concentration of element i in melt phase] (Beattie et al., 1993), is found to be independent of the concentration of the trace element. Most modeling of igneous processes continues to employ a constant partition coefficient to describe distribution of a particular element between melts and each mineral phase of interest. In reality, however, mineral/melt partition coefficients vary with pressure, temperature, and the major-element compositions of the melt and mineral phases. Ideally, therefore, differentiation models should be able to dynamically account for changing partitioning behavior over the course of magma evolution.

The chemical complexity of natural systems prevents experimental determination of equilibrium trace element partitioning in systems containing all possible combinations of components and physical conditions (i.e., temperature, pressure, oxygen fugacity) of interest. Even a set of high-quality experimental data customized to the situation of

* Adapted from Miller, S.A., Asimow, P.D., and Burnett, D.S. (2006) Determination of melt influence on divalent element partitioning between anorthite and CMAS melts. *Geochimica et Cosmochimica Acta*, 70, 4258-4274.

interest requires an interpolation scheme for use in numerical models. In the interest of overcoming such limitations, development of predictive models for trace element partitioning continues to be an area of active research. Blundy and Wood (1994) and Wood and Blundy (2001) describe a quite successful formalism that represents considerable progress towards a general predictive model of trace element partitioning. In particular, it explains the observed parabolic relationship between the cation radius and the logarithm of the partition coefficients of various homovalent trace elements for a given crystal (Higuchi and Nagasawa, 1969; Onuma et al., 1968). The model incorporates the Brice (1975) model of crystal lattice strain energy, taken to be a function of misfit in radius between a substituting cation and a particular crystallographic site, into a general expression for partitioning:

$$D_i(\mathbf{P}, \mathbf{T}, \mathbf{X}) = D_o(\mathbf{P}, \mathbf{T}, \mathbf{X}) \exp \left[-4\pi EN_A \left[\frac{r_o}{2}(r_i - r_o)^2 + \frac{1}{3}(r_i - r_o)^3 \right] / RT \right], \quad (2.1)$$

where r_i is the ionic radius of cation i ; r_o , the ideal (strain-free) radius of the lattice site; D_o , the partition coefficient of an ideally sized cation for that lattice site; and E , a strain parameter for the site. N_A is Avogadro's number, R is the gas constant, and T is absolute temperature. Extensions of this model have investigated prediction of the r_o and E parameters from macroscopic structural and elastic data on the host phase (e.g., Purton et al., 1996; Purton et al., 2000), systematics of variations in the fit parameters with mineral composition along solid solution joins (e.g., Hill et al., 2000; van Westrenen et al., 1999), systematics of heterovalent substitution (Wood and Blundy, 2001) and, in several studies (Blundy et al., 1996; van Westrenen et al., 2001; Wood and Blundy, 1997), incorporation of the effects of melt composition using an approximation to melt thermodynamics based on ideal mixing of quasi-crystalline six-oxygen species.

There are numerous reports of melt influence on partitioning behavior (e.g., Kohn and Schofield, 1994; Linnen and Keppler, 2002; Mysen and Virgo, 1980; Peters et al., 1995; Prowatke and Klemme, 2005). Recent work on the importance of melt composition has focused on the polymerization state of the melt, a melt structure index, as a key variable (e.g., Libourel, 1999; Mysen and Dubinsky, 2004; Toplis and Corgne, 2002). Because the magnitude and complexity of interactions among variables in natural systems often obscure their relationships to one another, insights sometimes must first come from study of simpler systems. The basalt analogue CMAS (CaO-MgO-Al₂O₃-SiO₂) provides a petrologically useful, low-variance system in which to gain fundamental understanding of phase composition influence on partitioning behavior. For our purposes, the key advantages of the CMAS system are the purity of mineral phases that crystallize in this system and the availability of a high-quality activity-composition model for the melt phase at ambient pressure (Berman, 1983). Together, these advantages allow us to isolate the role of melt composition in variation of partition coefficients and to separate these variations into the part that can be understood through the major-element thermodynamics of crystal-liquid equilibrium and the residual part that reflects behavior of trace elements in the melt.

We isolate the effects of melt composition on divalent element (Mg, Ca, Sr, and Ba) partitioning between anorthite and a range of seven CMAS liquid compositions. We chose anorthite because it crystallizes from a wide range of melt compositions in CMAS, and because in Na-free systems we expected essentially no variation in mineral composition. This work considers how abundance of major element network-modifying cations, Ca and Mg, in nearly isopolymerized melts controls partitioning of alkaline earth

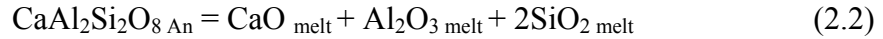
elements, which are cations of moderate charge density and not expected to exhibit much variation in D_i values (Ryerson and Hess, 1978; Watson, 1976). The systematic variation in the parameter D_o that we observe in our experimental systems is thermodynamically rationalized in terms of major element melt chemistry. Remaining deviation in partitioning behavior from the best-fitting lattice strain model, after this major-element melt thermodynamics correction, is taken to represent the influence of melt trace species activities. Although the particular example shown here is restricted to the CMAS system, it is meant to illustrate how, in general, the availability of an activity-composition model for multi-component melts, in combination with lattice strain theory and some corrections for trace activities in the melt, leads to a general theory for prediction of partition coefficients.

2.2 DESIGN CONSIDERATIONS

2.2.1 Choice of Compositions

Given that crystal chemistry likely controls the bulk of isovalent trace element mineral/melt partitioning variation (Blundy and Wood, 1994), the challenge of isolating the influence of melt composition lies in varying melt composition while keeping mineral composition constant from experiment to experiment, at constant temperature and pressure. We sought to achieve this by identifying melt compositions in the simple CMAS system, using an internally consistent thermodynamic model (Berman, 1983), that are expected to coexist with stoichiometric anorthite at our chosen liquidus temperature of 1400 °C. These criteria amount to two nonlinear constraints on the choice of liquid

compositions, which reduces the three degrees of compositional freedom in this quaternary system to one. First, in order to have equal liquidus temperature, all the compositions must satisfy the equilibrium

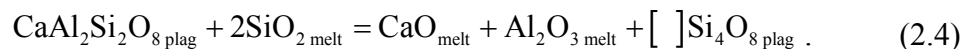


at equal temperature. Applying the law of mass action, the equilibrium constant for this reaction is

$$K_{\text{anorthite}}^{\text{fusion}} = \frac{(a_{\text{CaO}}^{\text{melt}})(a_{\text{Al}_2\text{O}_3}^{\text{melt}})(a_{\text{SiO}_2}^{\text{melt}})^2}{a_{\text{CaAl}_2\text{Si}_2\text{O}_8 \text{ plagioclase}}}. \quad (2.3)$$

Hence all liquids that coexist with nearly pure anorthite ($a_{\text{plag}}^{\text{An}} = 1$) at given conditions have equal values of the activity product $(a_{\text{CaO}})(a_{\text{Al}_2\text{O}_3})(a_{\text{SiO}_2})^2$.

Second, anorthite is known to incorporate significant amounts of excess silica ($[\text{Si}_4\text{O}_8]$) into its structure under low-pressure experimental conditions (Bruno and Facchinelli, 1974; Ito, 1976; Longhi and Hays, 1979) and in some natural environments both terrestrial (Bryan, 1974; Kimata et al., 1995; Murakami et al., 1992) and lunar (e.g., Beatty and Albee, 1980; Bruno and Facchinelli, 1975). Attempts to use starting melt compositions ranging from 45 to 65 wt % SiO_2 and constant 1 wt % MgO content generated crystals with a wide range of mole fractions of the excess silica component. As a result, any melt composition contribution to partitioning behavior in these experiments could not be readily resolved from the effect of significant changes to the crystal structure resulting from solid solution with SiO_2 . Hence, in order to find compositions that would crystallize anorthite of identical stoichiometry, we write the substitution reaction for excess SiO_2 in anorthite:



The equilibrium constant for this reaction is

$$K_{\text{plagioclase}}^{\text{exchange}} = \frac{(a_{\text{melt}}^{\text{CaO}})(a_{\text{melt}}^{\text{Al}_2\text{O}_3})(a_{\text{plag}}^{\text{[Si}_4\text{O}_8]})}{(a_{\text{plag}}^{\text{CaAl}_2\text{Si}_2\text{O}_8})(a_{\text{melt}}^{\text{SiO}_2})^2}, \quad (2.5)$$

which shows that, at equal temperature, all melt compositions with equal value of the activity quotient $(a_{\text{CaO}})(a_{\text{Al}_2\text{O}_3})/(a_{\text{SiO}_2})^2$ should yield anorthite compositions with equal activity of the excess silica component.

From our family of solutions that fit these two constraints (a curvilinear subspace of CaO-MgO-Al₂O₃-SiO₂ space), we selected seven points that would span the range of possible melt compositions yet still lie comfortably within the anorthite phase volume, to ensure that no other phases would crystallize during controlled cooling experiments. Figure 2.1 illustrates the locations of these compositions within the CMAS tetrahedron.

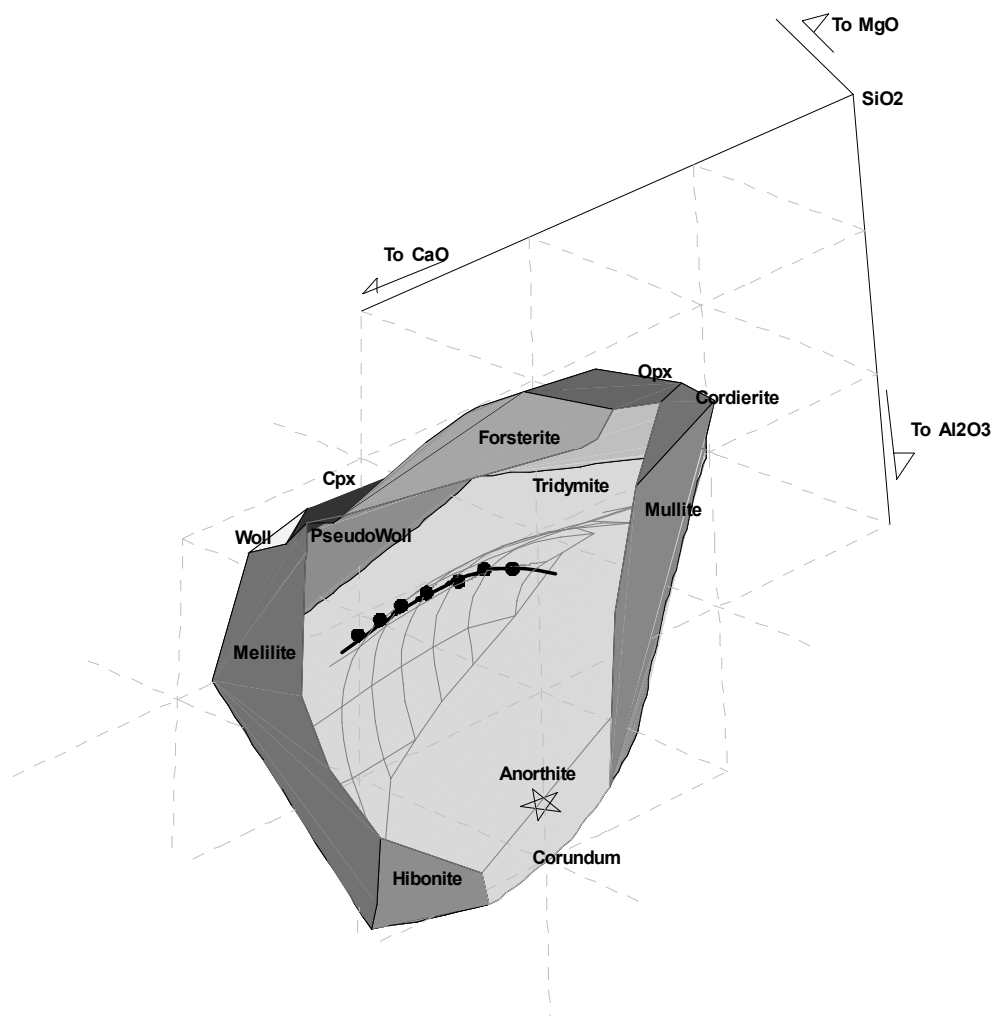


Figure 2.1. The choice of liquid compositions for this study is illustrated in a three-dimensional perspective view of the CMAS tetrahedron. The composition of anorthite is shown by the black star. The anorthite liquidus volume is delimited by the CAS ternary base and a number of bounding surfaces, each labeled by the phase that coexists with anorthite and liquid on that boundary; the spinel boundary has been left transparent to expose the interior of the phase volume. Within that volume, the gray mesh surface indicates the 1400 °C isotherm on the liquidus, calculated using the Berman (1983) model. The black contour on this surface shows the range of liquid compositions that are expected to crystallize stoichiometric anorthite without excess silica (see text). The points along the black contour indicate the seven compositions chosen to span the maximum compositional range consistent with the constraints of crystallizing stoichiometric anorthite at 1400 °C.

2.2.2 Choice of Experimental Protocol

In designing our experimental protocol, we needed to make a basic choice between constant-temperature equilibrium crystallization and controlled-cooling rate fractional crystallization. For the reasons detailed below, we decided that controlled-cooling rate fractional crystallization experiments are more feasible in this system than any attempt to reach static equilibration at constant conditions. Diffusion studies of divalent elements Mg, Ca, Sr, and Ba in plagioclase indicate that diffusion on experimental time scales even at temperatures in excess of 1300 °C is sluggish. Following Cherniak (2002), a spherical approximation of a 100 μm diameter labradorite (An₆₇) grain indicates that it would take six months at 1300 °C for the Ba concentration in the plagioclase core to begin equilibrating with the surrounding melt. Ba diffusion is likely even slower in anorthite than in intermediate plagioclases due to the greater rigidity of calcic plagioclase structures (Blundy and Wood, 1994). Divalent cation diffusion in end-member anorthite is also strongly dependent on ionic radius, with Mg diffusion likely over 200 times faster than that of Ba, according to Mg data of LaTourrette and Wasserburg (1998).

The slow diffusivity of divalent cations within plagioclase makes it ideal for investigating long-term magma chamber evolution using zoning profiles (e.g., Bindeman et al., 1999; Blundy and Shimizu, 1991; Singer et al., 1995), but it presents a significant experimental challenge in equilibrium partitioning studies. On the other hand, assuming that diffusion of these elements in the melt is much faster, the same slow diffusivity

allows nearly perfect fractional crystallization experiments. In light of this, crystal rim trace element compositions were chosen over core data as the most promising representation of equilibrium between anorthite and the coexisting melts of these experiments.

Although a tempting approach would be to calculate partition coefficients based on analysis of core compositions assumed to crystallize first from the starting melt, this introduces a number of unknowns. One disadvantage of relying on core data to capture initial crystallization compositions results from having to assume that, upon nucleating, crystals grow uniformly outward in all directions. In many cases, crystals may nucleate on the surface of the melt bead or on the platinum loop and grow outward from that surface (e.g., Kirkpatrick, 1974; Klein and Uhlmann, 1974; Roskosz et al., 2005; Stolper and Paque, 1986). In these cases, the geometrical centers of the crystals do not crystallize from the initial melt composition. A second disadvantage results from the kinetic barrier of supercooling that prevents crystallization from occurring exactly at the anorthite liquidus temperature of the melt. When crystallization does occur, initial crystallization is likely to be rapid (Lofgren, 1974b) until some degree of kinetic equilibrium is established, after which crystallization progresses at a slower pace, following the controlled cooling pattern established by the thermal program. The initiation of crystallization may also be random, varying from experiment to experiment. Gibb (1974) observed that random nucleation of liquidus phase plagioclase from the Columbia River basalt may occur within a range of over 35 °C below the liquidus. The more recent work of Tsuchiyama (1983) with anorthite and $\text{Di}_{50}\text{An}_{50}$ melt demonstrates that delay in

anorthite nucleation is a function both of initial superheating above its liquidus and duration of time superheated prior to cooling and crystallization.

In order to avoid crystallizing a myriad of tiny (5–10 μm diameter) anorthite crystals that cannot be analyzed with available instrumentation, runs were heated to 10–20 $^{\circ}\text{C}$ above the liquidus to dissociate most of the potential nuclei in the starting melt. Controlled cooling of the sample at 2 $^{\circ}\text{C}/\text{hour}$ has allowed us over 100 hours to grow anorthite crystals with shortest dimensions in excess of 100 μm , providing ample area for analysis. The regular, tabular morphology of these experimental CMAS anorthite laths attests to initiation of slow, controlled crystallization not far from the liquidus. Lofgren (1974a) demonstrated that plagioclase crystals with tabular morphology generally grow when the degree of supercooling is 30 $^{\circ}\text{C}$ or less in basaltic liquid. At higher degrees of supercooling, acicular and skeletal crystals are formed.

2.2.3 Choice of Doping Concentrations

The choice of a fractional crystallization model and rim compositions to represent the solids requires fairly good spatial resolution, even though the experimental crystals are quite large. This, in turn, makes electron probe analysis in some ways superior to ion probe analysis with the typical performance characteristics of most ion probes. However, analysis of Sr and Ba by electron probe requires doping to fairly high concentration and this, in turn, requires evaluation of the limits of Henry's law behavior. Recent work of Bindeman and Davis (2000) has reconfirmed the results of Drake and Weill (1975), showing partition coefficients of Sr between plagioclase and melts of natural

concentration to be identical to those of synthetic samples doped to 11,000 ppm. Bindeman and Davis also demonstrated similar Henrian behavior of Ba doped at 5500 ppm, and Drake and Weill report Ba exhibiting the same Henry's law constant for melt concentrations in excess of 2 wt. %. As our experiments were doped with approximately 1000 ppm Sr and 3000 ppm Ba, we expect no deviation from Henry's Law for the solid in this concentration range for these elements.

2.2.4 Experimental Procedure and Analytical Methods

Alfa Aesar Puratronic™ SiO₂, Al₂O₃, MgO, and CaCO₃ were used to make our starting compositions. Ingredients were dried overnight; the oxides at 800 °C and CaCO₃ at 140 °C. Materials were removed from the drying oven and cooled in vacuum before weighing. Weighed quantities were ground under ethanol in an alumina mortar for five hours. After drying, each mixture was decarbonated by heating to 1000 °C in 200 °C/hour steps and remained at 1000 °C for 24 hours. Powdered mixtures were fused in Pt crucibles at 1450 °C and reground under ethanol for one hour. Half gram separates were spiked with Ba and Sr solutions to achieve concentrations of 3000 ppm and 1000 ppm, respectively, dried, re-fused at 1450 °C, and reground for half an hour. After both grinding steps the fine powder contained a mixture of glass fragments ranging from <1 μm to ~50 μm.

All experiments were conducted at 1 atm in a Deltech vertical muffle furnace. Reconnaissance experiments have shown that anorthite crystals may gain as much as 4 mol % albite component over the course of a 100-hour run in stagnant air. Therefore,

we ran a flow of compressed air through the muffle tube in excess of 200 cm³/hour to minimize the partial pressure of sodium. Temperatures were monitored by a type S Pt-Pt_{0.9}Rh_{0.1} thermocouple. Each experimental charge consisted of ~30 mg of starting material adhered with polyvinyl alcohol to Pt wire loops suspended from a wheel-shaped sample hanger fashioned from 0.5 mm diameter Pt wire.

The thermal history of the experiments was adapted from Simon et al. (1994). Samples of the seven compositions were run in the furnace simultaneously to ensure identical temperature and pressure conditions. After allowing the powder pellets to dry at room temperature for a minimum of six hours, the charges were lowered into the furnace and a multi-step controlled temperature program was begun. First the temperature was raised to approximately 10 °C above the median liquidus of the seven compositions. The furnace was held at that temperature for one hour to reduce the number of potential crystal nuclei in the melts. Next the temperature was decreased 2 °C/hour to 25 °C below the median liquidus and held at constant temperature for 24 hours to allow any rapidly growing crystals to catch up with the thermal conditions and to compensate for delayed nucleation. Cooling then continued at 2 °C/hour to the final hold temperature of 1330 °C. Charges remained at the final run temperature for 30 hours. The samples were quenched by removal out of the top of the furnace and dipping in distilled water.

Samples were mounted in Araldite epoxy and cross sectional surfaces were polished to 0.3 μm fineness with alumina. Element compositions were analyzed using the Caltech JEOL JXA-733 electron microprobe, and raw data were reduced using the CITZAF correction procedure (Armstrong, 1988). Standards used were albite, microcline, fayalite, anorthite, forsterite, a Sr-silicate glass, and benitoite (for Ba). Beam

conditions of 25nA and 15 keV with a 10 μm defocused beam were used for collecting major element data. Counting times were 30 s on-peak and 15 s for each background measurement. Sr, Ba, and Mg in anorthite were also analyzed at 400 nA and 15 keV with a focused beam for 90 s on-peak and 45 s per background. One-sigma (1σ) analytical uncertainty (\sqrt{N}) for a given point is $<2\%$ relative for Sr, Ba, and Mg at operating conditions and counting times specified for both phases. Secondary electron imaging of the 400 nA focused beam spots show the resulting burn marks in the carbon coat to be no more than 12 μm in diameter.

In order to identify any zoning in the crystals, we analyzed rim-to-rim polygonal grids of 100–200 points in 7–9 μm steps oriented in the centers of the long dimension of crystals. Major element compositions were uniform but trace elements showed normal zoning (i.e., concentration increasing towards rim) in some cases. Partitioning analysis and crystal data presented below use only rim analyses most likely to be in equilibrium with the coexisting melt at the final hold temperature of 1330 $^{\circ}\text{C}$. Although the constraint that each liquid composition should coexist with stoichiometrically identical anorthite in all seven charges was applied at an anorthite liquidus temperature of 1400 $^{\circ}\text{C}$, rim-to-rim transects across crystals from each indicate no significant major element variability for crystal edges formed at lower temperature. This permits us to treat crystal chemistry as constant and compare anorthite rim data between charges.

2.2.5 Rates of Crystal Growth and Possible Nonequilibrium Enrichment

In order to place some constraints on the rates of crystal growth, separate runs were conducted in which charges were quenched at intermediate temperatures along the controlled cooling path of these experiments. Extents of crystallization were calculated from the Rayleigh equation and glass major element compositions. The bulk of crystal growth occurs between 45 and 67 hours into our runs, when temperature decreases from 1380 °C to the final temperature of 1330 °C. The most magnesian liquid composition (2b-7) produces the greatest increase in volume crystallized over this interval: from approximately 6 % crystallized to 27 %. For all compositions the fraction crystallized remains constant within analytical error during the final 30 hours of the thermal history in which the charges are held at the final temperature. This indicates that rim growth is unlikely to be affected by supercooling at this stage of the experiments.

How closely our experiments approximate equilibrium partitioning between anorthite and melt depends on how quickly the cations of interest can diffuse away from the crystal interface into the bulk melt, relative to the crystal growth rate. If the anorthite crystallizes faster than diffusion can restore compositional homogeneity throughout the melt, a concentration gradient will develop around the growing crystal. In this rapid growth scenario, incompatible trace elements will become enriched in the melt boundary layer and be incorporated into the expanding crystal structure in greater concentrations than would be characteristic of equilibrium partitioning between the crystal interface and the melt as a whole.

Even if cation diffusion within the melt is rapid enough to prevent buildup of a liquid concentration gradient in incompatible elements, crystal zoning can occur if the growing crystal incorporates incompatible elements from the melt more quickly than those cations can diffuse out of the moving boundary layer (a few unit cells thick) of the anorthite crystals themselves. The sector zoning model of Watson and Liang (1995) demonstrates how this can occur even in instances of slow growth, such as titanite formation within plutons, if temperatures are low (700–800 °C) and cation diffusivities through the crystal lattices are slow. Possible extent of non-equilibrium surface enrichment in the experimentally grown anorthites of this study may be evaluated using the general, qualitative version of the Watson and Liang model. In it they assume that the half width of a crystal growth layer is a 5 Å silicate monolayer, and that the lattice diffusion distance is approximately equal to the growth distance into the melt when $V/Df_i \approx 2 \cdot 10^9 \text{ m}^{-1}$, where V is the growth rate (m/s) and Df_i is the lattice diffusivity of element i (m^2/s). Surface enrichment is likely to be preserved within the crystal structure if $V \geq 2 \cdot 10^9 Df_i$.

To obtain a conservative estimate for the fastest rate of crystal growth in the experiments of this study, one may calculate the total volume a sample melt bead from its quenched diameter of 3 mm. We consider this melt volume as a cube with half-edge length 1.2 mm and represent a change from 6 % to 27 % crystal growth as an expansion of a single theoretical cubic lath of anorthite from the center of the melt cube. Assuming crystal and melt have roughly comparable densities and isotropic growth, the one-dimensional growth outward in any direction parallel to the faces of this melt cube between 6 % and 27 % crystallization is $\sim 310 \text{ }\mu\text{m}$. Assuming crystal growth follows the

linear progression of the controlled cooling of the furnace from ~ 1380 to 1330 °C, the crystal growth rate of this theoretical anorthite cube is $\sim 4 \cdot 10^{-9}$ m/s.

This simple calculation represents an upper limit on growth rate, as anorthite typically forms rectangular laths, and growth at later stages onto an existing crystal will build width in layers parallel to the elongated direction of the crystal, requiring the growth rate along that width to be slower for a given volume increase than if the crystal had a cubic shape. Furthermore, assuming multiple crystals nucleate within a charge instead of one lone crystal in the above thought experiment, comparable increases in overall crystal volume will occur with any given crystal having a proportionally smaller width than it would have in the single crystal scenario. Thus the short length of a crystal analyzed in our experiments, which average between 5 and 20 exposed crystal cross sections per charge, is likely the result of a lower growth rate than that calculated for a hypothetical solitary crystal.

The competition between crystal growth rate and lattice diffusion in determining whether or not surface enrichment develops also depends on knowledge of cation diffusion in anorthite at temperatures of interest. According to the first-order, qualitative version of the Watson and Liang model and the estimate of anorthite growth rate given above, surface enrichment might be expected if lattice diffusion for cations of interest is slower than $2 \cdot 10^{-18}$ m²/s, according to our upper bound crystal growth rate. Calculating the diffusivity of Sr in anorthite at 1330 °C using the Arrhenius parameters of Giletti and Casserly (1994) yields a value of $1.14 \cdot 10^{-17}$ m²/s, which is about an order of magnitude faster than our surface enrichment threshold.

No data exist for Ba diffusion in pure anorthite, and diffusion rates may be higher in more albitic compositions. The most anorthitic plagioclase composition (An_{67}) of the Cherniak (2002) study, along its slowest direction, perpendicular to (001), has a Ba diffusivity at 1300 °C of $7 \cdot 10^{-18}$ m²/s. The proximity of this value to our surface enrichment threshold may mean that there is a higher probability that the observed Ba content of anorthite rims in this study are elevated above equilibrium values, but our approximation of crystal growth and knowledge of diffusion behavior in these experiments are too uncertain to constrain this further.

2.3 RESULTS AND DISCUSSION

2.3.1 Anorthite-Melt Partitioning Data

Melt and anorthite compositions are listed in Tables 2.1 and 2.2, respectively. Liquidus temperatures (Table 2.3) of the starting materials were determined from isothermal experiments in which samples were lowered into the furnace at desired run temperature and removed after three hours. Presence or absence of crystallization was ascertained by visual inspection. Mass balance calculations of charge compositions indicate that anorthite is the sole crystal phase present in all experiments and extent of crystallization ranges from 15 % to 30 %. Because the percent crystallization of anorthite was relatively low in these experiments, the melt composition upon quenching did not deviate far enough from the starting liquid to produce identifiable changes in anorthite major element chemistry.

Table 2.1. Compositions of melt quenched to glass (wt. %) coexisting with anorthite at 1330 °C determined by EMP. Uncertainties (1σ) for the last digit(s) indicated in parentheses.

| | 2b-1-2 n = 10 Mg,Sr,Ba n = 17 | 2b-2-2 n = 10 Mg,Sr,Ba n = 27 | 2b-3-2 n = 10 Mg,Sr,Ba n = 7 | 2b-4-2 n = 10 Mg,Sr,Ba n = 9 | 2b-5-2 n = 10 Mg,Sr,Ba n = 16 | 2b-6-2 n = 10 Mg,Sr,Ba n = 21 | 2b-7-2 n = 10 Mg,Sr,Ba n = 23 |
|--------------------------------|--|--|---------------------------------------|---------------------------------------|--|--|--|
| SiO ₂ | 47.97 (11) | 47.41 (30) | 47.86 (9) | 47.60 (28) | 46.34 (29) | 46.29 (29) | 46.39 (13) |
| Al ₂ O ₃ | 18.14 (19) | 17.80 (14) | 17.92 (16) | 18.03 (8) | 18.80 (7) | 19.83 (12) | 20.97 (6) |
| MgO | 1.19 (6) | 3.22 (1) | 5.52 (5) | 7.76 (1) | 10.28 (3) | 12.52 (6) | 14.66 (30) |
| CaO | 32.48 (18) | 30.68 (14) | 28.05 (10) | 25.86 (11) | 23.20 (8) | 20.25 (5) | 17.57 (10) |
| SrO | 0.136 (5) | 0.144 (4) | 0.142 (6) | 0.133 (6) | 0.141 (5) | 0.147 (4) | 0.127 (4) |
| BaO | 0.60 (3) | 0.64 (1) | 0.65 (1) | 0.66 (1) | 0.73 (1) | 0.71 (1) | 0.72 (2) |
| FeO* | 0.06 (1) | 0.07 (1) | 0.08 (2) | 0.07 (1) | 0.07 (3) | 0.10 (1) | 0.07 (2) |
| K ₂ O | 0.021 (6) | 0.019 (7) | na | 0.026 (7) | 0.023 (5) | na | na |
| Na ₂ O | <u>0.01 (1)</u> | <u>0.02 (1)</u> | <u>0.02 (1)</u> | <u>0.02 (1)</u> | <u>0.02 (1)</u> | <u>0.02 (1)</u> | <u>0.02 (1)</u> |
| | 100.62(18) | 100.02(30) | 100.25(18) | 100.15(19) | 99.61(25) | 99.87(16) | 100.52(34) |

* All Fe reported as FeO
na = not analyzed

Table 2.2. Anorthite compositions (wt. %) coexisting with melt at 1330 °C determined by EMP. Uncertainties (1σ) for the last digit(s) indicated in parentheses.

| | 2b-1-2 n = 10 Mg,Sr,Ba n = 19 | 2b-2-2 n = 10 Mg,Sr,Ba n = 11 | 2b-3-2 n = 10 Mg,Sr,Ba n = 10 | 2b-4-2 n = 10 Mg,Sr,Ba n = 6 | 2b-5-2 n = 10 Mg,Sr,Ba n = 8 | 2b-6-2 n = 10 Mg,Sr,Ba n = 9 | 2b-7-2 n = 10 Mg,Sr,Ba n = 12 |
|--------------------------------|--|--|--|---------------------------------------|---------------------------------------|---------------------------------------|--|
| SiO ₂ | 43.41 (10) | 43.04 (23) | 43.39 (12) | 43.45 (26) | 42.98 (18) | 43.09 (44) | 43.46 (20) |
| Al ₂ O ₃ | 36.48 (15) | 35.92 (10) | 36.21 (11) | 35.99 (6) | 35.52 (8) | 35.92 (29) | 36.20 (10) |
| MgO | 0.099 (4) | 0.226 (4) | 0.298 (7) | 0.359 (28) | 0.376 (6) | 0.371 (11) | 0.376 (12) |
| CaO | 20.38 (11) | 20.41 (10) | 20.28 (6) | 20.39 (9) | 20.30 (5) | 20.12 (7) | 20.05 (10) |
| SrO | 0.111 (5) | 0.120 (5) | 0.123 (5) | 0.109 (14) | 0.144 (5) | 0.166 (4) | 0.160 (5) |
| BaO | 0.097 (8) | 0.086 (12) | 0.092 (6) | 0.126 (4) | 0.117 (7) | 0.115 (6) | 0.133 (14) |
| FeO* | 0.02 (2) | 0.01 (1) | 0.03 (1) | 0.02 (1) | 0.02 (2) | 0.02 (1) | 0.02 (1) |
| K ₂ O | 0.020 (7) | 0.016 (6) | na | 0.018 (6) | 0.017 (5) | na | na |
| Na ₂ O | <u>0.01 (1)</u> | <u>0.02 (1)</u> | <u>0.01 (1)</u> | <u>0.02 (1)</u> | <u>0.02 (1)</u> | <u>0.02 (1)</u> | <u>0.02 (1)</u> |
| | 100.63 (41) | 99.85 (48) | 100.43 (33) | 100.48(45) | 99.49 (36) | 99.82 (84) | 100.42 (45) |

* All Fe reported as FeO
na = not analyzed

Anorthite crystals exhibit tabular, lath-like morphology. A few appear to contain melt inclusions and such crystals were avoided during analysis. Figure 2.2 shows a

representative sample cross-section from these experiments. No identifiable quench textures were formed in the charges. Linear transects extending perpendicularly in 2 μm steps from crystal rims to $\sim 70 \mu\text{m}$ into surrounding melt revealed only slight concentration gradients for Mg in the most magnesian composition, and none for Ba and Sr even in samples quenched at 67 hours, immediately after the 2 $^{\circ}\text{C}/\text{hr}$ cooling step at the final hold temperature of 1330 $^{\circ}\text{C}$. This indicates that near-equilibrium conditions were likely reached, although the most conservative interpretation is that all calculated partition coefficient data from this study should be considered upper limits (assuming kinetic effects will enrich growing crystals in incompatible trace elements and produce elevated D values).

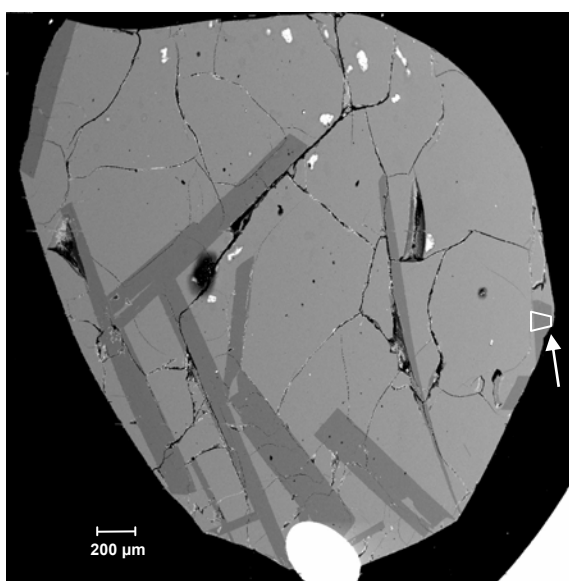


Figure 2.2. Back-scattered electron image of sample 2b-3-2. Crystals showing rapid growth and/or melt inclusions were avoided in analysis. Analyzed polygonal grid area outlined in white and indicated by arrow.

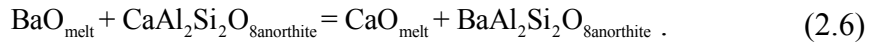
Divalent element partition coefficients between anorthite and coexisting melt at time of sample quenching (Table 2.3) show a systematic decrease in the observed bulk Mg partition coefficient as melts become more magnesian, and similarly, Ca partition coefficients have lower values with increasing lime content in coexisting liquids. D_{Sr} increases with increasing D_{Ca} . D_{Ba} , though analytically less resolved, indicates a corresponding trend of higher partition coefficient with lower calcium abundance in melt.

Table 2.3. Normalized CMAS melt compositions (wt. %) and molar partition coefficients with 1σ uncertainties for the last digit(s) indicated in parentheses. Molar partition coefficients calculated from EMP weight % data as neutral oxides: (moles XO/g)/ Σ (moles XO/g) in anorthite divided by the same quantity in the glass. Uncertainty of anorthite liquidus temperatures is $\sim\pm 5$ °C. NBO/T and optical basicity (O.B.) are calculated according to Mills (1993) from full melt composition data. D^{molar}_{MgVIII} calculated from equation (2.17) using the reoptimized parameters listed in chapter 3.

| | 2b-1 | 2b-2 | 2b-3 | 2b-4 | 2b-5 | 2b-6 | 2b-7 |
|--------------------------------|-------------|-------------|-------------|-------------|-------------|-------------|-------------|
| T_{Liq} (°C) | 1398 | 1402 | 1400 | 1408 | 1408 | 1408 | 1403 |
| CaO | 32.55 (18) | 30.96 (14) | 28.23 (10) | 26.06 (11) | 23.52 (8) | 20.48 (5) | 17.64 (10) |
| MgO | 1.19 (6) | 3.25 (1) | 5.56 (5) | 7.82 (1) | 10.42 (3) | 12.66 (6) | 14.72 (30) |
| Al ₂ O ₃ | 18.18 (19) | 17.96 (14) | 18.04 (16) | 18.17 (8) | 19.06 (7) | 20.05 (12) | 21.06 (6) |
| SiO ₂ | 48.08 (11) | 47.84 (30) | 48.17 (9) | 47.96 (28) | 46.99 (29) | 46.81 (29) | 46.58 (13) |
| NBO/T | 0.749 (6) | 0.799 (7) | 0.803 (6) | 0.834 (7) | 0.853 (6) | 0.826 (8) | 0.799 (10) |
| O.B. | 0.618 (3) | 0.617 (4) | 0.613 (4) | 0.612 (4) | 0.611 (4) | 0.607 (4) | 0.603 (4) |
| D^{molar}_{Mg} | 0.091 (5) | 0.077 (1) | 0.061 (1) | 0.052 (4) | 0.042 (1) | 0.034 (1) | 0.029 (1) |
| D^{molar}_{MgVIII} | 0.0024 | 0.0023 | 0.0026 | 0.0029 | 0.0035 | 0.0049 | 0.0067 |
| D^{molar}_{Ca} | 0.689 (5) | 0.738 (4) | 0.805 (3) | 0.886 (5) | 0.993 (4) | 1.134 (4) | 1.309 (9) |
| D^{molar}_{Sr} | 0.90 (5) | 0.92 (4) | 0.97 (5) | 1.06 (5) | 1.16 (5) | 1.29 (4) | 1.45 (6) |
| D^{molar}_{Ba} | 0.18 (2) | 0.15 (2) | 0.16 (1) | 0.18 (2) | 0.18 (1) | 0.19 (1) | 0.21 (2) |

2.3.2 Thermodynamic Modeling

The data can be thermodynamically rationalized by using oxide exchange and mineral fusion reactions, an approach common in the literature (e.g., Beckett and Stolper, 2000; Drake, 1976; Drake and Weill, 1975; Longhi et al., 1976), to predict cation partitioning behavior. To demonstrate, we consider an exchange reaction for Ba²⁺ partitioning into anorthite using neutral species and oxide-mineral exchange:



The energy associated with this thermodynamic mixing contribution can be understood in terms of the reaction equilibrium constant,

$$K_{\text{anorthite}}^{\text{exchange}} = e^{(\Delta G_{\text{exchange}}^{\circ} / RT)} = \frac{a_{\text{melt}}^{\text{CaO}} a_{\text{anorthite}}^{\text{BaAl}_2\text{Si}_2\text{O}_8}}{a_{\text{melt}}^{\text{BaO}} a_{\text{anorthite}}^{\text{CaAl}_2\text{Si}_2\text{O}_8}} . \quad (2.7)$$

The equations for the reaction of fusion of the end-member host anorthite and corresponding equilibrium constant are:



$$K_{\text{anorthite}}^{\text{fusion}} = e^{(\Delta G_{\text{fusion}}^{\circ} / RT)} = \frac{a_{\text{anorthite}}^{\text{CaAl}_2\text{Si}_2\text{O}_8}}{a_{\text{melt}}^{\text{CaO}} a_{\text{melt}}^{\text{Al}_2\text{O}_3} (a_{\text{melt}}^{\text{SiO}_2})^2} . \quad (2.9)$$

Multiplication of the fusion and exchange equilibrium constants for anorthite yields

$$\frac{a_{\text{anorthite}}^{\text{BaAl}_2\text{Si}_2\text{O}_8}}{a_{\text{melt}}^{\text{BaO}}} = a_{\text{melt}}^{\text{Al}_2\text{O}_3} (a_{\text{melt}}^{\text{SiO}_2})^2 e^{[(\Delta G_{\text{fusion}}^{\circ} + \Delta G_{\text{exchange}}^{\circ}) / RT]} . \quad (2.10)$$

Explicit incorporation of BaO activity coefficients in both the melt and solid phases produces an expression for the molar partition coefficient of the trace element:

$$D_{\text{BaO}}^{\text{anorthite/melt}} = \frac{X_{\text{anorthite}}^{\text{BaAl}_2\text{Si}_2\text{O}_8}}{X_{\text{melt}}^{\text{BaO}}} = \frac{\gamma_{\text{melt}}^{\text{BaO}}}{\gamma_{\text{anorthite}}^{\text{BaAl}_2\text{Si}_2\text{O}_8}} a_{\text{melt}}^{\text{Al}_2\text{O}_3} (a_{\text{melt}}^{\text{SiO}_2})^2 e^{[(\Delta G_{\text{fusion}}^{\circ} + \Delta G_{\text{exchange}}^{\circ})/RT]} \quad (2.11)$$

Such treatment differs from the analysis of other studies (Blundy et al., 1995; van Westrenen et al., 2001; Wood and Blundy, 1997) by applying a calibrated, oxide-based non-ideal melt mixing model that explicitly describes the D_o term of equation (2.1) as an activity product, rather than relying on an ideal quasi-crystalline melt model where careful selection of speciation and exchange reactions is meant to approximate liquid influence on partitioning. Given that little thermodynamic data for possible melt species exist, particularly for those involving trace elements, the approach preferred here offers a potentially more rigorous accounting of melt thermodynamics when precise experimental data and access to a sufficiently well-calibrated melt model permit.

2.3.3 Equilibrium and CMAS melt model tests

Before proceeding to use these data to extend the lattice strain model of trace element partitioning from an oxide melt perspective, we can perform some tests of whether our data are consistent with near-equilibrium conditions and whether the fusion and exchange relationships described in the previous section are consistent with observed partitioning behavior. We calculate the activities and activity coefficients in the melt based on Berman's (1983) 1 atm stoichiometric model of CMAS liquids. This model uses simple neutral oxides as species and parameterizes melt activities for each oxide as a function of composition and temperature with enthalpy and entropy excess mixing terms (Margules parameters) fitted to mineral-melt equilibria, liquidus, and calorimetric data.

Because the reported uncertainty in the anorthite liquidus temperature for the 20 wt. % Al_2O_3 plane of the quaternary (near our region of interest) exceeds 20 °C, a reoptimization of the Berman model was performed for a portion of the anorthite liquidus space. This was accomplished by adjusting the Margules parameters to minimize the differences between the liquidus temperatures predicted by the model and those experimentally determined for anorthite in 57 CMAS liquids with SiO_2 content between 40 and 50 wt. % (this study, Osborn, 1942; Osborn and Tait, 1952; Tsuchiyama, 1983; Yang et al., 1972). Reoptimization decreased the sum of the discrepancies squared between the observed and predicted liquidus temperatures by 35 %. Results of the anorthite field parameterization used are reported in chapter 3; we caution that this reoptimization considered only anorthite-melt constraints and is presumed to be worse than the original Berman model at describing equilibria with other solids.

For a given trace element obeying Henry's law in anorthite at equilibrium conditions in our experiments, we would expect that its activity coefficient in anorthite would be constant for all melt compositions; of course the standard state quantities $\Delta G^\circ_{\text{fusion}}$ and $\Delta G^\circ_{\text{exchange}}$ are also constants at given temperature (see equation (2.11)). We cannot perform this test using Sr or Ba data because the Berman model does not provide activities of these components in the melt. For Ca, this relationship tests only whether the re-optimized Berman model accurately predicts liquidus temperatures. Hence Mg, the only component of the Berman CMAS melt model that enters the anorthite structure as a trace constituent, provides the best test, but it is complicated by the possibility of substitution into two different sites. Although technically the M-site of anorthite (where Ca resides) has VII-fold coordination, here it will be referred to as VIII-coordinated since

the ionic radius data of Shannon (1976) used later in this paper does not include VII-coordinated Mg radii. This convention also allows us to more easily compare our results to previous work (Blundy and Wood, 1994), which used VIII-fold coordinated ionic radii for divalent elements substituting into plagioclase. The decision to use VIII-fold rather than VII-fold coordinated ionic radii introduces an average 0.06 Å shift in r_o but has no effect on the overall conclusions drawn from this study.

If all Mg were to substitute onto the VIII-fold site of the anorthite structure, our model would predict that the relationship between $D_{\text{MgO}}^{\text{molar}}/a_{\text{Al}_2\text{O}_3}(a_{\text{SiO}_2})^2$ and γ_{MgO} of corresponding melts would be linear and pass through the origin:

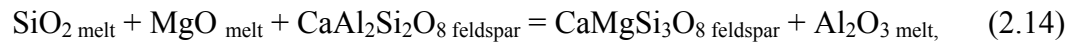
$$\frac{D_{\text{MgO}}^{\text{molar}}}{a_{\text{melt}}^{\text{Al}_2\text{O}_3} (a_{\text{melt}}^{\text{SiO}_2})^2} = \gamma_{\text{melt}}^{\text{MgO}} \left(\frac{e^{(\Delta G_{\text{fusions}}^{\circ} + \Delta G_{\text{exchange}}^{\circ})/RT}}{\gamma_{\text{plagioclase}}^{\text{MgO}}} \right). \quad (2.12)$$

Such a relationship is not found for our re-optimized model and the partitioning data.

Considerable evidence, however, suggests that the majority of Mg in plagioclase resides in a tetrahedrally coordinated (IV) site (e.g., Longhi et al., 1976; Peters et al., 1995), perhaps via an Al substitution. The observed $D_{\text{MgO}}^{\text{molar}}$ is therefore a sum of partitioning onto both M (i.e., VIII-coordinated) and T (IV-coordinated) sites:

$$D_{\text{MgO}}^{\text{molar,observed}} = D_{\text{MgO}}^{\text{molar,VIII}} + D_{\text{MgO}}^{\text{molar,IV}}. \quad (2.13)$$

To account for substitution onto the tetrahedral site, we write the appropriate exchange reaction and equilibrium constant expression:



$$K_{\text{feldspar}}^{\text{exchange}} = e^{(\Delta G_{\text{exchange}}^{\circ}/RT)} = \frac{a_{\text{melt}}^{\text{Al}_2\text{O}_3} a_{\text{feldspar}}^{\text{CaMgSi}_3\text{O}_8}}{a_{\text{melt}}^{\text{MgO}} a_{\text{melt}}^{\text{SiO}_2} a_{\text{anorthite}}^{\text{CaAl}_2\text{Si}_2\text{O}_8}}. \quad (2.15)$$

Multiplication by the anorthite fusion equilibrium constant expression, equation (2.9) generates an equation for partitioning of Mg onto the tetrahedral site:

$$D_{MgO}^{IV} = \frac{\gamma_{melt}^{MgO}}{\gamma_{feldspar}^{CaMgSi_3O_8}} a_{melt}^{CaO} (a_{melt}^{SiO_2})^3 e^{[(\Delta G_{fusion}^{\circ} + \Delta G_{exchange,IV}^{\circ})/RT]} \quad (2.16)$$

This treatment predicts that the observed D_{MgO} for our experiments divided by the melt product $\gamma_{MgO} a_{Al_2O_3} (a_{SiO_2})^2$ for each composition will plot as a linear function of the melt activity quotient $a_{CaO} a_{SiO_2} / a_{Al_2O_3}$ with y-intercept related to the constants for VIII-site partitioning and slope related to the constants for IV-site partitioning:

$$\frac{D_{MgO}}{\gamma_{melt}^{MgO} a_{melt}^{Al_2O_3} (a_{melt}^{SiO_2})^2} = \left[\frac{e^{[(\Delta G_{fusion}^{\circ} + \Delta G_{exchange,VIII}^{\circ})/RT]}}{\gamma_{anorthite}^{CaAl_2Si_2O_8}} \right] + \left[\frac{e^{[(\Delta G_{fusion}^{\circ} + \Delta G_{exchange,IV}^{\circ})/RT]}}{\gamma_{feldspar}^{CaMgSi_3O_8}} \right] \frac{a_{melt}^{CaO} a_{melt}^{SiO_2}}{a_{melt}^{Al_2O_3}} \quad (2.17)$$

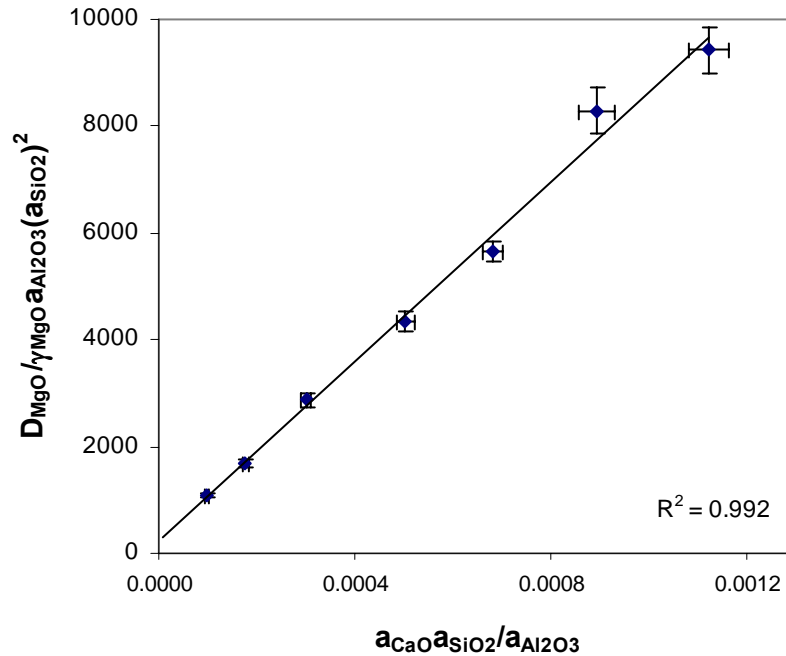


Figure 2.3. Linear relationship of observed D_{MgO}^{molar} and melt activity products expected for Mg^{2+} partitioning onto IV and VIII coordination sites of anorthite crystal lattice. Error bars (1σ) for activity products are propagations of activity uncertainties due to

uncertainty in composition values. No estimate is made of systematic errors inherent in the activity model.

Our data as plotted in Figure 2.3 are consistent with these predictions. This suggests that the Mg data are consistent with equilibrium partitioning according to our reoptimized Berman model and, furthermore, allows us to define the distribution of Mg between IV- and VIII-coordinated sites in anorthite. Calculations using reoptimized Berman liquid model oxide activities show how Mg site occupancy at constant anorthite composition varies as a function of melt composition. Sensitivity of such calculations to activity modeling is demonstrated in Figure 2.4, where both the Berman model and its reoptimization in this study are used to calculate Mg site distribution according to equation (2.17).

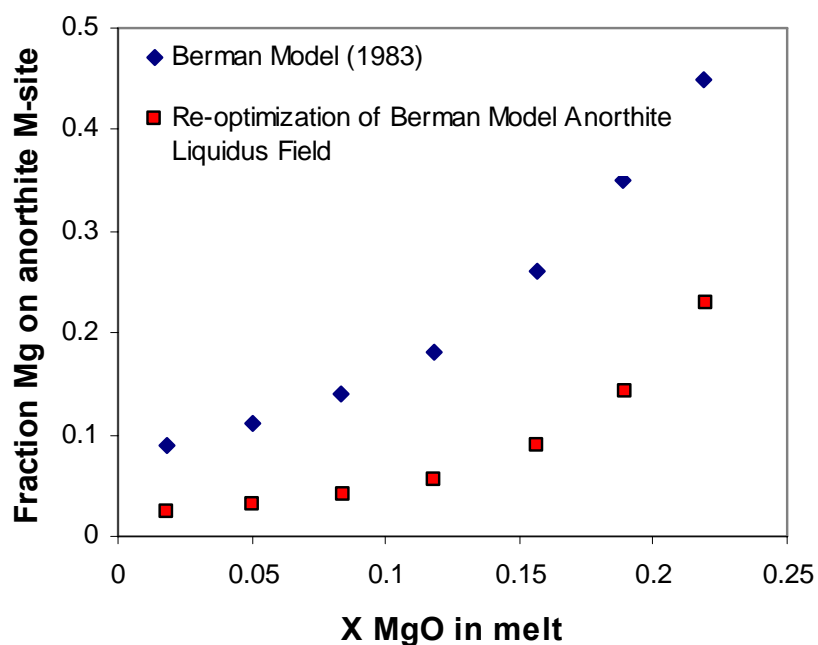


Figure 2.4. Prediction of Mg fractionation between IV (T) and VIII (M) sites in anorthite according to two CMAS liquid activity models: diamonds represent calculation using the Berman (1983) Margules parameters and squares represent calculations using a reoptimization of the Berman model with Margules parameters given in chapter 3.

The two models indicate similar trends in Mg cation site occupation as a function of melt composition but our reoptimization predicts significantly less exchange onto the VIII-coordinated site. Regardless of whether the Berman model or the reoptimization is used, this identification of the VIII-fold coordinated Mg population in anorthite is critical for interpreting the Onuma curves as resulting from constant crystal chemical parameters. It would be desirable to obtain high-sensitivity site occupancy data for Mg in anorthite, perhaps by X-ray absorption spectroscopy, to test these model predictions, but such data are not available at this time.

2.3.4 Extension of Lattice Strain Model

The lattice strain model of Blundy and Wood (1994) builds on the strain theory of Brice (1975) to explain the observed near-parabolic dependence (Higuchi and Nagasawa, 1969; Onuma et al., 1968) of logarithmic element partition coefficients on ionic radius. This model ascribes the bulk of isovalent cation partitioning variation to the importance of crystal-site exchange energy, where the strain energy required to fit same-charge cations into a crystal site is a function of the size misfit between the ideal radius of the crystal site and that of the substituting cation and the strain parameter E , the Young's Modulus of the crystal site of interest:

$$\Delta G_{\text{exchange}} = 4\pi E N_A \left[\frac{r_o}{2} (r_i - r_o)^2 + \frac{1}{3} (r_i - r_o)^3 \right]. \quad (2.18)$$

The lattice strain model, equation (2.1), collects all potential terms relating to melt component activities, mineral fusion, and activity coefficients of the cation species in

solid and liquid phases into a pre-exponential term, D_o , for a given temperature, pressure, cation charge, and mineral composition.

Graphically, on what have come to be known as Onuma diagrams (logarithm of partition coefficient vs. ionic radius), D_o represents the maximum partition coefficient possible for a site, by a hypothetical cation for which $r_i = r_o$. Fitting Onuma curves through our data (Ca, Ba, Sr, and calculated Mg in VIII-fold coordination using the re-optimized Berman activity model for anorthite field) with the parameters of the lattice strain model show that while no systematic variations in r_o or E exist, as may be expected from the success of the lattice strain model, D_o varies significantly with melt composition. This variation near the top of the parabola is expressed not only in the partition coefficients of the major cation Ca (which are required in this case since stoichiometric anorthite of fixed Ca content is coexisting with a range of liquids of varying Ca content), but also by those of Sr, a trace constituent of similar size.

Figure 2.5(a) shows how well a lattice strain model succeeds in predicting the partitioning behavior of these divalent elements between anorthite and the coexisting melts of this study if D_o is calculated from calcium partitioning data. The crystal chemical parameters for ideal site radius (r_o) and site elasticity (E) are taken from Table 1 of Blundy and Wood (1994) and represent linear extrapolations of the parameters for plagioclases to end-member anorthite. The observed partitioning behavior unexplained by the Blundy and Wood model is represented by an average $\chi^2 = 33$ for each measured D value. We propose that the remaining unmodeled behavior and systematic variation in D_o of our experiments can be quantitatively understood in terms of melt thermodynamics via

a more complex model than that of the ideal quasi-crystalline approach employed in other partitioning studies (e.g., van Westrenen et al., 2001; Wood and Blundy, 1997).

D_o varies not with the stability of anorthite in pure anorthite liquid, as the fusion term was approximated in the original Blundy and Wood (1994) paper, but with the stability of anorthite in an actual liquid of interest, and this is accounted for by its dependence on Al_2O_3 and SiO_2 activity. If one uses a neutral oxide stoichiometric melt model:

$$D_{\text{Ca}}^{\text{anorthite/melt}} = \frac{1}{X_{\text{CaO}}^{\text{melt}}} = \gamma_{\text{melt}}^{\text{CaO}} a_{\text{melt}}^{\text{Al}_2\text{O}_3} (a_{\text{melt}}^{\text{SiO}_2})^2 e^{[(\Delta G_{\text{fusion}}^{\circ} + \Delta G_{\text{exchange}}^{\circ})/RT]} \quad (2.19)$$

This thermodynamic correction to the lattice strain model can be quantified using a self-consistent activity-composition model for non-ideal mixing in the melt phase of interest. We use our reoptimized version of the Berman model for CMAS here; the MELTS model (Ghiorso and Sack, 1995), the MTDATA thermodynamic model (Davies et al., 1990) as used in Blundy et al. (1996), or any other accurate parameterization of silicate liquid activity-composition relations could be used in more complex chemical systems. Equation (2.11) states that D_o actually represents $\gamma_{\text{melt}}^{\text{M}2+} a_{\text{melt}}^{\text{Al}_2\text{O}_3} (a_{\text{melt}}^{\text{SiO}_2})^2 e^{\Delta G_{\text{ofus}}/RT}$, assuming that γ_{MO} in the solid phase is 1.

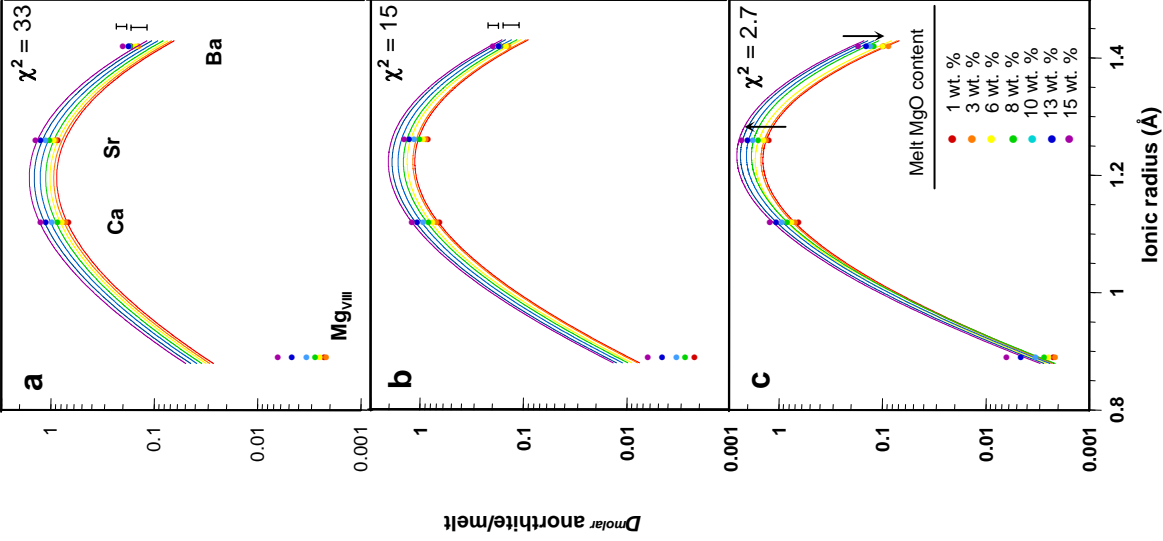


Figure 2.5. Comparison of model parameterizations to molar partition coefficients between anorthite VIII-fold coordinated site and seven melt compositions. 1σ uncertainties for $D^{\text{molar}}_{\text{Ca}}$ and $D^{\text{molar}}_{\text{Sr}}$ are within symbol size and representative error bars are shown for the highest and lowest $D^{\text{molar}}_{\text{Ba}}$. (a) Onuma curves (log plot of D vs. ionic radius from Blundy and Wood (1994) plagioclase crystal chemistry parameters extrapolated to end-member anorthite, with D_o calculated from D_{Ca}). (b) Three-parameter melt major element thermodynamic augmentation of crystal chemistry model where $D_o \propto \gamma_{\text{CaO}}^{\text{Ba}} \gamma_{\text{Al}_2\text{O}_3}^{\text{Ba}} (a_{\text{SiO}_2})^2$. (c) Parameterization including linear corrections for melt γ_{SiO} and γ_{BaO} as a function of MgO content of liquids. Fit improvement is demonstrated by shifting partitioning data towards curves according to modeled γ_{MO} correction.

In Figure 2.5(b) we augment the crystal chemical model of partitioning by substituting for D_o the melt activity product $\gamma_{\text{CaO}}a_{\text{Al}_2\text{O}_3}(a_{\text{SiO}_2})^2$ for each composition and an unknown common parameter representing $e^{\Delta G_{\text{ofus}}/RT}$. Including the crystal chemical parameters E and r_o , this yields a three-parameter solution with an average $\chi^2 = 15$ over the data set of 28 partition coefficients, an improvement on the crystal chemical model.

It should be noted that evidence of deviation from a purely crystal chemical model has been found in comparisons of D values between mineral/silicate and mineral/carbonate liquids (Blundy and Dalton, 2000). The qualitative explanation proposed relates observed variations in E and r_o crystal chemical site fit parameters to energy associated with a structural relaxation in the melt, which adds to the overall solution energy accompanying cation exchange between phases. Van Westrenen et al. (2000) noticed absolute differences in E and r_o that they attributed to the influence of melt composition, but relative variations of these parameters between garnets were dominated by crystal chemistry. If $D_{\text{Mg}}^{\text{molar}}$ (Table 2.3) were used instead of calculated $D_{\text{MgVIII}}^{\text{molar}}$ values in our parameterization, the lattice strain parameter E would have to vary substantially (from 97 to 139 GPa) with melt composition to fit the data. Such variation for these melt compositions seems unlikely and requires ignoring evidence of significant Mg tetrahedral site occupancy mentioned in Section 2.3.3. Instead, our treatment of anorthite/silicate partitioning data in this study allows E and r_o to remain constant as crystal chemical parameters with unchanging mineral composition. Deviations from crystal chemistry partitioning theory are interpreted quantitatively via melt component activities within the D_o term.

The remaining difference between our proposed melt major element contribution to the crystal chemical partitioning model and the data is attributed to the influence of the trace cation activities in the melt. The three-parameter partitioning model accounting for melt major element activity shown in Figure 2.5(b) uses melt γ_{CaO} values in place of individual trace element activity coefficients. However, trace element activity coefficients in the melts, while perhaps similar, are unlikely to be identical to γ_{CaO} and a successful partitioning model should account for this. When empirical linear corrections specific to the systematic behavior of $D^{\text{molar}}_{\text{SrO}}$ and $D^{\text{molar}}_{\text{BaO}}$ over the differing melt compositions are applied, the γ_{MO} -corrected model produces (with fewer parameters!) an average χ^2 smaller than even that obtained from a free parameterization of D_o , r_o , and E values for each experiment independently (Table 2.4).

Table 2.4 summarizes the performance of several partitioning models:

- (1) The Blundy and Wood (1994) crystal lattice strain model contains two parameters, E and r_o , extrapolated to the anorthite endmember from intermediate plagioclase parameterizations. D_o is calculated from D_{Ca} and the resulting average χ^2 equals 33 per datum, where $\chi^2 = [(\ln D^{\text{data}} - \ln D^{\text{model}}) / \ln \sigma^{\text{data}}]^2$. The uncertainty associated with calculated $D^{\text{molar}}_{\text{MgVIII}}$ values remains unknown; for modeling purposes it is assumed to be 0.001.
- (2) A free parameterization with D_o , E , and r_o values for each of the seven compositions in this study decreases the χ^2 average considerably to 11, but requires 21 separate parameters to describe our data as there are no systematic variations in r_o or E .

Table 2.4. Comparison of measured data with model parameterization predictions of anorthite/melt partition coefficients. Goodness of fit is defined as $\chi^2 = \text{average} [(\ln D^{\text{data}} - \ln D^{\text{model}}) / \ln \sigma^{\text{data}}]^2$ per datum for Mg_{VIII}, Ca, Sr, and Ba molar partition coefficients and seven melt compositions.

| <i>Model</i> | <i>Fit Parameters</i> | χ^2 |
|--|-----------------------|----------|
| Anorthite (extrapolated mean), Blundy and Wood (1994) Calculate D_o from D_{Ca} , $r_o = 1.196(18) \text{ \AA}$, $E = 124.5(14.8) \text{ GPa}$ | 2 | 33 |
| <i>Mathematica</i> free parameterization: unique D_o , r_o , E solutions for partitioning data of each melt composition | 21 | 11 |
| $D_o \propto \gamma_{melt}^{CaO} a_{melt}^{Al_2O_3} (a_{melt}^{SiO_2})^2 e^{\Delta G_{fus}^o / RT}$ Melt major oxide correction to lattice strain model: D_o is product of major oxide activities and fit parameter (G) representing $e^{\Delta G_{ofus}/RT}$ $G = 4.095 \cdot 10^7$, $r_o = 1.22 \text{ \AA}$, $E = 151.3 \text{ GPa}$ | 3 | 15 |
| $D_o \propto \gamma_{melt}^{cation} a_{melt}^{Al_2O_3} (a_{melt}^{SiO_2})^2 e^{\Delta G_{fus}^o / RT}$ Empirical linear correction for D_{Sr} and D_{Ba} residuals. $G = 5.170 \cdot 10^7$, $r_o = 1.227 \text{ \AA}$, $E = 190.2 \text{ GPa}$, $\gamma_{melt}^{SrO} \approx (-0.385 - 0.690 X_{melt}^{MgO}) \gamma_{melt}^{CaO}$ $\gamma_{melt}^{BaO} \approx (0.568 - 1.933 X_{melt}^{MgO}) \gamma_{melt}^{CaO}$ | 7 | 2.7 |

(3) We can account for melt major oxide activities in D_o by simultaneously solving equation (2.11) for each partition coefficient in all seven melt compositions to minimize a sum of χ^2 . In this treatment, the activity coefficients of the cations in anorthite are assumed to be equal to 1 and oxide activity data comes from our reoptimization of the Berman CMAS liquid model. The remaining unknown quantity in equation (2.11) is a value for $e^{\Delta G_{ofus}/RT}$, termed “ G ,” which should remain constant across all seven

compositions. The three-parameter solution for G , E , and r_o generates an average χ^2 of 15.

(4) The residuals of the melt major element activity model (3) are attributed to nonideality of the trace species in the melts. Analytical resolution restricts observable dependence of these residuals on melt composition to linear relationships. However, including slope and intercept parameters for γ_{SrO} and γ_{BaO} relative to known γ_{CaO} as a function of melt X_{MgO} still considerably improves our model. The resulting seven-parameter model yields a $\chi^2 = 2.7$, a better fit with far fewer parameters than the free parameterization of each Onuma curve. Figure 2.5(c) shows the Sr and Ba partitioning data linearly corrected back onto the model Onuma curves as a function of X_{MgO} in the melt.

One should be cautious about using the γ_{MO} -corrected parameterization presented here as an exact, quantitative treatment of the trace cation activity coefficients in these melts. A seven-parameter system to fit these data is degenerate and thus the values of r_o and E influence the extent of correction for partitioning behavior we attribute to the influence of γ_{MO} . Parameters shown in Table 2.4 for this parameterization are a representative, rather than unique, solution. Furthermore, if future magnesium site occupancy data were to demonstrate that the original Berman melt model more accurately predicts magnesium site distributions in anorthite than the reoptimization employed here, the modeled E value for this data would decrease by approximately 20 GPa for both the three- and seven-parameter fits.

We also note a difficult philosophical issue concerning the meaning of the fit parameters r_o and E . Papers by Blundy, Wood and co-workers (Blundy and Dalton, 2000; van Westrenen et al., 2000) have developed models in which these parameters vary with liquid composition and so are not strictly descriptions of the properties of crystals alone. Yet these authors have noted the similarity both between fitted values of r_o and site radii from structure refinements and between fitted values of E and macroscopic Young's moduli from elastic data, both of the latter data types defining properties of the crystal in isolation. In this work, we remove melt thermodynamics and obtain good fits with values of r_o and E that are independent of melt composition and so could be properties of the isolated crystal, yet the resulting values do not match site radii and mineral elasticity. Neither of these outcomes is entirely satisfactory. It remains an open question whether it is appropriate to think of these parameters in terms of a direct physical interpretation rather than as free parameters of a successful model whose form was originally motivated by physical insight.

2.3.5 Calculating Activity Coefficients of Melt Trace Species

Understanding the precise activity coefficients of trace constituents in silicate liquids is essential to developing complete thermodynamic models of trace element distributions in magmatic systems (e.g., Hirschmann and Ghiorso, 1994). In our experiments, the residual misfit of observed D^{molar}_{Sr} and D^{molar}_{Ba} values to those predicted by the melt composition-modified crystal chemistry model is characterized by a negative slope as a function of melt MgO content. This qualitatively suggests that the activity

coefficients of these neutral trace element species decrease as melts become more magnesian.

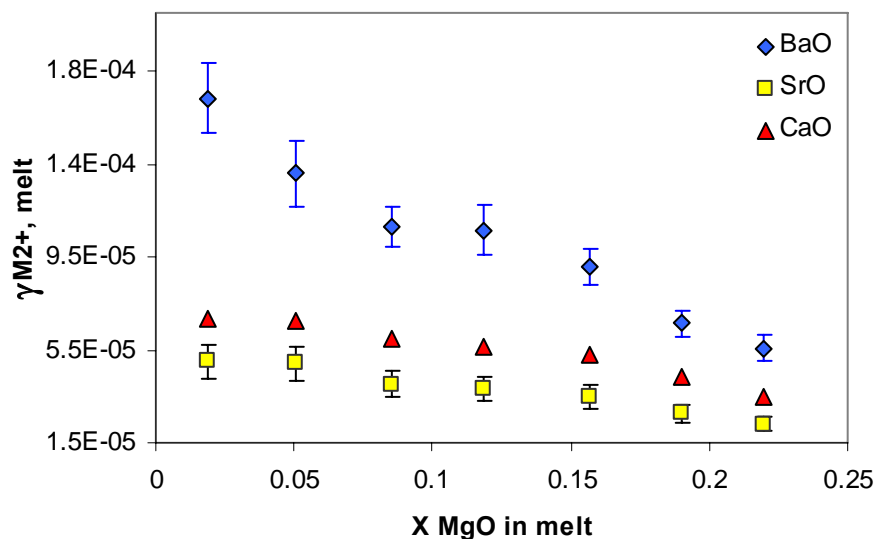


Figure 2.6. Calculated melt γ_{BaO} and γ_{SrO} values plotted with γ_{CaO} (from re-optimization of Berman model) for the seven liquid compositions of this study. Error bars are 1σ .

Without independently knowing the activity coefficients of BaO and SrO in the solid phase, γ_{BaO} and γ_{SrO} of the melts cannot be directly solved from equation (2.11). However, Henry's Law for these trace constituents in anorthite is equivalent to a constant value of the activity coefficient in the solid for each oxide, so most of the variation we see is attributable to changes in the melt activity coefficients. We can examine these relative changes by assuming ideal mixing (activity coefficient = 1) of these cations in anorthite. In this case, $\Delta G^{\circ}_{\text{fusion}}$ of anorthite can be calculated for each composition from $D^{\text{molar}}_{\text{CaO}}$ data and then relative values for the melt activity coefficients may be explicitly derived. The compositional trend for both SrO and BaO is similar to that given by the

original or re-optimized Berman models for CaO in our liquids, as shown in Figure 2.6, suggesting a similar network-modifying role in the melt phase.

Exchange equilibria provide additional support for the overall qualitative trends in divalent cation activity coefficients calculated above. The *equilibrium* exchange constant, $K_{D,eq}$, between anorthite and melt for an exchange reaction between Ca^{2+} and Ba^{2+} in coexisting anorthite and melt phases would be,

$$K_{D,eq}^{\text{anorthite/melt}} = \frac{a_{\text{Ca}^{2+}(\text{anorthite})} a_{\text{Ba}^{2+}(\text{melt})}}{a_{\text{Ca}^{2+}(\text{melt})} a_{\text{Ba}^{2+}(\text{anorthite})}} \quad (2.20)$$

On the other hand, the *observed* exchange partition coefficient $K_{D,obs}^{\text{anorthite/melt}}_{\text{Ca-Ba}}$ is defined as $D_{Ca}^{\text{molar}} / D_{Ba}^{\text{molar}}$. If the activity coefficients of the cations in the anorthite phase remain constant (i.e., Henry's Law behavior) and temperature is constant (making $K_{D,eq}^{\text{anorthite/melt}}$ a constant), then the expression for $K_{D,obs}^{\text{anorthite/melt}}_{\text{Ca-Ba}}$ may be reduced to,

$$K_{D,obs}^{\text{anorthite/melt}}_{\text{Ca-Ba}} = \text{constant} \cdot \frac{\gamma_{\text{Ca}^{2+}(\text{melt})}}{\gamma_{\text{Ba}^{2+}(\text{melt})}} \quad (2.21)$$

Plots of $K_{D,obs}^{\text{anorthite/melt}}$ for Ca-Sr, Ca-Ba, and Sr-Ba exchanges as a function of MgO content in the melt (Figure 2.7) suggest the same trends as the calculated $\gamma_{\text{MO,melt}}$ values in Figure 2.6. $K_{D,obs}^{\text{anorthite/melt}}_{\text{Ca-Sr}}$ varies little as the network modifying major element content of the melt becomes more magnesian, suggesting that $\gamma_{\text{CaO,melt}}$ and $\gamma_{\text{SrO,melt}}$ exhibit nearly identical behavior. $K_{D,obs}^{\text{anorthite/melt}}_{\text{Ca-Ba}}$ and $K_{D,obs}^{\text{anorthite/melt}}_{\text{Sr-Ba}}$ both increase significantly, meaning that γ_{BaO} in the melt systematically decreases relative to γ_{SrO} and γ_{CaO} as X_{MgO} increases. Calculated $\gamma_{\text{MO,melt}}$ values (Figure 2.6) from our hybrid melt thermodynamic-crystal chemistry treatment are consistent with this result. More extensive data of this type should allow a general parameterization of these trace activity coefficients in melts, and

hence, in combination with lattice strain theory for crystal chemical effects and major element melt-mineral equilibria for obtaining D_o , will provide the final link in a complete trace element partitioning model.

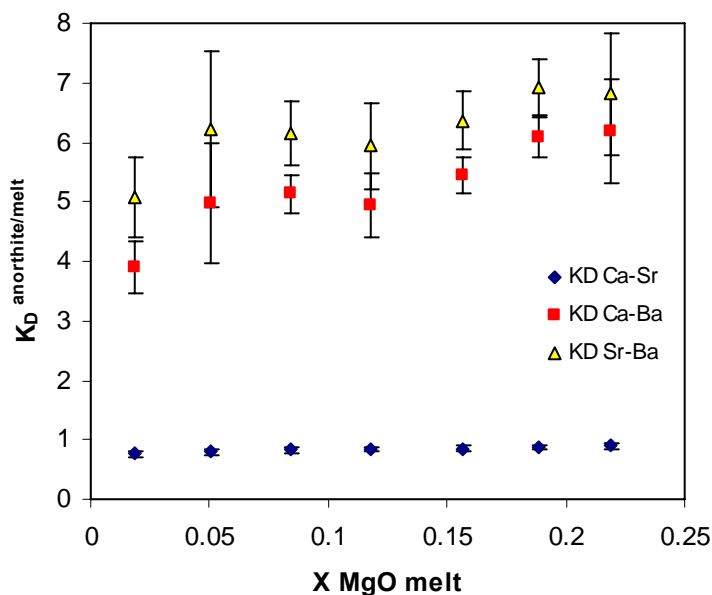


Figure 2.7. Exchange partition coefficients ($K_D = D^{molar}_{M1O}/D^{molar}_{M2O}$) for Ca-Sr, Ca-Ba, and Sr-Ba. Uncertainty is 1σ .

2.3.6 Melt Structure and Partitioning

Quantitative relationships between partitioning and melt properties have yet to be fully elucidated, though studies have attempted to relate partitioning behavior to both melt thermodynamics (Hirschmann and Ghiorso, 1994; Kinzler et al., 1990; O'Neill and Eggins, 2002) and structure (Gaetani, 2004; Kohn and Schofield, 1994; Kushiro and Walter, 1998; Mysen and Dubinsky, 2004). We have approached the problem with an empirical thermodynamic model of the melt, but we also wish to evaluate whether

structural information about the melt provides insight into the origin of the melt activity coefficient variations and their influence on partitioning.

The crystal chemical model of partitioning assumes that the strain imposed on a site within a liquid network by a substituting cation is negligible relative to the strain due to cation misfit on a crystal site. The quality of this assumption may vary with both the structure of the liquid and of the liquidus mineral. Calculation of an average non-ideal mixing chemical potential of BaO from melt γ_{BaO} plotted in Figure 2.6 yields $RT\ln\gamma_{\text{BaO}} = \sim 125$ kJ/mol at 1330 °C. The $\Delta G^{\circ}_{\text{exchange}}$ of Ba for the anorthite VIII-site calculated from the crystal chemical portion of our partitioning model is considerably smaller, ~ 40 kJ/mol, and therefore may have less control over partitioning behavior than would be predicted by a purely crystal chemical model.

Universal melt parameters may offer insights into melt structure as a whole and its effects on trace element partitioning. As shown in Table 2.3, the liquid compositions of this study are essentially isopolymerized in terms of the frequently used parameter NBO/T, representing the ratio of non-bridging oxygens to tetrahedrally coordinated cations in the melt (Mysen et al., 1982). Since NBO/T treats Al^{3+} and Si^{4+} as having identical implications for melt structure and the amounts of both in our melts vary only slightly, NBO/T is not, in this case, a useful parameter for relating our observed partitioning behavior to melt structural changes. However, optical basicity, which estimates the average electron cloud density around oxygen in a liquid (Duffy, 1993; Mills, 1993), varies systematically among our compositions, decreasing as the abundance of more polarizing Mg^{2+} cations increases relative to Ca^{2+} .

We find that the partitioning of all divalent elements considered here onto the anorthite VIII-fold coordination site (Figure 2.8) increases linearly with optical basicity of the melt.

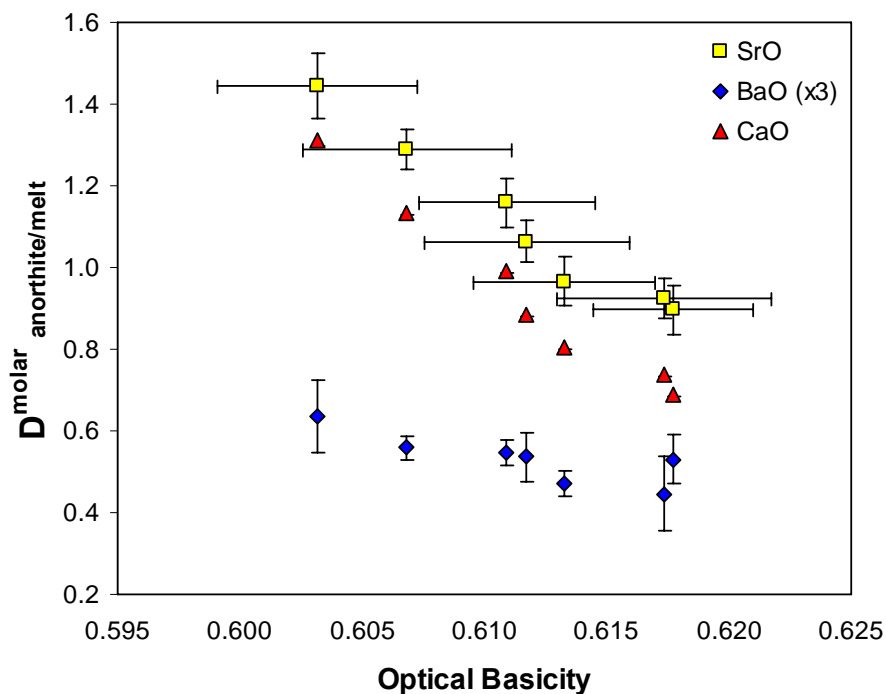


Figure 2.8. D^{molar} as a function of optical basicity (from Mills, 1993). 1σ uncertainty shown in brackets where uncertainty exceeds symbol size except in the case of optical basicity, where error bars have been omitted on CaO and BaO data points for clarity. $D^{\text{molar}}_{\text{BaO}}$ and associated errors are shown as x3 measured values.

The experimental compositions of this study vary primarily in Mg/Ca (0.05 to 1.2) and to a lesser extent Al/(Al+Si), which is 0.31 in the least magnesian composition and ranges up to 0.35. As melts become progressively magnesian at roughly constant Si and Al contents, more Mg might be forced to charge-balance Al, creating a less stable melt structure relative to that of more calcic compositions.

One consequence may be the formation of a wider range of coordination environments for network modifying cations. This would increase the number of magnesium cations in higher-coordinated melt sites that are energetically competitive with Ca for placement in VIII-fold coordination in anorthite. Studies in both silicate (Fiske and Stebbins, 1994) and aluminosilicate melts (George and Stebbins, 1998) indicate that Mg exhibits lower coordination when in melts composed of lower field strength cations. As the magnesium content of our melts increases, the average Mg coordination number may rise to near 6. Our calculations from melt major oxide thermodynamics predict that Mg increasingly populates the VIII-fold coordinated site of anorthite relative to IV-fold as melt MgO content increases. If the number of coordination sites in a melt were to progressively become more like the population present in a coexisting solid phase, energetic barriers to greater equilibrium substitution into the crystal structure would decrease. By this mechanism, increasingly magnesian melts would promote higher coordination of Mg in anorthite and contribute to changes in D^{molar}_{MgVIII} . Computer simulations of melt solution energies for a cation species suggest that melt coordination environments can significantly influence predicted partition coefficients (van Westrenen et al., 2000).

Another approach to characterizing melt structure considers the number of oxygen bonds available to network modifying cations. Local polymerization in silicate liquids is often described in terms of Q^n species, where n represents the number of bridging oxygens to which a tetrahedrally coordinated cation such as Si or Al is bound in the melt framework (Stebbins, 1995). Fully polymerized tetrahedral networks contain only Q^4 species in which each oxygen (BO) is bonded between two tetrahedral units, while fully

depolymerized networks are composed of Q^0 , or non-bridging oxygens (NBO). Spectroscopic investigation of the liquid structures in the CMAS system has been hampered by poor peak resolution, particularly at high temperature. However, study of alkali aluminosilicate melts (Mysen, 1997; Mysen, 1999) may yield qualitative insights into liquid structures in alkaline earth systems. In alkali aluminosilicates for this Al/(Al+Si) range at 1400 °C, approximately 70 % of the bonding environments are Q^4 , with perhaps 20 % as Q^3 and Q^2 ; less than 10 % of oxygens are Q^1 (Mysen, 1997). A slight trend towards formation of Q^4 and Q^2 at the expense of Q^3 units, creating a more disordered melt structure, may occur over our compositional range as Al/(Al+Si) increases according to the reaction,



However, any influence the minor Al/(Al+Si) change may exert on melt structure cannot be separated here from the potentially large influence of the major network modifying cations present, since greater magnesium content also has been implicated in increasing the number of Q^4 and Q^2 units in a melt. Hence our data are not necessarily inconsistent with the prediction of Mysen (2004) that network modifying trace element mineral-melt partition coefficients should show a negative correlation with melt Al/(Al+Si). Mysen and Dubinsky (2004) state that abundances of Q^n species are not only a function of melt polymerization, but also a function of ionization potential of the network modifying cations, which form energetically non-equivalent bonds with NBO according to their relative abilities to draw electrons from oxygen. Cations with smaller ionic radii and/or greater charge will form less stable bonds with NBO (mostly Q^3 species in these melts), and this stabilizes larger populations of Q^2 and Q^4 species according to

equation (2.22). This effect has been documented by Libourel et al. (1992), who observed increases in ^{29}Si peak shielding with magnesium content in CMAS glasses. They interpreted this as a possible consequence of a greater variety of Si sites available in the glass structure, which would translate into a greater range of Q^n speciation, as would occur when forming Q^2 and Q^4 species from Q^3 . Merzbacher et al. (1990) also noted that ^{29}Si peaks in MAS glasses were broader than those of CAS.

A wider distribution of oxygen species due to destabilization in melts of higher magnesium content may result in a greater abundance of coordination sites energetically comparable to those within the anorthite structure, which is composed of a purely Q^4 framework encasing larger VII-fold coordinated sites occupied by a divalent network modifying cation to charge balance Al^{3+} . In this scenario, all alkaline earth cations occupying such melt sites would partition more strongly into the anorthite structure as melts become more magnesian, as observed in this study.

2.4 CONCLUSIONS

We demonstrate that melt composition affects trace element partitioning behavior in a manner that can be systematically accounted for by projecting melt model refinements onto existing crystal lattice strain models of partitioning (Beattie, 1994; Blundy and Wood, 1994). Here our model relies on an empirical description of melt thermodynamics, but this approach to partition coefficient determination may be applied using any self-consistent thermodynamic melt model, such as MELTS in the case of natural compositions, providing that the mineral thermodynamics are well characterized.

Such a treatment shows promise in generating more accurate predictions of D values that would be costly or, in the case of short-lived radioactive elements, potentially hazardous to obtain experimentally. Our method also offers a means for isolating activity coefficient behavior of melt trace species. Such information has been hitherto inaccessible yet, as our study demonstrates, may often play a non-trivial role that should be incorporated into a complete model of trace element partitioning.

Chapter 3: Reoptimization of the Berman (1983) CMAS Liquidus Model in Anorthite Phase Space

3.1 INTRODUCTION

Accurate thermodynamic interpretations of partitioning between minerals and melts and their successful application to igneous processes are heavily dependent on the quality of major-element activity-composition models of melts in the compositional systems of interest. This chapter describes a targeted effort to improve the Berman (1983) CaO-MgO-Al₂O₃-SiO₂ thermodynamic melt model for use in studies of anorthite partitioning, such as that discussed in chapter 2. New Margules parameters are reported for melts between 40 and 50 mol % SiO₂ on the anorthite liquidus that reduce discrepancies between experimentally measured liquidus temperatures and those calculated from the model by 35 %.

3.1.1 Description of Berman CMAS Thermodynamic Melt Model

Two main approaches exist for describing the molecular interactions that govern energies of solution in melt systems: speciation and stoichiometric models (for a more detailed overview, see Berman and Brown (1987)). Speciation models, which are mathematically more complicated, attempt to identify all, or at least a representative critical mass of, molecular species present in the melt and incorporate as much nonideal mixing behavior into speciation as possible. Usefulness of this approach is often limited by not knowing melt species identities well and the lack of standard state property data

for many of them, so full treatments have been limited to simple, well studied binaries such as $\text{Na}_2\text{O-SiO}_2$ (e.g., Halter and Mysen, 2004). Less rigorous variations of this approach in more complex systems have approximated melt structure as consisting of one species similar to a coexisting mineral phase of interest, as in Blundy et al. (1996), or “two-lattice” models (e.g., Drake, 1976; Nielsen and Dungan, 1983) that treat melts as being composed of two independent quasi-lattices, each an ideal solution: a network-forming lattice of SiO_2 and aluminous species MAlO_2 and MAl_2O_4 (where M = a monovalent or divalent cation) and a network-modifying lattice on which oxides such as CaO , MgO , and FeO are evenly distributed.

In contrast, a stoichiometric model makes no assumptions about melt structure and instead designates a number of endmember components that encompass the entire compositional field of interest. Calculating melt energetics using these endmembers as fictive melt species is generally more mathematically tractable and one has greater flexibility in choosing components for which thermodynamic data exists. The extent to which the chosen endmember species do not represent the actual species present in the melt can be reflected in extremely non-ideal mixing behavior of these species in the model. For example, the CaO activity coefficients calculated using the Berman (1983) stoichiometric model in the CMAS melts of chapter 2 are on the order of 10^{-5} , indicating that very little Ca inhabits these melts as a simple oxide. Use of one or more species such as CaSiO_3 , CaAl_2O_4 , or $\text{CaAl}_2\text{Si}_2\text{O}_8$ might account for a greater amount of the solution energy associated with Ca molecules via their molar proportions alone.

The Berman model (1983) uses simple neutral oxides as fixed endmember components and parameterizes melt activities for each oxide as a function of composition

and temperature, with enthalpy and entropy excess mixing terms (Margules parameters) fitted to liquidus relations. The Gibbs free energy of a solution can be described as the sum of two parts: the free energy associated from ideal mixing behavior of a species in the melt, which depends only on the concentration of the species, and the energy arising from non-ideal mixing, here termed “excess”:

$$\Delta G_{solution} = \Delta G_{ideal} + \Delta G_{excess} . \quad (3.1)$$

The excess Gibbs free energy of the system may be described with the following expression for any number (nc) of components (i), where X is the molar fraction, T is the absolute temperature, R is the gas constant, and γ is the activity coefficient:

$$\Delta G_{excess} = \sum_{i=1}^{nc} X_i RT \ln \gamma_i . \quad (3.2)$$

In the case of the quaternary system CaO-MgO-Al₂O₃-SiO₂ (CMAS), there are 31 different mixing combinations of the four end-member oxide components, with an enthalpy term (W_H) and entropy term (W_S) for each. The general Margules term, W , used in the model represents a simple relationship incorporating both, along with a temperature term. For a given combination of mixing components i , the expression for W is:

$$W_i = W_{H_i} - TW_{S_i} . \quad (3.3)$$

The Berman model empirically approximates liquid excess free energy of a liquid species using the general polynomial expression,

$$RT \ln \gamma_m = \sum_{i_1=1}^{nc-1} \sum_{i_2=i_1}^{nc} \dots \sum_{\substack{i_p=i_{p-1} \\ i_p \neq i_1}}^{nc} W_{i_1 i_2 \dots i_p} \left[Q_m X_{i_1} X_{i_2} \dots X_{i_p} / X_m + (1-p) X_{i_1} X_{i_2} \dots X_{i_p} \right] . \quad (3.4)$$

Here m is the oxide component of interest, p is the degree of polynomial, Q_m is the number of times the liquid oxide (m) appears in a particular mixing interaction, and X is the mole fraction of a component in the liquid of interest. The activity coefficient of oxide component m in a quaternary system may be calculated from the fourth degree polynomial expression of the general equation above:

$$\gamma_m = \exp \left[\left(\sum_{i_1=1}^3 \sum_{i_2=i_1}^4 \sum_{i_3=i_2}^4 \sum_{\substack{i_4=i_3 \\ i_4 \neq i_1}}^4 W_{i_1 i_2 i_3 i_4} [Q_m X_{i_1} X_{i_2} X_{i_3} X_{i_4} / X_m - 3 X_{i_1} X_{i_2} X_{i_3} X_{i_4}] \right) / RT \right]. \quad (3.5)$$

Instead of employing regression fitting to minimize residuals over the entire data set, the approach used in Berman model fits the data via linear programming to maintain the uncertainty consistency associated with each data point. Specifics of model calibrations are discussed in detail in Berman and Brown (1984) as well as Berman (1983).

3.2 MODEL PERFORMANCE

In order to more confidently quantify liquid thermodynamic effects on partitioning behavior for the data of chapter 2, it was highly desirable to determine the accuracy of the Berman CMAS model within the anorthite liquidus phase volume near the compositional range of seven CMAS compositions of interest (as shown in Figure 2.1). Model performance was evaluated by testing its ability to predict anorthite liquidus temperatures. Before proceeding, it should be noted that this work uses the correct values for ternary SAMM (SiO₂-Al₂O₃-MgO-MgO) interaction parameters that were printed as typos duplicating the values of SSAM reported in both the original thesis (1983) and De

Capitani and Brown (1987). The actual values for W_H and W_S for the SAMM interaction are 652384.49 and 397.38, respectively (J. Beckett, personal communication).

3.2.1 Calculating Anorthite-Melt Liquidus Temperatures from the Berman Model

At equilibrium on the anorthite liquidus, the chemical potential (μ) of pure anorthite equals the chemical potential of anorthite component in the coexisting melt phase, as shown in equation (3.6). The chemical potential of each phase is composed of both standard state (μ^0) and excess energy ($RT\ln a$) terms:

$$\sum_{i=1}^3 \rho_i \left[\mu_i^{o,\text{Liq}} + RT \ln(X_i^{\text{Liq}} \gamma_i^{\text{Liq}}) \right] = \mu_{\text{anorthite}}^o + RT \ln a_{\text{anorthite}} \quad (3.6)$$

The stoichiometric coefficient for oxide i in the anorthite formation reaction is represented by ρ_i . Activity coefficients for the liquid oxide components are calculated from equation (3.5), whereas the activity of anorthite of the solid phase is assumed equal to 1 (that is, the anorthite is assumed pure). Standard state chemical potential is described by the expression,

$$\mu^o = \Delta H_f^o + \int_{298.15}^T C_p dT - T \left[\Delta S^o + \int_{298.15}^T \frac{C_p}{T} dT \right]. \quad (3.7)$$

Heat capacities are calculated according to the following four term heat capacity equation used in Berman (1983):

$$C_p = A + CT^{-2} + DT^{-0.5} + FT^{-1} \quad (3.8)$$

The anorthite and liquid component heat capacity equation coefficients used are listed in Table 3.1.

Table 3.1. Anorthite and liquid oxide component standard state properties and heat capacity equation coefficients from Berman (1983).

| | $\Delta H_f^{298.15, 1 \text{ bar}}$ J/mol | $\Delta S^{298.15, 1 \text{ bar}}$ J/mol | Heat capacity (C_p), J/mol·K | | | |
|---------------------------------------|---|---|----------------------------------|----------|-----------|-----------|
| | | | A | C | D | F |
| Anorthite | -4231480 | 199.90 | 422.521 | -2189052 | -3219.938 | - |
| CaO liquid | -554897 | 26.228 | 76.044 | - | - | - |
| Al ₂ O ₃ liquid | -1548481 | 102.785 | 154.820 | - | -677.889 | -8071.355 |
| SiO ₂ liquid | -904927 | 45.000 | 121.630 | - | -1444.383 | - |

The success of the Berman model can be assessed by comparing the liquidus temperatures it predicts for various melt compositions coexisting with pure anorthite with those observed experimentally for those compositions. The reported uncertainty in anorthite liquidus temperatures based on the calibration data used by Berman (Berman, 1983) for the 20 wt. % Al₂O₃ plane of the quaternary, near our region of interest, exceeded 20 °C. The need for an accurate set of liquid activity coefficient and anorthite liquidus temperatures for the experimental protocol described in chapter 2 of this thesis motivates our attempt at a Margules parameterization refinement specifically to reduce this uncertainty. Furthermore, a plot (Figure 3.2a) of liquidus temperature discrepancies between the model and experiments in which anorthite coexists with CMAS melts between 40–50 mol % SiO₂ revealed an positive correlation of the temperature residual with the melt CaO content. No similar systematic relationships between ΔT_L and the other melt oxide components MgO, Al₂O₃, and SiO₂ emerged. While these discrepancies generally fall within expected model performance, they suggest that some degree of melt

behavior is left unaccounted for by the Berman model that might be recovered by a targeted reoptimization of the model within our compositional range of interest.

3.3 REOPTIMIZATION OF BERMAN MODEL

3.3.1 Data Selection

A reoptimization of the Berman model was performed within the 40–50 mol % SiO₂ portion of the anorthite liquidus space in the system CMAS. This was accomplished by adjusting the Margules parameters to minimize the differences between the liquidus temperatures predicted by the model and those experimentally determined for anorthite in 57 CMAS liquids with SiO₂ content between 40 and 50 mol % (Chapter 2, Osborn, 1942; Osborn and Tait, 1952; Tsuchiyama, 1983; Yang et al., 1972). Compositions and observed liquidus temperatures are listed in Table 3.2. These data all constrained the anorthite liquidus to within 5 °C, thus offering sufficient precision for use in this modeling. Several other studies (Anderson, 1915; DeVries and Osborn, 1957; Osborn et al., 1954; Prince, 1954) contain an additional 61 points in CMAS-anorthite liquidus space, but the bulk of these data falls outside the composition region of interest and are thus not selected for this model reoptimization. DeVries and Osborn (1957) compositions all contain significantly more alumina, whereas the Anderson (1915), Osborn et al. (1954), and Prince (1954) data sets tend to have >50 % molar SiO₂.

Table 3.2. Literature anorthite-CMAS melt liquidus data from composition region ~40–50 mol % SiO₂.

| Source | T _L , ° C* | X CaO | X MgO | X Al ₂ O ₃ | X SiO ₂ |
|------------------------|-----------------------|-------|-------|----------------------------------|--------------------|
| CMAS2 (Chapter 2) | | | | | |
| | 1403 | 0.207 | 0.159 | 0.151 | 0.483 |
| | 1408 | 0.228 | 0.142 | 0.144 | 0.487 |
| | 1408 | 0.250 | 0.119 | 0.141 | 0.490 |
| | 1408 | 0.277 | 0.093 | 0.137 | 0.493 |
| | 1400 | 0.300 | 0.068 | 0.134 | 0.498 |
| | 1401 | 0.322 | 0.040 | 0.133 | 0.504 |
| | 1398 | 0.345 | 0.014 | 0.132 | 0.508 |
| Tsuchiyama (1983) | | | | | |
| | 1270 | 0.257 | 0.160 | 0.089 | 0.494 |
| | 1360 | 0.253 | 0.122 | 0.126 | 0.499 |
| Yang et al. (1972) | | | | | |
| | 1257 | 0.281 | 0.187 | 0.102 | 0.431 |
| | 1276 | 0.263 | 0.196 | 0.110 | 0.432 |
| | 1264 | 0.282 | 0.183 | 0.103 | 0.432 |
| | 1252 | 0.288 | 0.178 | 0.102 | 0.432 |
| | 1299 | 0.258 | 0.190 | 0.117 | 0.435 |
| | 1294 | 0.269 | 0.180 | 0.115 | 0.436 |
| | 1254 | 0.313 | 0.149 | 0.102 | 0.436 |
| | 1304 | 0.276 | 0.164 | 0.120 | 0.439 |
| | 1335 | 0.260 | 0.169 | 0.130 | 0.441 |
| | 1355 | 0.281 | 0.134 | 0.136 | 0.448 |
| | 1399 | 0.241 | 0.149 | 0.158 | 0.452 |
| | 1366 | 0.311 | 0.094 | 0.140 | 0.455 |
| | 1411 | 0.277 | 0.104 | 0.160 | 0.460 |
| | 1443 | 0.233 | 0.116 | 0.186 | 0.465 |
| | 1437 | 0.267 | 0.091 | 0.176 | 0.466 |
| Osborn and Tait (1952) | | | | | |
| | 1325 | 0.192 | 0.218 | 0.128 | 0.461 |
| | 1448 | 0.201 | 0.130 | 0.201 | 0.468 |
| | 1305 | 0.202 | 0.211 | 0.119 | 0.468 |
| | 1444 | 0.216 | 0.122 | 0.186 | 0.477 |
| | 1392 | 0.216 | 0.148 | 0.158 | 0.478 |
| | 1353 | 0.217 | 0.172 | 0.132 | 0.478 |
| | 1296 | 0.218 | 0.196 | 0.108 | 0.479 |
| | 1291 | 0.221 | 0.195 | 0.103 | 0.481 |
| | 1288 | 0.225 | 0.194 | 0.098 | 0.483 |
| | 1287 | 0.228 | 0.186 | 0.101 | 0.485 |
| | 1280 | 0.228 | 0.191 | 0.096 | 0.485 |
| | 1498 | 0.232 | 0.048 | 0.232 | 0.488 |
| | 1280 | 0.234 | 0.187 | 0.089 | 0.490 |
| | 1297 | 0.237 | 0.177 | 0.094 | 0.492 |

Table 3.2. (continued)

| Source | $T_L, ^\circ\text{C}^*$ | X CaO | X MgO | X Al ₂ O ₃ | X SiO ₂ |
|---------------|-------------------------|-------|-------|----------------------------------|--------------------|
| Osborn (1942) | 1239 | 0.333 | 0.084 | 0.083 | 0.500 |
| | 1263 | 0.328 | 0.084 | 0.087 | 0.500 |
| | 1258 | 0.342 | 0.070 | 0.088 | 0.500 |
| | 1288 | 0.371 | 0.029 | 0.101 | 0.500 |
| | 1323 | 0.250 | 0.141 | 0.109 | 0.500 |
| | 1333 | 0.276 | 0.113 | 0.110 | 0.500 |
| | 1337 | 0.303 | 0.086 | 0.111 | 0.500 |
| | 1333 | 0.330 | 0.058 | 0.112 | 0.500 |
| | 1328 | 0.358 | 0.029 | 0.113 | 0.500 |
| | 1323 | 0.386 | 0.000 | 0.114 | 0.500 |
| | 1388 | 0.250 | 0.115 | 0.135 | 0.500 |
| | 1393 | 0.277 | 0.087 | 0.136 | 0.500 |
| | 1398 | 0.305 | 0.059 | 0.137 | 0.500 |
| | 1398 | 0.333 | 0.030 | 0.138 | 0.500 |
| | 1438 | 0.250 | 0.089 | 0.161 | 0.500 |
| | 1463 | 0.335 | 0.000 | 0.165 | 0.500 |
| | 1488 | 0.250 | 0.061 | 0.189 | 0.500 |
| | 1498 | 0.279 | 0.031 | 0.191 | 0.500 |
| | 1510 | 0.308 | 0.000 | 0.192 | 0.500 |
| | 1533 | 0.250 | 0.031 | 0.219 | 0.500 |

* Where liquidus are bracketed by an experiment at temperature T_1 where only glass is present and T_2 where both anorthite and glass are observed, the liquidus is assumed to be the average of T_1 and T_2 .

3.3.2 Model Reoptimization Procedure and Results

The reoptimization process involved a very simple program making iterative adjustments to the 62 Margules parameters, term by term, to find new parameters that minimize the sum of squares of liquidus temperature differences between the observed experimental data set and those predicted by the evolving thermodynamic model. Specifically, the program changes a Margules parameter by increasing or decreasing it incrementally and recalculates the liquid oxide component activities according to the new parameter value. New liquidus temperatures are calculated after each parameter value

adjustment such that $\Delta\mu_{\text{anorthite}} = \Delta\mu_{\text{anorthite liquid}}$ for all the data compositions being modeled. When a minimum is found for the one-dimensional search along a given parameter direction (that is, when adjustments to the parameter value become smaller than 0.1% of the value), the program accepts the new value and proceeds to search for the optimum value of the next Margules parameter. This term-by-term search is not optimal for finding a global minimum in multi-parameter space, but that is not a reasonable goal when optimizing a 62-parameter model to 57 experimental constraints. Instead this computationally straightforward method is sufficient for seeking incremental improvements relative to the starting model without any claim to uniqueness of the solution.

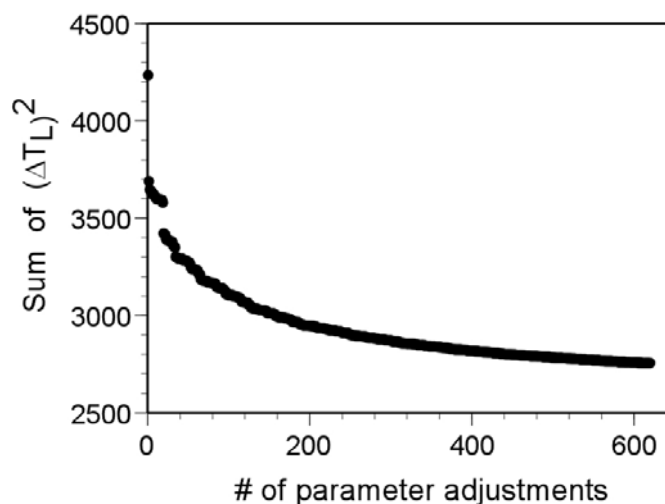


Figure 3.1. Reduction of the sum of differences squared between experimental measurements of liquidus temperatures and those calculated from the model $(\Delta T_L)^2$ as a function of the number of Margules parameter adjustments made during reoptimization of the Berman model.

It is important to recognize that this reoptimization considered only anorthite-melt constraints and is presumed to be worse than the original Berman model at describing not only equilibria with other solids but potentially portions of the anorthite liquidus outside the compositional range of experimental liquidus data selected. However, the reparameterization successfully eliminates the apparent systematic dependence of liquidus temperature errors on melt CaO content in this compositional region, as shown in Figure 3.2.

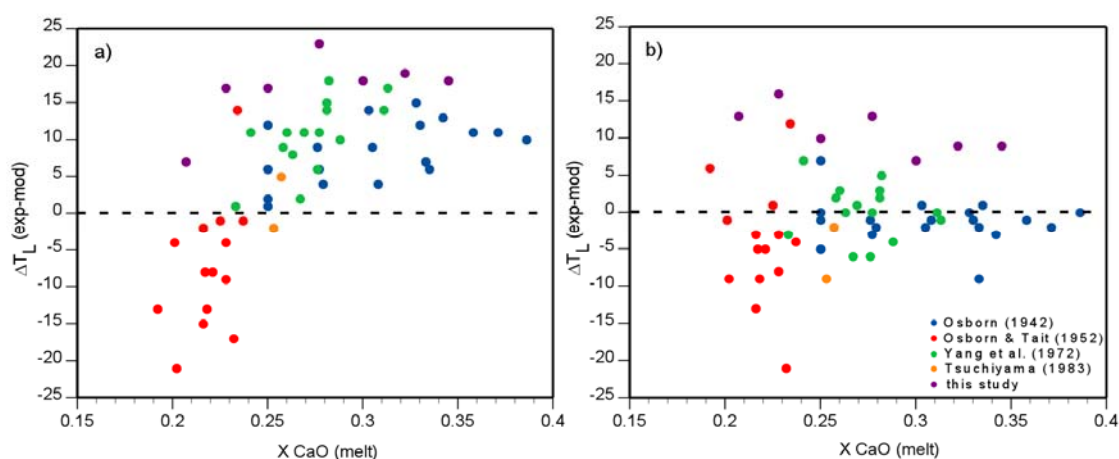


Figure 3.2. Difference between anorthite liquidus temperature (ΔT_L) as a function of molar melt CaO content as measured experimentally (exp) and calculated by thermodynamic model (mod): (a) Berman (1983) CMAS activity model, and (b) after reoptimization of Berman model using CMAS experimental literature data shown.

3.3.3 Discussion

Vulnerability to systematic errors is a known disadvantage of stoichiometric melt models (Beckett, 2002), and this effect can be significant when applying them to other thermodynamic modeling efforts. This is illustrated by the exercise in chapter 2 of this thesis, where the two sets of Margules parameters discussed here generate distinctly different predictions of Mg site occupancy (tetrahedral vs. octahedral/cubic) for

anorthites coexisting with CMAS melt compositions (see Figure 2.4). Molar D_{MgVIII} values calculated from the Berman model exceed those of the reoptimized model by a factor of ~ 3 . A detailed spectroscopic study of Mg site distribution in anorthite might definitively indicate whether the reoptimized melt model produces a more accurate description of Mg in the crystal structure. As no such site occupancy data currently exist, improvements in liquidus temperatures within a subregion of the anorthite phase volume remain the sole justification for using this reoptimization to thermodynamically rationalize the divalent cation partitioning data of chapter 2.

Chapter 4: Experimental Techniques for Radium Partitioning Measurements

4.1 INTRODUCTION

The partitioning of radium into a major crustal constituent such as feldspar has important implications for deciphering the evolution and transport histories of young magmas, yet no experimental radium partitioning data exist for any mineral. This chapter discusses experimental and analytical approaches used to overcome the technical and safety challenges inherent to investigating partitioning behavior of the geologically short-lived radioactive isotope ^{226}Ra , which has a half-life of 1600 years and thus is over a million times more radioactive than the most abundant uranium isotope, ^{238}U (Figure 4.1). Here I outline the rationales for selection of the system composition, preparation of starting materials, and analytical method. Procedures used for handling the materials are detailed, as well as the design of a flow line to remove radioactive ^{222}Rn from gas exiting the furnace during experiments. Also described are post-experiment furnace contamination measurements and their implications for greater understanding of radium volatility. Experimental partitioning data for radium are discussed in chapter 5.

4.1.1 Crystal Chemical Model Prediction of Radium Partitioning in CMAS

The difficulty of experimentally determining Ra partitioning behavior has forced past workers to use Ba as a proxy, either by assuming barium partitioning behavior to be a perfect analogue (e.g., Condomines et al., 1995; Schaefer et al., 1993; Volpe and Hammond, 1991) or by extrapolating D_{Ra} from lattice strain models of partitioning.

Blundy and Wood (1994) demonstrated that cation partitioning behavior is often strongly and systematically dependent on ionic radius and resulting degree of fit or misfit into particular lattice sites. The difference between Ba, 1.42 Å in VIII-coordination (Shannon, 1976) and Ra (1.48 Å) leads to significantly predictions of Ra partition coefficients considerably lower than Ba. Accounting for this difference has notable implications for understanding the timescales of any magmatic process occurring within 8000 years, or five half-lives of ^{226}Ra . Failing to recognize the greater incompatibility of Ra relative to Ba in magmatic systems experiencing plagioclase crystallization produces an apparent crystallization age older than that of the actual event (Condomines et al., 2003). Cooper et al. (2001) showed the significance of this effect in the case of the 1955 Kilauea east rift plagioclases, which likely crystallized near the same time as the augite phenocryst population in this system, yet a ^{226}Ra - ^{230}Th mineral isochron model assuming $D_{\text{Ra}}/D_{\text{Ba}} = 1$ would suggest the plagioclase crystallized 8000 years earlier. Given the demonstrated age uncertainties that these different estimates of D_{Ra} can imply in such systems, experimental determination of D_{Ra} would provide an important test of lattice strain model predictions for radium partitioning.

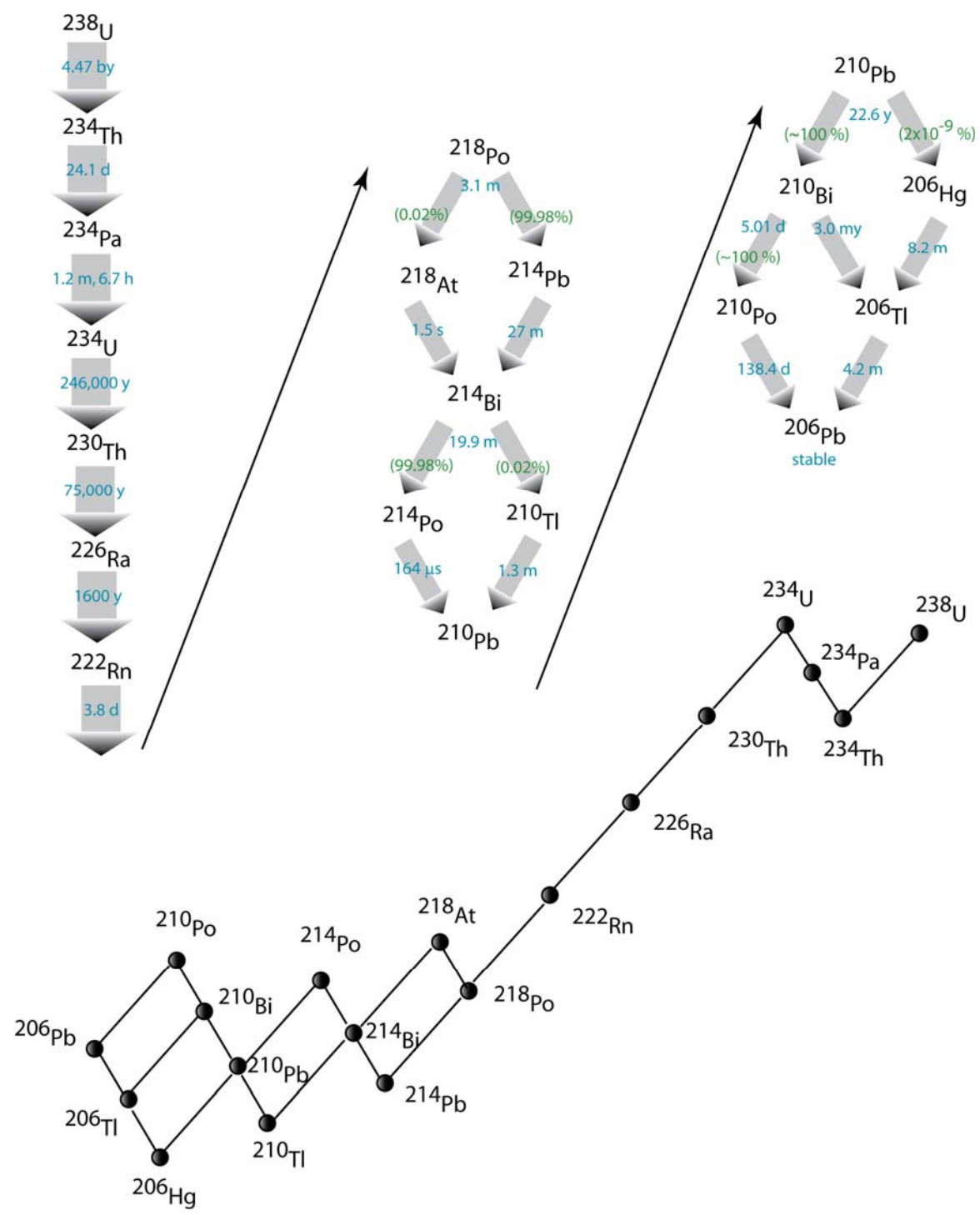


Figure 4.1. ^{238}U decay series ending in stable ^{206}Pb , with half-lives shown in light blue and % of daughter products produced (when several are possible) shown in green. Adapted from Parrington et al. (1996).

4.1.2 Analytical Method Considerations

Experimentally determined partition coefficients for radioactive elements such as U and Th have been measured by a range of analytical techniques including alpha and fission track radiography, proton-induced X-ray emission, laser ablation inductively coupled plasma mass spectroscopy (LA-ICP-MS), and secondary ion mass spectrometry (SIMS) (for a review, see Blundy and Wood, 2003a). Estimates of ^{226}Ra bulk and mineral/glass partition coefficients in natural samples may also be made by separating minerals from coexisting groundmass, digesting the samples, and measuring trace amounts of radioactive elements by isotope dilution thermal ionization mass spectrometry (TIMS) (e.g., Cooper et al., 2003; Cooper and Reid, 2003; Cooper et al., 2001; Rogers et al., 2004; Turner et al., 2003; Volpe and Hammond, 1991). Apparent D_{Ra} have also been obtained for leucite phenocrysts and groundmass by high resolution γ -spectrometry (Voltaggio et al., 2004). Such analyses can require tens to hundreds of grams of material (Condomines et al., 1995; Simpson and Grun, 1998). ^{226}Ra content determination for mineral and whole rock separates by ^{222}Rn emanometry also requires sample materials on the order of a gram (Schaefer et al., 1993).

Although destructive analytical techniques such as TIMS can detect very low amounts of ^{226}Ra (fg/g) in materials, *in situ* analysis was deemed a more suitable approach for accurately measuring radium in experimental run products of this study, given that the modest amount (<5 mg) of crystallized mineral material produced during an experiment would be difficult to cleanly separate from the coexisting glass phase and the extraordinary sensitivity of the measurement of very small partition coefficients to such contamination. The $\sim 2.5 \mu\text{Ci}$ of ^{226}Ra stock available to us made determining

plagioclase/melt partition coefficients by both alpha track radiography and SIMS potentially practicable.

4.1.2.1 Alpha Track Radiography Feasibility Tests

Alpha track radiography has the advantage of allowing *in situ* analysis of experimental samples, which relies neither on the cleanliness of natural material separates nor on the assumptions needed to derive a liquid composition from a groundmass or whole rock analysis. However, alpha track counting must be restricted to regions at least some critical distance from phase boundaries, depending on the alpha particle energies, to ensure that tracks collected at the sample surface did not originate at depth from a neighboring phase (LaTourrette, 1993).

As many radioactive elements of geologic interest belong to complicated decay chains (such as shown in Figure 4.1), there always exists a degree of uncertainty as to which tracks are produced by the decay of a particular element of interest. If one knows the abundances of each radioactive element in a sample, the track population corresponding to each can be calculated and accounted for when measuring a partition coefficient. The quantity of radium available for this study was obtained from Isotope Products in July of 1991, at which time the activity ratio of $^{210}\text{Pb}/^{226}\text{Ra}$ was reported as 4.8 %.

Since our radium starting solution contained a modest population of ^{226}Ra daughter product ingrowth, we needed to determine if those daughters would volatilize and depart the sample over the course of a controlled cooling experiment, which would

provide a clean initial condition for counting tracks produced by ^{226}Ra and a known quantity of daughter products at any point after the experiment. Several reconnaissance runs were performed to approximate the volatility of the longest-lived ^{226}Ra daughter nuclides ^{210}Pb ($t_{1/2} = 22.6$ years) and ^{210}Bi ($t_{1/2} = 5$ days) using an aliquot of CMAS1-1 composition material spiked with 2500 ppm Pb and 2500 ppm Bi. Volatility was not assessed for ^{210}Po , since Po lacks a stable isotope. Run products were analyzed on a JEOL 733 electron microprobe at Caltech; PbS and bismuth metal served as standards and beam conditions were 20 keV and 30 nA. Counting times were 30 s on the peaks and 15 s for background positions.

Compared to a 15 min glass fuse within a sealed 3 mm diameter platinum capsule (run 1-1-8), glass from an 86 hour open-furnace wire-loop dynamic crystallization experiment (run 1-1-7) contained no lead and 25 % of the initial bismuth. A 48 hr crystallization experiment (run 1-1-10) in an open graphite capsule under C/CO atmospheric conditions lost 90 % Pb and 45 % Bi, though measurement uncertainties (standard error of the mean) were somewhat large at 20 % and 35 % of the average glass totals for each element, respectively. Ideally, a quenched sample at the end of an experiment would have no significant population of alpha emitters except for ^{226}Ra so that all alpha tracks measured on film from the sample might be attributed to that one isotope. These Pb and Bi experiments indicated variable degrees of volatilization that could complicate interpretation of the alpha track population densities of both anorthite and glass when using alpha track radiography to determine radium partitioning.

4.2 STARTING MATERIAL PREPARATION

Given the complications for alpha track radiography associated with incomplete volatilization of daughter products over the course of the favored dynamic crystallization thermal regime for anorthite growth, we chose to measure radium partitioning behavior by ion probe. Major and trace element composition of starting materials were then picked specifically to maximize the fraction of the mass 226 signal attributable to ^{226}Ra during SIMS analyses.

4.2.1. Composition Selection

Selecting the optimal starting material composition for radium partitioning experiments from seven CMAS compositions (as described in chapter 2) relied on several factors. To maximize the amount of Ra available for detection in the anorthite crystals, one might choose CMAS2-7, the most magnesian composition. As a divalent cation with ionic radius of 1.42 Å in VIII-fold coordination, Ra^{2+} certainly enters the M-site of anorthite along with Ca, Sr, and Ba. Anorthite/melt partition coefficients presented in chapter 2 clearly demonstrate an increase in partitioning into the anorthite phase with increasing magnesium content of the coexisting CMAS liquid. However, the modest decrease in Ba D^{molar} values (0.21 ± 0.02 to 0.18 ± 0.2) from the CMAS2-7 to CMAS2-1 compositions suggests that this is a minor consideration, and if for other reasons the least magnesian composition (CMAS2-1) is preferred we should still be able to determine the lowest expected $D^{\text{molar}}_{\text{Ra}}$ in this suite of compositions.

The accuracy of SIMS analyses can be compromised by the presence of ion clusters in the mass range of the cation of interest, especially for abundances near the detection limit of the instrument. The extent of this effect at mass 226 is unknown, so potential clustering of ions was estimated using the Excel macro "ClusterCalc," supplied by Ian Hutcheon and written by Ross Williams (Analytical & Nuclear Chemistry Division, LLNL), which utilizes the programming of O. Eugster et al. (1985). Gold coating was avoided to prevent possible mass 226 interference from ion clusters of ^{197}Au and ^{29}Si , since nearly 5 % of silicon in the sample exists as ^{29}Si (Parrington et al., 1996). By considering a population of H, C, O, Mg, Si, Al, Ca, Sr, and Ba ions, a mass tolerance window of 1.5, and a maximum cluster charge of 1, the most likely mass 226 interferences would result from two-ion clusters of various Ba and Sr isotope combinations. To minimize this potential interference, the starting material was doped with ~100 ppm Ba and ~100 ppm Sr, a factor of 30 lower in the case of Ba than the amount used for the partitioning studies of chapter 2. Less likely three-ion clusters might involve addition of hydrogen to Ba-Sr clusters. Magnesium isotopes featured prominently in a number of possible four ion clusters and thus the least magnesium rich of our CMAS2 compositions, 2-1, was selected for use in our radium partitioning study.

No standard exists for radium, so radium content must be determined by comparing the measured abundance of ions detected at mass 226 for a sample with known non-zero radium concentration to an otherwise identical sample lacking radium, following the method of Brennan et al. (1995). Doping a 150 mg aliquot of starting material with approximately 1 μCi of ^{226}Ra would produce a mixture with roughly 1 ppm RaO. If the anorthite-melt radium partition coefficient were ~0.1, the SIMS would need

to accurately detect concentrations on the order of 100 ppb Ra in the anorthite phase in order to determine a partition coefficient. Here we document the procedure for making such a standard; ion probe sensitivity tests showing that this abundance is sufficient for successful measurements follow in the next chapter.

4.2.2 ^{226}Ra Solution Preparation

Source material for radium in this experiment was a reported 1 μCi of ^{226}Ra in 0.1 mL of 1 M HNO_3 from Isotope Products Laboratories. Daughter products had been separated from the ^{226}Ra in December 1989 resulting in a reported $a_{\text{Pb}}/a_{\text{Ra}}$ of $\sim 4.8\%$ as of July 1, 1991. The seal on the glass vial containing the radium solution was broken at some point prior to March 2005 and the solution had completely dried, likely leaving a $\text{Ra}(\text{NO}_3)_2$ salt residue. The remaining radium salt was resolubilized in 1 mL 5 M nitric acid by shaking vigorously under a heat lamp. The solution was transferred to a sterile 2 mL polypropylene NALGENE cryogenic vial with a 1 mm thick wall.

Gamma spectra of the solution in the plastic vial were collected in the Safety Office of the California Institute of Technology using a GEM 30P high purity germanium coaxial detector and ORTEC DSPEC jr digital gamma-ray spectrometer. Data were processed with GammaVision-32 gamma ray spectrum analysis software. Gamma rays from the vial were counted over a 1 hour period to obtain a spectrum. Approximately 94.45 % of ^{226}Ra α -decays go directly to the ^{222}Rn ground state, but the remaining 5.55 % of the decays go to the 2+ excited state, which returns to the ground state by release of a 186.2 keV gamma ray.¹ This 186 keV peak, the most intense of the ^{226}Ra

¹ Based on NNDC/BNL 5/1/2000 data compiled in the Idaho National Laboratory gamma-ray spectrum catalogue.

gamma ray energy spectrum, was compared to that detected from a 5 μCi standard ^{226}Ra source over an equal period of time. The 5 μCi standard is uncertified and therefore has a presumed uncertainty of 15 %. The spectrometer measured $2.6 \pm 0.4 \mu\text{Ci}$ of ^{226}Ra from the vial.

4.2.3 ^{226}Ra -Spiked Starting Material Preparation

Starting material consisted of 0.5 g of CMAS2-1 composition powder spiked with 150 ppm Ba and 100 ppm Sr according to the procedures described in chapter 2. A 150 mg aliquot of this material then was doped with ^{226}Ra by emptying the 1 mL contents of the polypropylene vial onto a Teflon watch glass and reducing the size of the solution drop under a heat lamp in a fume hood of the Caltech Isotope Lab. Four 1 mL washes of the vial using heated 5 M HNO_3 and vigorous shaking were added to the watch glass bead and subsequently reduced under heat until the remaining bead attained a diameter of ~ 0.8 cm. Gamma counting of the empty vial confirmed that no significant ^{226}Ra remained in the vial. The 150 mg of starting material was added to the reduced solution bead in a glove box in the same hood and mixed with a Teflon coated spatula. Several drops of 2 % polyvinyl alcohol aqueous solution were added to the mixture, which was formed into a large bead and transferred onto a circular mesh of platinum wire suspended from an alumina rod to be lowered into a vertical muffle furnace.

The bead exterior remained wet after an intended overnight drying period, so the bead was hung for two hours at the top of Deltech furnace muffle tube, where it dried at ~ 220 °C under compressed air flow. It was then lowered into the hot spot of the furnace and the furnace temperature was raised to 1440 °C where the bead fused for three hours.

The fused material was air quenched by turning off the compressed air flow and removing the bead from the top of the furnace.

4.3 EXPERIMENTAL DESIGN

4.3.1 Furnace Setup for ^{226}Ra Experiments

The primary safety objective of conducting radium partitioning experiments for ion probe analysis is containment of the radioactive radium and daughter products that are emitted from the charge over the course of an experiment. ^{226}Ra decays by alpha particle emission to ^{222}Rn gas, which has a half-life of 3.8 days. Assuming that radium volatility is negligible at 1400 °C at atmospheric conditions, the challenge lies in trapping the radon released from the sample material during the fusing of the doped starting material and during the ~100 hour controlled cooling experiment. To accomplish this, a multi-step flow line was constructed with an activated charcoal trap to remove radon from the air exiting the furnace. Several other reservoirs were positioned before the radon trap to remove other daughter nuclides and any water or carbon dioxide from the flow stream that might reduce radon adsorption efficiency of the activated charcoal.

4.3.2 Activated Charcoal Selection and Preparation

The radon trap consisted of 3 mm diameter pellets of extruded activated carbon from NORIT Americas (product R-2030). Previous work comparing radon adsorption onto various activated charcoal brands showed that NORIT activated carbon performed best (Bocanegra and Hopke, 1988) among the products considered. A separate study

comparing six active carbons from Kuraray Chemicals reported the best adsorption performance by a carbon (referred to as “KAC-3”) with an apparent density of 0.40 g/ml and specific surface area (N_2 BET) of 910 m^2/g (Nakayama et al., 1994). The physical properties of the NORIT R-2030 activated carbon used here with apparent density of 0.56 g/ml and 800 m^2/g surface area are more like those of the most absorbent Kuraray carbon than any other investigated by Nakayama and coworkers.

To enhance adsorption performance, several studies recommend heat treating activated carbon under vacuum prior to use to remove water (Johnson et al., 1998; Momyer, 1960; Nakayama et al., 1994). This step was clearly necessary, as water condensation was observed along the interior regions below the two glass stoppers of the glass apparatus when fresh carbon pellets directly from the NORIT container were heated while the apparatus was sealed off from the vacuum line. The activated charcoal glass reservoir was heated to >150 °C by wrapping the reservoir exterior with flexible electric heating tape and then placed under vacuum sustained by a roughing pump. The charcoal was heated under vacuum for a minimum of thirty minutes and then the chamber was sealed to keep the charcoal isolated from ambient atmospheric conditions until the experiment commenced shortly thereafter. For added insurance that material would not be sucked into the pump, a series of glass tube loops in a water–ice bath served to trap any particles or unwanted gases before they entered the pumping system (Figure 4.2).

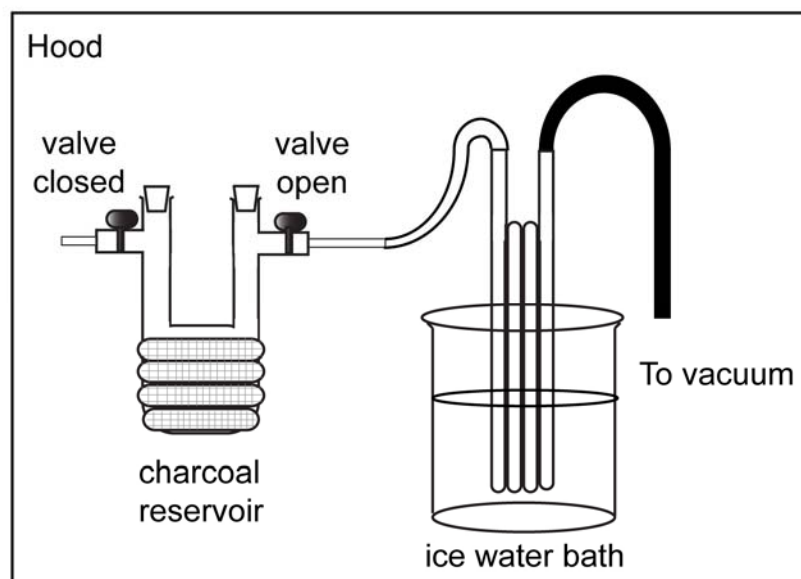


Figure 4.2. Flow line configuration for activated charcoal heating pre-treatment under vacuum prior to sample runs in furnace.

4.3.3 Flow Line Design

Gas flowing through the system consisted of Air Liquide Alphagaz1, an airlike synthetic nitrogen-oxygen mixture with 20 %–22 % O₂, <3 ppm H₂O, <1 ppm CO₂, and <2 ppm total hydrocarbons. Typical flow rate was approximately 75 cm³/min. The gas entered the top of the furnace and exited the bottom, step (1) of Figure 4.3, after which it bubbled through a glass dispersion tube with a coarse (170-220 μm pore size) frit into 5 M HNO₃ solution (2) intended to remove any airborne lead, bismuth, or polonium daughter products produced from the charge (Bagnall, 1957). The gas then bubbled through a second frit into a saturated NaOH solution to remove CO₂ from the gas stream (3).

Passing through two liquid reservoirs added moisture to the gas, so two aspirator bottles of CaSO_4 (indicator Drierite) were constructed next to remove any H_2O from the gas flow, steps (4) and (5). As a final insurance step to remove any remaining CO_2 , the gas proceeded through a second CO_2 -removal step (6) consisting of an aspirator bottle filled with DeCarbite, a granular silica base coated with NaOH to provide a large surface area for CO_2 absorption. To keep the DeCarbite grains from sticking together, the product was interspersed with vermiculite as recommended by the manufacturer. The gas then flowed into the activated carbon chamber (7), which contained approximately 100 g of activated charcoal, in a water-ice bath contained by a 1.9 L capacity dewar flask.

Radon has a boiling temperature of $-61.7\text{ }^\circ\text{C}$ (CRC, 1993-1994), so preliminary tests of the flow line included a dry ice–ethanol bath ($-97\text{ }^\circ\text{C}$). Trial runs with the dry ice–ethanol bath demonstrated that the activated charcoal chamber was efficiently trapping a relatively large volume of an unknown gas that might compete with radon for pore space within the charcoal pellets. Alphagaz1 is synthesized by mixing pure O_2 and N_2 gases rather than by directly purifying and compressing ambient air, but the Ar contents of Alphagaz1 are not routinely measured or reported in product literature so it remains a possible candidate. To mitigate this potential competition, a water-ice bath was chosen instead under the assumption that the $0\text{ }^\circ\text{C}$ conditions still would be sufficiently cold to trap the relatively heavy radon gas within the chamber but not other more abundant, but more volatile, gas species. To test the efficiency of the flow line in removing H_2O and protect the charcoal reservoir from any back-streaming air moisture, a third Drierite step (8) was added after the charcoal chamber.

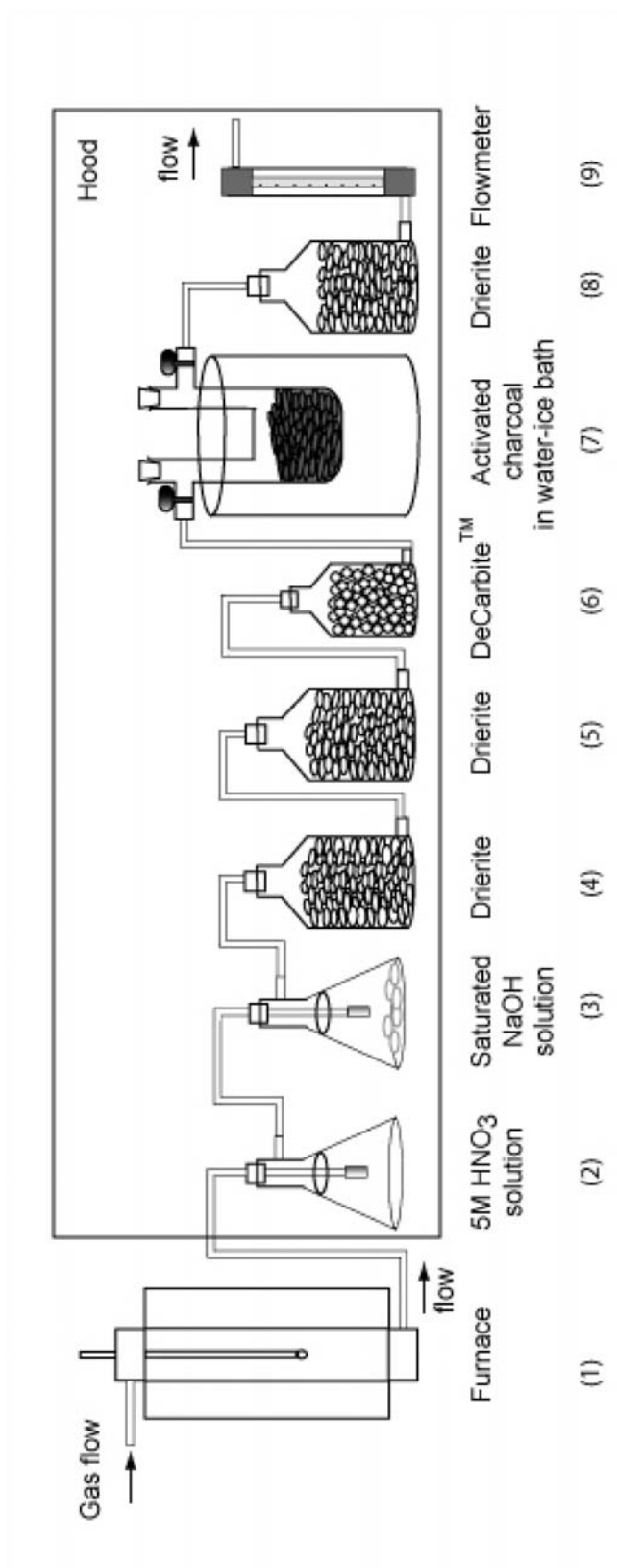


Figure 4.3. Flow line for ^{222}Rn removal from gas exiting furnace during experiments.

This drierite reservoir showed no visual indication of water absorption over the course of the experiments. Gas then passed through a flow meter out into the back of the hood (9).

After the experiment, the charcoal reservoir was sealed on both ends by closing the valves, removed from the flow line, transferred to a large plastic bag, and placed in a -10°C freezer for five months to ensure that nearly all of the trapped radon atoms would have decayed to non-gaseous daughter products. The charcoal was then removed from the freezer.

4.4 POST-EXPERIMENT FURNACE ANALYSIS

4.4.1 Activity Measurements of Sample Rod

Efforts to minimize system contamination assumed that ^{222}Rn gas would be flushed through the system by gas flow and collected in the charcoal cold trap, whereas ^{226}Ra volatilization would be negligible. Detailed, direct studies of radium volatility do not exist, though it is qualitatively described as being somewhat more volatile than barium (Bagnall, 1957; Bouissieres, 1958). To assess the extent and nature of possible contamination of furnace elements with Ra volatilized from the experimental charge, the ~ 47 cm alumina hanging rod was cut after the experiment into ten sections according to levels of activity measured by Geiger counter. To ensure that only ^{226}Ra would be producing any measured activity, this was performed three months after the experimental work. Sectioning occurred in a hood glove box of the Caltech Isotope Lab using a Dremel diamond wheel. The two ~ 13 cm ends of the alumina rod registered no discernable activity above background levels and were not subdivided. Activity was

concentrated in the middle 20 cm of the rod, which was sectioned into eight lengths. Rod sections were contained in reclosable low density polyethylene bags with wall thickness of 0.1 mm, and activity of each segment was measured using a Geiger counter and by γ -spectrometry.

Each bagged segment was placed on a surface 2.5 cm below a Ludlum in-window gas detector Geiger counter with the counter reading reported as an eyeball estimate of the range of counts detected while watching the counter for approximately a minute. Results are reported in Figure 4.4(d) and indicate that detected activity varies with position of the alumina rod in the furnace according to the thermal gradient. Activity rises above background levels between 700 °C and 800 °C, and Geiger counter readings suggest it peaks around 500 °C before decreasing to background levels at the top of the furnace.

The alumina rod had been used previously in C/CO buffered experiments, during which amounts of carbon were deposited on the rod that were qualitatively similar to the activity variations measured. This heterogeneous carbon surface may have also influenced ^{226}Ra deposition if the radium preferentially adsorbed onto carbon relative to alumina.

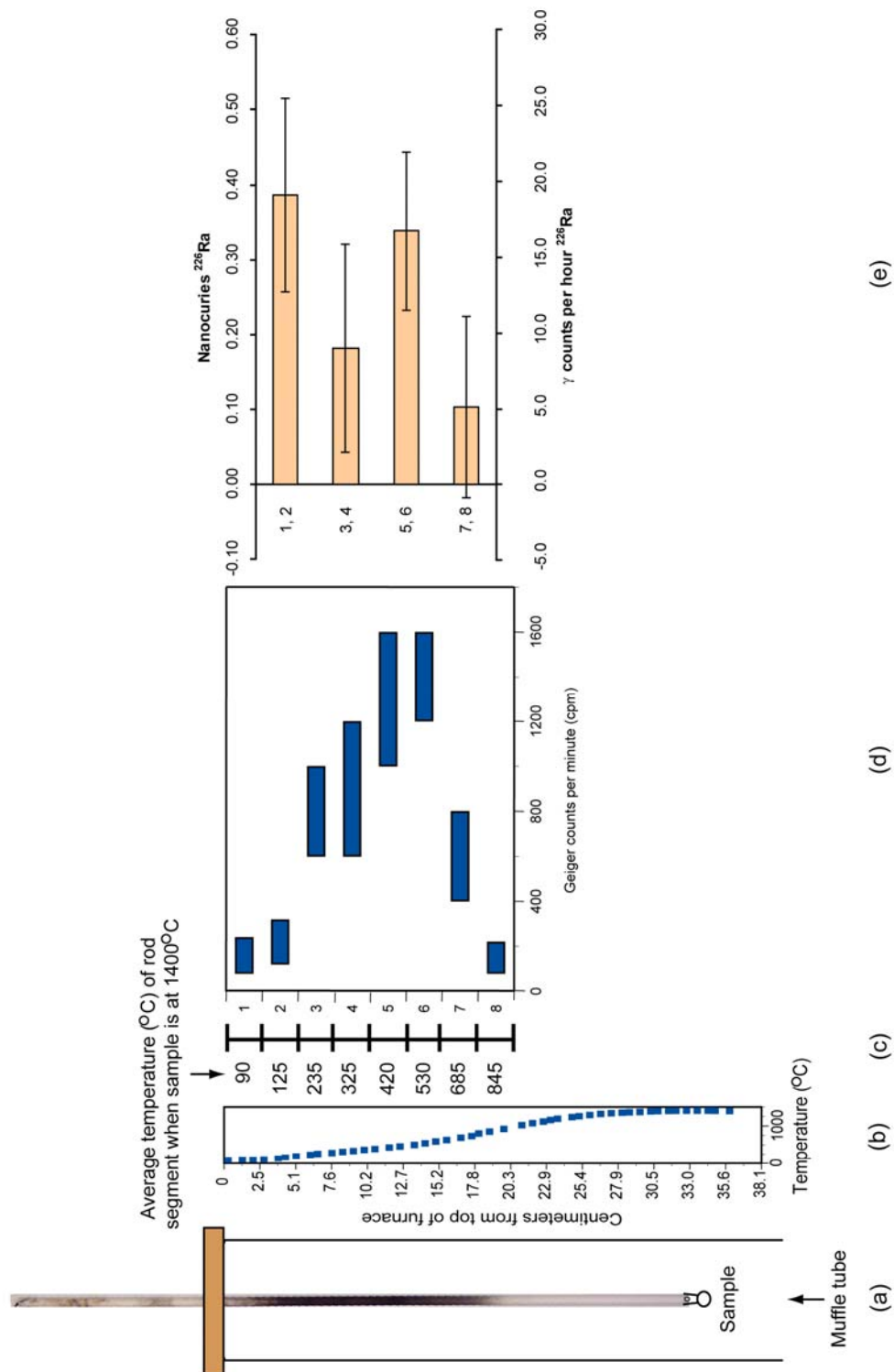


Figure 4.4. (a) Image of rod relative to muffle tube and sample in furnace, (b) thermal profile of furnace when sample location = 1400 °C, (c) average temperature of middle of each sectioned rod segment when sample is at 1400 °C, (d) rod segment activity measured by Geiger counter (counts per minute), (e) nCi ^{226}Ra and corresponding particle counts detected by γ -spectrometry for each pair of rod segments.

Geiger counters can only detect the intensity of ionizing radiation, not species identity, so γ spectra were collected to determine the activity source. The activity source concentrations on each rod segment were near detection limits of the spectrometer, so segments were paired and the four groups were each measured for 24 hours and their spectra compared to that of a 1.57 μCi ^{226}Ra standard and a 24 hour background spectrum. Each was positioned 10 cm from the detector, with the goal of being close enough to ensure detection yet not so close as to influence readings by the differing geometries of the rods and the source. Radium concentrations for each set of rod segment pairs is shown in Figure 4.4(e), with uncertainty calculated from the error associated with the background channel measurements immediately below and above the ^{226}Ra peak locations.

4.4.2 Radium Volatility

Although radium volatilization was anticipated to be essentially nonexistent, it occurred nonetheless. Assuming that the maximum activity recorded by Geiger counter represents 0.2 nCi of ^{226}Ra (from Figure 4.4(e)), application of an integrated rod deposition profile to the 4.75 cm diameter alumina muffle tube interior generates an estimated 8 nCi of total ^{226}Ra activity in the furnace after experimental work was complete. The furnace experienced two stages of potential ^{226}Ra exposure: the 3 hour fusing of the 2.5 μCi starting glass material and the 102 hour dynamic crystallization experiment CMAS2-1*-Ra with a sample activity of 0.5 μCi . Relative to the sample

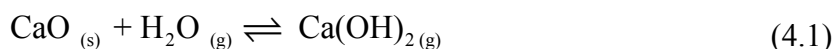
^{226}Ra contents, Geiger and γ -spectrometry measurements indicate that $\sim 1.5\%$ of the radium was lost over the course of the experiment.

Atomic mechanisms for radium volatilization from this CMAS composition are unknown. What radium left the sample did so at temperatures between $\sim 1320\text{ }^{\circ}\text{C}$ and $1440\text{ }^{\circ}\text{C}$ and condensed primarily in the $200\text{--}700\text{ }^{\circ}\text{C}$ range of the furnace. The furnace atmosphere was maintained with a very oxidizing gas flow containing $\sim 20\%$ O_2 , making it unlikely that radium would have been present as a monatomic species, though radium metal has a melting point of $700\text{ }^{\circ}\text{C}$, lower than that of any other alkaline earth nuclide except magnesium. No chemical data exists for RaO ; however, the boiling temperatures of other group II oxides of the periodic table systematically decrease from $\sim 3900\text{ }^{\circ}\text{C}$ to $\sim 2000\text{ }^{\circ}\text{C}$ with increasing atomic number (CRC, 1993-1994). Whether RaO volatilizes at temperatures at or below those of the experimental conditions remains undetermined and would not be necessarily expected, given that radium is thought to have a number of electrochemical properties very similar to barium (e.g., Pauling electronegativity, which is 0.9 vs. 0.89, respectively (Allred, 1961; Pauling, 1960)) and thus might be expected to behave similarly. Strontium, by comparison, is notably more electronegative at 0.95 (Allred, 1961), consistent with the flattening trend of most periodic properties approaching the bottom of each group.

Experimental studies of major element species volatility and condensation within the solar nebula have shown that, under reducing atmospheric conditions, Mg and Si can evaporate from condensed phases (Davis et al., 1999; Richter et al., 1999). Electron microprobe point transects from the edges inward of glass beads heated to $1400\text{ }^{\circ}\text{C}$ under

compressed air flow for 100 hours were analyzed, which verify that this evaporation did not occur under the oxidizing atmospheric conditions used for these studies.

Work on calcium by Hashimoto (1992) introduces another possibility for alkaline earth element volatilization: formation of gaseous $M(OH)_2$, where M represents an alkaline earth element. Experimental determination of the thermodynamic properties of hydroxide species involved in the reaction



allowed Hashimoto to calculate various Ca species stabilities for a variety of temperature, fO_2 , and $\log(H/O)$ conditions pertinent to models of the solar nebula. These conditions are admittedly quite different from that of our radium experiment furnace environment. The total gas pressure of the hydroxide experiments was a factor of 1000 lower than in the radium partitioning study here, and modeling in Hashimoto (1992) is restricted to $\log(H/O)$ above -2.8 , whereas the maximum 3 ppm H_2O content of the Alphasgaz1 used here would create a furnace $\log(H/O) = -4.8$. Also, the $\log(fO_2)$ of this radium work is very oxidizing, close to 0, whereas Hashimoto models the log of partial oxygen pressures from approximately -5 to below -40 . Nonetheless, the formation of gaseous alkaline earth hydroxides under the radium experiment conditions cannot be ruled out. At any given time, assuming constant rates of radium volatilization over the course of a controlled cooling experiment, the ratio of H_2O/Ra in the gas phase exceeds 10^7 , which is an ample supply of water molecules. Hashimoto also found that in a relatively oxygen-poor environment [$\log(H/O) = 3.16$] monatomic and oxide species were most abundant above $780^\circ C$, whereas at $\log(H/O) = 1.6$, $Ca(OH)_2$ was the dominant species up to $\sim 1530^\circ C$. These calculations suggest that $Ra(OH)_2$ could be considered a potentially stable

gaseous phase under the experimental conditions of our study, though no chemical data on this compound exist to support or eliminate this possibility.

While the gaseous species and volatility mechanism are uncertain, it remains a fact that activity measurements of the sectioned sample rod clearly indicate that a small but notable quantity of radium both volatilized and condensed within the furnace thermal gradient over the course of the experimental work. Future high-temperature experiments on Ra-bearing materials should be designed not only to capture Ra but also to ensure that all elements of the furnace that sit above ~ 200 °C in the thermal gradient are treated as radioactive byproducts.

Chapter 5: Experimental Study of Radium Partitioning between Anorthite and Melt at 1 atm

5.1 INTRODUCTION

Short-lived radioactive isotopes provide unique information about timescales of melting and magma transport processes that operate in the earth's crust and mantle. Any differentiation process that chemically fractionates parent and daughter elements from a decay chain will produce secular disequilibrium in which the activity ratio of the parent and daughter isotopes differs from unity. After approximately five half-lives of the daughter isotope, secular disequilibrium can no longer be measured and the decay rates of the parent and daughter are again equal. Because the half-life of ^{226}Ra is ~ 1600 years, $(^{226}\text{Ra})/(^{230}\text{Th})$ disequilibria produced within the past 8000 years may be preserved, making it an important chronometer of recent magmatic activity.

Successful interpretation of ^{226}Ra disequilibria in igneous rocks relies on our understanding of its partitioning behavior between minerals and melts. Unfortunately, no stable isotopes of radium exist with which to easily determine such partitioning. Because of the technical challenges involved in conducting experimental partitioning studies with Ra concentrations high enough to be measured *in situ*, our knowledge of Ra partitioning has been restricted to phenocryst/glass analyses of natural rocks producing apparent D_{Ra} values (Cooper et al., 2001) and modeling that either assumes Ra partition coefficients to be comparable to those of barium (e.g., Reagan et al., 1992; Schaefer et al., 1993; Volpe

and Hammond, 1991) or employs lattice strain theory and partition coefficients of other divalent elements to approximate D_{Ra} (Blundy and Wood, 1994; 2003a)

Partitioning behavior of radium between feldspars and coexisting melts is of particular importance because the large M site of the feldspar structure is one of the few sites in common crustal minerals able to accommodate measurable amounts of Ra, which has an ionic radius of 1.48 Å in VIII-fold coordination (Shannon, 1976). The presence of feldspar potentially can influence ($^{226}\text{Ra}/^{230}\text{Th}$) disequilibria in magmas generated at pressures below ~1.5 GPa within the plagioclase lherzolite stability field of the upper mantle (Presnall et al., 2002), whether the disequilibria arise from source melting or from diffusive reaction of rising melts with gabbroic cumulates (Saal and Van Orman, 2004; Van Orman et al., 2006). Dufek and Cooper (2005) demonstrate how lower crustal amphibolite dehydration melting involving plagioclase can generate and sustain radium excesses in arc magmas by incongruent continuous melting. Crystallization of feldspars within magma chambers in the shallow crust will further affect ^{226}Ra disequilibria by preferentially removing radium from melts and either reducing the magnitude of ^{226}Ra excess relative to ^{230}Th or even developing a ^{226}Ra deficit (e.g., Condomines et al., 1995; Zellmer et al., 2000).

5.2. EXPERIMENTAL METHODS

The starting composition was mixed from reagent oxides and CaCO_3 and ground under ethanol in an alumina mortar for five hours. The mixture was heated in air in 200 °C/hour steps and held at 1000 °C for 24 hours before fusing in a Pt crucible at 1450 °C.

The fused glass was reground under ethanol for one hour. A 0.5 gram aliquot was spiked with Ba and Sr solutions to achieve concentrations of approximately 100 ppm each. The material was dried, refused, and ground again under ethanol for half an hour. A fused glass of this starting composition (sample 2-1*-GL) was analyzed for major element content by electron microprobe and for Sr and Ba by SIMS. Additionally, a bead of this material, also not spiked with Ra, was run through the same experimental crystallization protocol described below, as a blank (sample 2-1*-1).

In a glove box positioned within a fume hood, approximately 2.5 μCi of ^{226}Ra in 5M HNO_3 solution was added to 150 mg of the Ba- and Sr-spiked starting material on a Teflon watch glass. The mixture was dried under a heat lamp, formed into a bead with polyvinyl alcohol (PVA), and transferred onto a wire mesh platform ~ 1 cm in diameter. The bead was air dried overnight and then placed near the top of a 1 atm Deltech vertical muffle furnace at ~ 170 $^\circ\text{C}$ for four hours to ensure dryness. It was then fused for 1 hour at 1430 $^\circ\text{C}$ and air quenched. The glass bead material was removed from the platinum wire mesh in the glove box using a percussion mortar and tweezers. The separated glass was powdered in an agate ball mill to produce the radium-spiked starting material.

The sample charge was prepared by mixing ~ 30 mg of spiked starting material with a drop of PVA and adhering it to a Pt wire loop. The small bead was dried overnight at ambient temperature and transferred to the furnace, where it was subjected to a known anorthite crystallizing thermal regime based on the procedures of Simon et al. (1994), as described in Miller et al. (2006). Since the liquidus temperature of this starting composition was approximately 1398 $^\circ\text{C}$ (all temperatures ± 5 $^\circ\text{C}$), the furnace was initially held at 1410 $^\circ\text{C}$ for 1 hour to reduce potential crystal nuclei before decreasing the

temperature at 2 °C/hour to 1370 °C, where the charge was held for 24 hours. The temperature was then decreased further at 2 °C/hour until the furnace reached the final temperature of 1330 °C and held there for 24 hours. The sample was air quenched by removing it from the top of the muffle tube. The charge was mounted in Araldite epoxy and polished to 0.3 μm fineness with alumina lapping paper before coating with carbon.

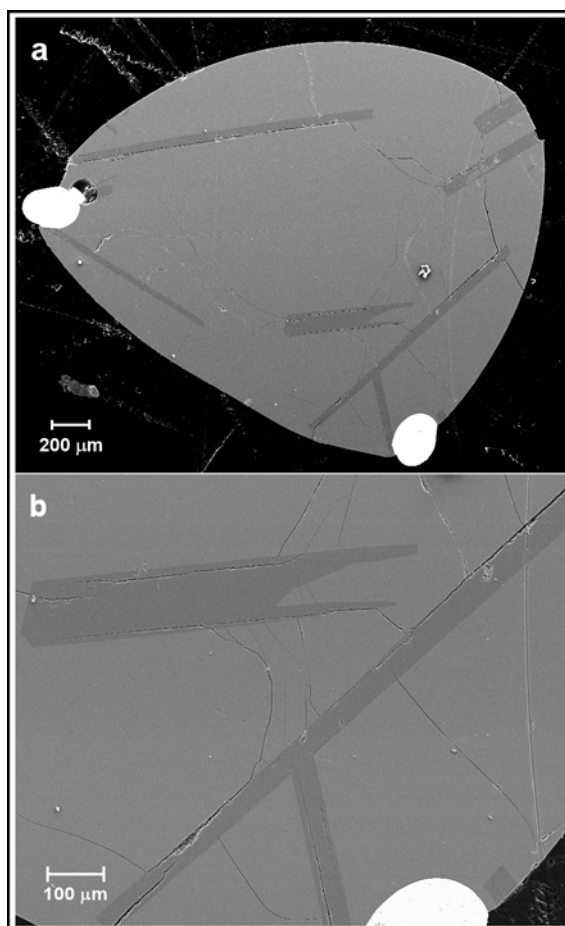


Figure 5.1. Back-scattered electron image of radium-bearing dynamic crystallization experiment 2-1*-Ra.

A standard (sample 2b-1-2) containing anorthite and glass of identical major element composition without radium but with elevated Ba (3000 ppm) and Sr (1000 ppm)

was both quenched directly from above the liquidus to check bulk composition and also crystallized under similar experimental conditions as the radium sample and analyzed by electron microprobe at Caltech (Miller et al., 2006). All trace element concentrations herein are expressed as oxide mole fraction (e.g. 1 ppm Ba means 1 mole BaO for every 10^6 moles of all oxide components).

5.3 SAMPLE ANALYSIS

The sample was analyzed on the modified Cameca ims-3f ion microprobe at Lawrence Livermore National Laboratory. The concentrations of ^{42}Ca , ^{88}Sr , ^{138}Ba , and ^{226}Ra were measured using a 30 μm diameter, 5 nA O^- primary beam with an impact energy of ~ 17 keV. Isobaric molecular interferences were minimized using energy filtering (Zinner and Crozaz, 1986); only secondary ions with kinetic energies within a 32.5 eV window centered on a 60 eV offset from the peak of the secondary ion energy distribution were focused into the mass spectrometer. Data collection consisted of 20 cycles through the mass sequence at each spot of interest, with integration times of 1 second for ^{42}Ca , ^{88}Sr and ^{138}Ba and 10 seconds for ^{226}Ra . Scans over the mass interval from 220 to 233 for both NBS-610 glass and the Ra-free anorthite/melt samples revealed virtually no background (0.2 counts/s) at mass 226. Figure 5.2(a) shows the portion of the mass spectrum from masses 224 to 228 on glass in the radium-free sample 2-1*-1 at 2 nA beam intensity; Figure 5.2(b) shows the same mass region for a radium-bearing glass sample (2-1*-Ra) at identical beam conditions. Mass scans were restricted to ± 0.15 amu centered at each integer mass. Radium is clearly detected at mass 226 with average

background intensity accounting for ~1 % of the Ra peak intensity in the glass over the 226 mass range shown in Figure 5.2.

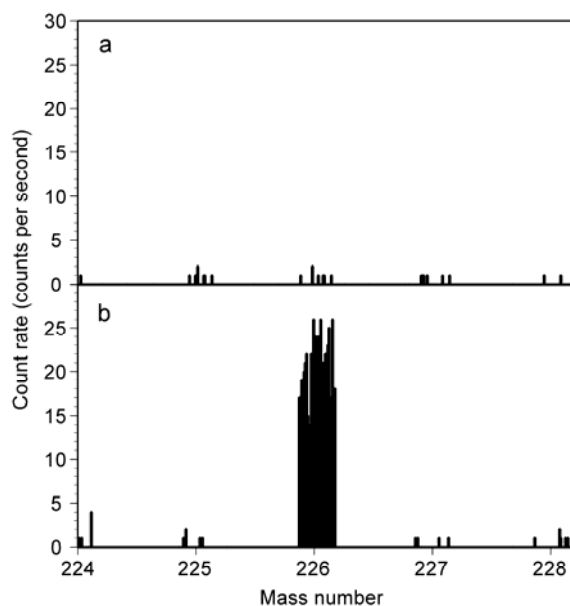


Figure 5.2. Ion probe mass scan over region surrounding mass 226 for glass of (a) radium-free and (b) radium-bearing samples. Data shown for each integer was taken from -0.15 to $+0.15$ of each mass center with counts measured at each hundredth of a mass unit. Count rate is reported in counts per second.

Concentrations (C_i , ppm) were calculated by applying a calibration factor, F , to convert secondary ion intensities to ppm abundances. For Sr and Ba, these calibration factors were obtained from electron probe analysis of the standard anorthite- and glass-containing sample 2b-1-2, which was spiked with 3000 ppm Ba and 1000 ppm Sr. F values for the glass ($^{88}\text{Sr} = 2900 \pm 100$, $^{138}\text{Ba} = 3300 \pm 200$) and anorthite ($^{88}\text{Sr} = 2000 \pm 100$, $^{138}\text{Ba} = 2300 \pm 400$) were calculated from ^{42}Ca -normalized ion intensities. Since no appropriate standard was available for Ra, ^{226}Ra ion intensities were converted to ppm abundances using the upper bound on the F -value for Ba. $C_{i,\text{std}}$ represents the

concentration (ppm) of ion i in a standard and I_i is ion intensity (counts/s) in the material with unknown concentration of i :

$$F = (C_{i, \text{std}}) \left(\frac{I_{\text{Ca}}}{I_i} \right)_{\text{std}}. \quad (5.1)$$

Concentrations in the samples were determined according to the equation,

$$C_i = F \left(\frac{I_i}{I_{\text{Ca}}} \right) \left(\frac{\text{CaO}_i}{\text{CaO}_{\text{std}}} \right), \quad (2)$$

where I_i represents the ion intensity for the element of interest in the sample, I_{Ca} is the ^{42}Ca ion intensity, CaO_i is the known CaO concentration in the sample, and CaO_{std} is the CaO concentration in the standard from which the calibration factor was established. In this case CaO_i and CaO_{std} have identical values. Following Brennan et al. (1995), the detection limit calculated for radium at mass 226 is 2 ppb for both anorthite and glass.

5.4 RESULTS AND DISCUSSION

The sample charge consisted of CMAS glass and well-formed pure anorthite laths, the largest measuring over 100 μm along its short dimension. Since the spatial resolution of our analyses is limited by the ~ 30 μm diameter of the ion probe primary beam, measurements were taken in the centers of crystals and assumed to represent near-liquidus growth at 1400 $^\circ\text{C}$. Table 5.1 reports molar partition coefficients for Ca, Sr, and Ba, calculated from crystal center and glass starting compositions, with uncertainties propagated from both crystal and glass analyses. Initial melt compositions used to calculate D^{Mg} and D^{Ra} (that is, mole fraction of the oxide of interest in anorthite divided by mole fraction of the oxide in the melt) were obtained by back-correcting final

melt composition to account for 23 % crystallization. Total fraction crystallized was calculated using the Rayleigh equation and Ba data. The determined molar partition coefficient for Ra is 0.040 ± 0.006 .

5.4.1 Lattice Strain Modeling with D_{Ra}

The most commonly used partitioning model describing the empirical observation of a quasi-parabolic relationship between log of isovalent cation partition coefficients and ionic radii of those cations (Onuma et al., 1968) is that of Blundy and Wood (1994):

$$D_i(P, T, X) = D_o(P, T, X) \exp \left[-4\pi E N_A \left[\frac{r_o}{2} (r_i - r_o)^2 + \frac{1}{3} (r_i - r_o)^3 \right] / RT \right]. \quad (3)$$

Here the partition coefficient D_i for a given absolute temperature (T), pressure (P), and phase compositions (X) is a function of the ideally sized radius (r_o) of a fictive cation with partition coefficient (D_o) that would fit into the crystallographic site without strain, the radius of the cation of interest (r_i), and a strain parameter qualitatively related to the Young's Modulus of the site (E). N_A is Avogadro's number and R is the gas constant.

The addition of radium partitioning data to a plagioclase Onuma curve for divalent cations provides a unique opportunity to test the application of lattice strain modeling to prediction of large, geologically short-lived radioactive isotope partitioning. The best-fit lattice strain model parameters for these data, when fitted in natural log space at 1400 °C, are $D_o = 0.93(5)$, $r_o = 1.207(6)$ Å, and $E = 107(9)$ GPa. Parameterizing with only the Ca, Sr, and Ba partition coefficients of this study (that is, excluding the Ra data) results in a 5 % decrease in E with negligible changes for D_o and r_o . These r_o and E

values fall within or close to the reported uncertainty of the extrapolated endmember anorthite parameters in Blundy and Wood (1994), although those authors considered all magnesium to reside in the plagioclase M site for their parameterizations.

Magnesium has been shown to occupy both tetrahedral and octahedral sites in anorthite (Longhi et al., 1976; Peters et al., 1995) and its exact site distribution in this composition remains unknown. Therefore, magnesium data are not used in the Onuma curve parameterization here, though the bulk molar distribution coefficient is plotted in Figure 5.3. Using the lattice strain model to predict the partitioning of octahedrally coordinated Mg in anorthite results in an estimated octahedral site occupancy of 35 %, which differs from previous, significantly lower, estimates of 3 % and 9 % for this composition based on thermodynamic melt modeling (Miller et al., 2006).

5.4.2 Ra-Ba Fractionation

The extent to which barium partitioning can be used to estimate initial ^{226}Ra contents of magmas prior to crystallization in magma chambers, an important component of dating eruptions, remains unresolved. Although Ra-Ba fractionation is clearly predicted by lattice strain equilibrium partitioning models, some studies continue to find assumptions of identical geochemical behavior sufficient to recover initial $(^{226}\text{Ra})/\text{Ba}$ ratios of magmas (e.g., Condomines et al., 2005). We measure a $D_{\text{Ra}}/D_{\text{Ba}}$ of 0.23 ± 0.05 for this composition, which compares favorably with estimates of 0.21–0.25 for plagioclase used by other workers (Cooper and Reid, 2003; Cooper et al., 2001). Greater $D_{\text{Ra}}/D_{\text{Ba}}$ fractionation, characterized by a tighter Onuma curve, results with increased Ca content in plagioclase and/or decreased temperature (Cooper et al., 2001). Although this

study was conducted at 1400 °C, strain modeling using the parameters reported here permits calculating Ra-Ba fractionation between highly calcic plagioclases and melt at the lower temperatures more common in natural environments.

5.4.3 Implications for Radium Partitioning in Clinopyroxene

($^{226}\text{Ra}/^{230}\text{Th}$) excesses in young volcanic rocks are ubiquitous across a wide range of geologic environments and range from slight in OIB settings to values of over 6 in some arc lavas (Turner et al., 2001). While fluid addition is also implicated in arc settings, such excesses are generally thought to result from Ra-Th fractionation during melting and to be preserved by rapid transport of the melt to the surface, although the exact location of radium excess production in even the relatively uncomplicated MOR setting remains an open question. A study of well characterized lavas from the East Pacific Rise (Sims et al., 2002) attributed the inverse ^{226}Ra and ^{230}Th excess systematics to polybaric melting of a homogenous source, with the ^{226}Ra excesses generated at shallower depths in equilibrium with depleted spinel harzburgite material just beneath the lower crust.

The dominant mantle reservoir of radium below the plagioclase peridotite field is likely clinopyroxene, except possibly in hydrous environments where phases such as phlogopite (calculated $D_{\text{Ra}} > 1$ for melts and $\gg 1$ for fluids) may play a significant role in radium storage at depth (Feineman and DePaolo, 2003). Given that Ra^{2+} has been shown here to be a well behaved ion whose partitioning behavior between plagioclase and melt is closely approximated by a lattice strain partitioning model (Blundy and Wood, 1994),

this study lends further confidence to clinopyroxene/melt D_{Ra} estimates, typically on the order of 10^{-7} (Cooper et al., 2003), calculated from such models.

Table 5.1. Compositions of starting material, standard, radium-free sample, and radium-bearing sample as determined by electron microprobe (EMP) and ion probe (SIMS) analysis. Elements not analyzed denoted by ‘-’. Abundances reported in wt. %. Na_2O , K_2O , FeO (total iron as FeO) were analyzed by EMP in standard sample 2b-1-2 and found to be 0.02 wt. % or less. Molar partition coefficients for divalent elements are reported for data collected from centers of crystals and random surrounding glass points back-corrected for fractional crystallization to initial melt composition. Standard deviation (1 σ) in the last one or two decimal places is given by the numbers in parentheses.

| | <u>EMP (wt. %)</u> | | | <u>SIMS (ppm)</u> | | | |
|-------------------------|------------------------------------|---|---------------------------------------|------------------------------------|----------------------------------|-----------------------------|-------------------------|
| | Starting glass 2-1 n = 10 | Standard 2b-1-2 Anorthite n = 10 | Standard 2b-1-2 Glass n = 10 | Ra-free Run 2-1*-1 Anorthite | Ra-free Run 2-1*-1 Glass | Run 2-1*-Ra Anorthite | Run 2-1*-Ra Glass |
| SiO_2 | 46.6 (2) | 43.4 (1) | 47.97 (11) | - | - | - | - |
| Al_2O_3 | 21.56 (6) | 36.5 (2) | 18.14 (19) | - | - | - | - |
| MgO | 0.99 (1) | 0.099 (4) | 1.19 (6) | - | - | - | - |
| CaO | 30.26 (7) | 20.9 (1) | 32.48 (18) | - | - | - | - |
| SrO | 114 (4) ^a | 0.111(5) | 0.136 (5) | 99 (5) | 111 (4) | 96 (5) | 112 (4) |
| BaO | 68 (4) ^a | 0.097 (8) | 0.60 (3) | 10 (2) | 76 (4) | 12 (2) | 85 (5) |
| RaO | nd | - | - | nd | nd | 0.16 (3) | 5.2 (3) |
| | <u>$D^m\text{Mg}^b$</u> | <u>$D^m\text{Ca}$</u> | <u>$D^m\text{Sr}$</u> | <u>$D^m\text{Ba}$</u> | <u>$D^m\text{Ra}$</u> | | |
| 2-1*-Ra | 0.098 (6) | 0.724 (4) | 0.84 (6) | 0.17 (3) | 0.040 (6) | | |

nd = not detected

^aDoping concentrations (ppm) as measured by SIMS on quenched glass of starting material.

^bBulk Mg partition coefficient shown from standard run 2b-1-2, including all magnesium in anorthite irrespective of crystal coordination environment.

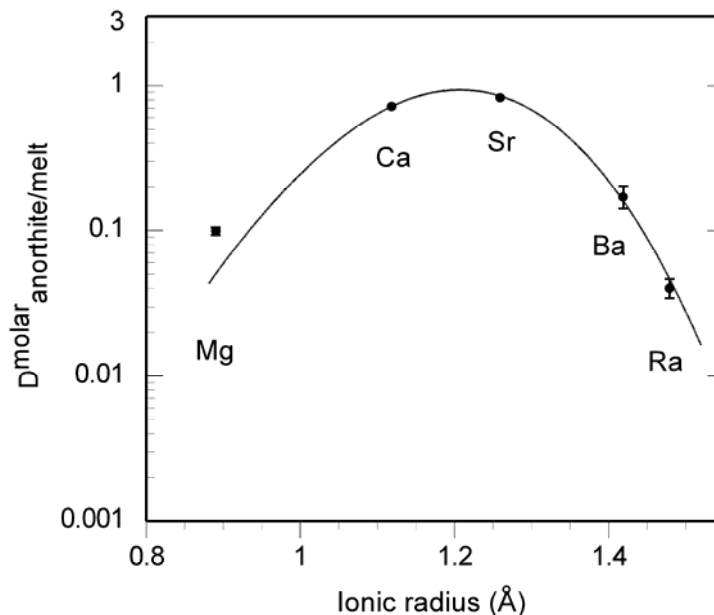


Figure 5.3. Onuma curve generated by lattice strain modeling of Ca, Sr, Ba, and Ra molar partition coefficients. Ionic radii are for VIII-fold coordination taken from Shannon (1976). Uncertainty reported as 1σ and within the size of the markers except where explicitly shown.

5.5 CONCLUSIONS

For the first time, experimental radium partitioning data are available to test a widely used predictive partitioning model (Blundy and Wood, 1994). Hitherto, Ra partitioning behavior has been estimated or calculated rather than directly measured. When focus is restricted to divalent elements known enter only the VII-fold site in anorthite (Ca, Sr, Ba, Ra), we find excellent agreement of the measured radium partition coefficients with those predicted by lattice strain models. Our results show that partitioning studies for phases in which Ra is more compatible, such as potassium feldspars and phlogopite (Blundy and Wood, 2003a), could be relatively straightforward. Furthermore, our present experiments have sufficient analytical margins that obtaining

Ra partition coefficients at least one and possibly two orders of magnitude lower would be feasible.

Chapter 6: Future Work

A logical next step in extending this work might be assessing its performance modeling natural liquids using a thermodynamic melt activity model such as MELTS (Ghiorso and Sack, 1995) at 1 atm, where the most literature partitioning data are available and the MELTS model is best constrained. However, continued progress towards a universal model of partitioning that incorporates lattice strain treatment for crystal chemistry depends on addressing several key issues.

(1) Clarifying the physical meaning of lattice strain parameters. As discussed in chapter 2, the parameters r_o (site ideal ionic radius) and E (effective Young's modulus of the site) were originally postulated to be purely crystal chemical properties (Blundy and Wood, 1994; Brice, 1975). More recent work has suggested an apparent additional dependence of these parameters on melt chemistry (e.g., Blundy and Dalton, 2000; Prowatke and Klemme, 2005; van Westrenen et al., 2000), a potentially considerable complication that could preclude use of the lattice strain formalism as a simple representation of mineral structure controls on partitioning. While parameterizations in chapter 2 demonstrate that the anorthite-CMAS melt partitioning data presented in this work can be modeled with r_o and E remaining solely crystal chemical parameters, systematic investigations into the nature of these parameters in other systems are necessary to fully appreciate their physical significance and determine their role in constructing more universal partitioning models.

(2) A tricky challenge to full thermodynamic descriptions of trace element chemistry in both solid and liquid phases lies in the paucity of thermodynamic data for endmembers at the trace element-rich end of mineral solid solutions series and for trace element bearing melt species, the identities and abundances of which may be unknown (Hess, 1995). Existing high quality melt thermodynamic models for natural (such as MELTS (Ghiorso and Sack, 1995) and its subsequent variations) and simple systems (Berman, 1983; Berman and Brown, 1984) only address the mixing behaviors of major and minor element constituents, leaving the behavior of many trace species uncharacterized. Our results demonstrate how the partitioning model presented in chapter 2 may be applied to obtain measurements of melt trace constituent activity coefficients in carefully designed experiments. However, calculating D values from this model in other systems requires independent knowledge of trace element energetics. This lack of thermodynamic data on trace species remains a hurdle to using the partitioning model presented in chapter 2 to predicting trace element D values in systems where activity coefficients are unknown. Poor accuracy of some major species activity coefficients is a problem in some parts of melt composition space, as well.

(3) Due to relative experimental ease, the data set for partitioning behavior at 1 atm is large compared to that at higher pressures. Silicate melts are over an order of magnitude more compressible than silicate minerals (Lange and Carmichael, 1990), but discerning how this influences partitioning requires separating the effects of pressure, temperature, and melt composition. The hazards of failing to explicitly account for pressure effects in some cases may be mitigated by the fact that temperature and pressure, which both

increase with depth below the Earth's surface, often have opposite effects on partitioning. Nonetheless, pressure effects have been identified (e.g., Bedard, 2006; Blundy and Wood, 2003b; Colson and Gust, 1989; Fujinawa and Green, 1997) and adjustments to existing simple partitioning models have been proposed, such as in the case of plagioclase (Vander Auwera et al., 2000). Oxygen fugacity is another intensive variable not addressed by models that consider only homovalent substitutions but could be incorporated into a broader treatment of partitioning using the Wood and Blundy (2001) expressions for D dependence on cation valence state.

(4) As the multiple site occupancy of Mg^{2+} in anorthite (chapter 2) demonstrates, further development and calibration of partitioning models based on crystal lattice strain theory will require careful consideration of cation site occupancy. Fitting model expressions to partitioning data ideally constrains the shape of the Onuma curve (Onuma et al., 1968) with cation radii both larger and smaller than the ideal site size, and should be based on more data points than the number of variables being parameterized. In the cases of minerals where a limited number of isovalent cations may substitute onto a given site, quantifying the population of a cation that predominately prefers a different site, yet still is present in low abundance, can increase the data set available for modeling partitioning on the site of interest. Likewise, correct identification of substituting cation valence state is an important consideration when calibrating lattice strain models to experimental partitioning data sets. Advances in spectroscopic methods such as EXAFS (Extended X-ray Absorption Fine Structure) and XANES (X-Ray Absorption Near Edge

Structure) may offer new information about such cation behavior within both crystalline and amorphous phases that will improve partitioning model precision.

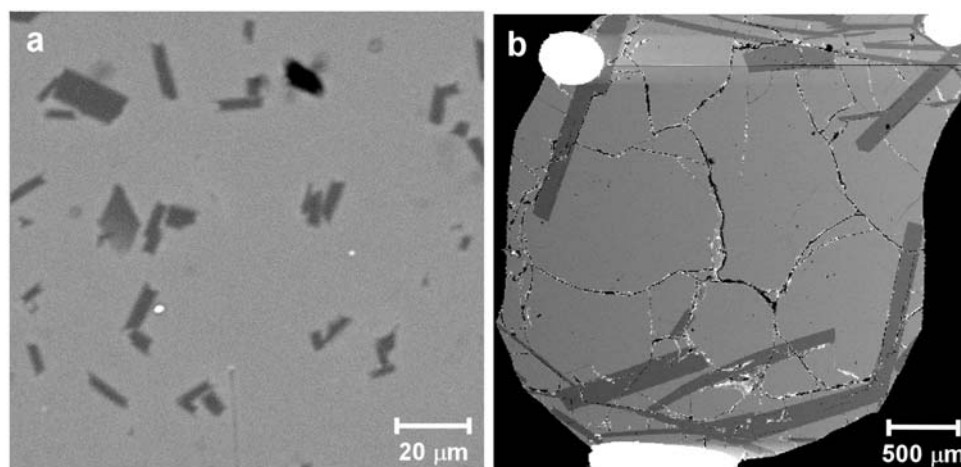
Appendix 1

A1 EXPERIMENTAL DESIGN

A1.1 Constant Temperature vs. Dynamic Crystallization Experiments

The rationale for choosing to analyze controlled cooling instead of isothermal experimental charges to measure anorthite-melt divalent element partition coefficients has been discussed in chapter 2. The difference in crystal size produced by these two thermal regimes is illustrated by back-scattered electron (BSE) imaging in Figure A1.1, which shows that the short dimensions of anorthite laths grown under isothermal conditions rarely exceed 10 μm (a). As the 400 nA beam of the Caltech JEOL 733 electron microprobe had a diameter of $\sim 12 \mu\text{m}$, all reconnaissance trace element analyses of these small crystals included a glass component. Image (b) of the same composition shows crystals grown by dynamic crystallization, which are analyzed easily both by electron microprobe and ion probe.

Figure A1.1. Comparison of anorthite crystals grown under (a) isothermal conditions (run 2-2-8), and (b) a dynamic crystallization thermal regime (run 2b-2-2).



A graphical representation of the controlled cooling program discussed in Section 2.2.4, based on that of Simon et al. (1994), is shown below in Figure A1.2, with furnace temperature plotted as a function of time.

Thermal history

(Adapted from Simon et al., 1994)

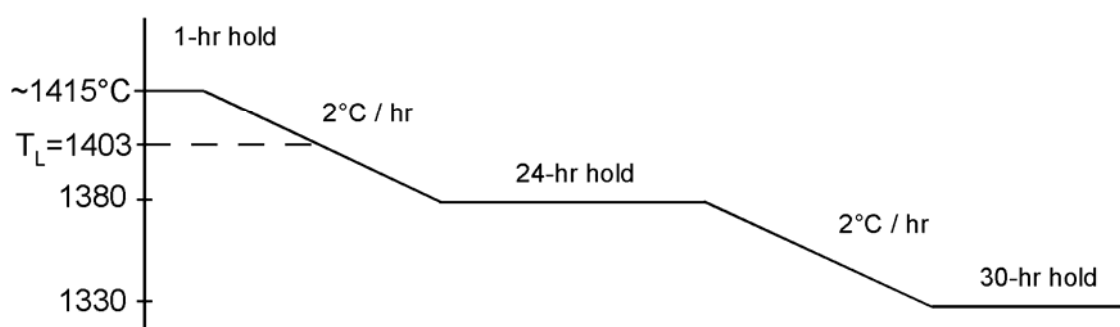


Figure A1.2. Controlled cooling path of dynamic crystallization experiments described in chapter 2.

A1.2 Comparison of Electron Probe and Ion Microprobe Analysis Data for CMAS2 Compositions

A1.2.1 CMAS2 Partitioning Data from Electron Microprobe Analysis of Crystal Centers

Several analytical methods, conditions, and starting material spike concentrations were considered when attempting to resolve the differences in barium, the most incompatible element of these studies, partitioning in the seven CMAS composition systems described in chapter 2. Anorthite crystal center points from compositions doped with 1500 ppm Ba were measured by electron microprobe analysis (EMP). Analytical

conditions were 25 nA and 15 keV, with 30 s on peak and 15 s background counting times and standards as listed in Section 2.2.4. Assuming that crystal centers represent anorthite that grew from the initial melt composition, partition coefficients were calculated using the compositions of fused glasses of the starting materials. While this may not be strictly true, it likely produces a better representation of partitioning near the anorthite liquidus than the apparent D value generated by crystal center/final melt data. The first column of Table A1.1 shows that the Ba partition coefficients calculated from these data have large uncertainties and are indistinguishable from one another.

The standard deviations given for the crystal center EMP D_{Ba} are essentially entirely due to the variability in the crystal EMP analyses. The higher Ba concentration, higher beam currents, and longer counting times for the rim EMP Ba data in Table A1.2.1 can explain the larger variability of the center EMP D_{Ba} . Nevertheless, the center EMP D_{Ba} values are systematically higher than the rim values for 6 of the 7 compositions. This is evidence for disequilibrium partitioning that reflects initial rapid crystal growth. The larger standard deviations for the center EMP Sr data are also explained by the differences in analytical conditions. Here, unlike Ba, there are no systematic differences between D_{Sr} values for the center and rim analyses of the different compositions, and the two data sets agree to within $\pm 15\%$. With a partition coefficient near 1, Sr is very insensitive to disequilibrium effects associated with liquid boundary layers; however, if disequilibrium were due to a greater importance of surface, as opposed to bulk, partitioning at initially high growth rates, then Sr might have been as likely to show disequilibrium effects as any other element. Our next analytical approach involved

measuring trace element compositions of anorthite interiors from these same samples by ion microprobe.

Table A1.1. Comparison of three CMAS2 anorthite/melt molar partition coefficient data sets generated by electron microprobe and ion microprobe analysis of spots in the centers of crystals doped with 1500 ppm Ba and electron microprobe analysis of anorthite crystal edges from starting material doped with 3000 ppm Ba. Not analyzed = na.

| Crystal Data Location | <u>Ba</u> | | | <u>Sr</u> | | | <u>Be</u> |
|-----------------------|-----------|----------|----------|-----------|----------|----------|-----------|
| | Center | Center | Rim | Center | Center | Rim | Center |
| Instrument | EMP | SIMS | EMP | EMP | SIMS | EMP | SIMS |
| Beam | 25 nA | 2 nA | 400 nA | 25 nA | 2 nA | 400 nA | 2 nA |
| Doping concentration | 1500 ppm | 1500 ppm | 3000 ppm | 1000 ppm | 1000 ppm | 1000 ppm | 500 ppm |
| 2-1 | 0.23 (28) | 0.20 (2) | 0.18 (2) | 0.78 (28) | 1.01 (2) | 0.90 (5) | 0.27 (2) |
| 2-2 | 0.21 (22) | 0.20 (2) | 0.15 (2) | 0.77 (24) | 1.03 (4) | 0.92 (4) | 0.22 (4) |
| 2-3 | 0.18 (21) | 0.20 (3) | 0.16 (1) | 0.90 (24) | 1.14 (6) | 0.97 (5) | 0.21 (2) |
| 2-4 | 0.33 (20) | 0.16 (2) | 0.18 (2) | 0.98 (26) | 1.13 (2) | 1.06 (5) | 0.153 (3) |
| 2-5 | 0.27 (22) | 0.23 (1) | 0.18 (1) | 1.29 (42) | 1.34 (3) | 1.16 (5) | 0.138 (7) |
| 2-6 | 0.26 (22) | 0.19 (2) | 0.18 (1) | 1.49 (52) | 1.37 (2) | 1.29 (4) | 0.13 (1) |
| 2-7 | 0.13 (14) | na | 0.21 (2) | 1.43 (40) | na | 1.45 (6) | na |

A1.2.2 CMAS2 Partitioning Data from Ion Microprobe Analysis of Crystal Centers

Anorthite and coexisting glass from the seven compositions of the CMAS2 series were analyzed with the Lawrence Livermore National Laboratory (LLNL) Cameca ims-3f ion microprobe (SIMS). The primary beam had 12.5 kV, 2 nA primary beam, a 4500 V secondary accelerating voltage, and a 60 V offset to minimize molecular ion interferences. Ion count rates were normalized to ^{40}Ca and converted to concentration factors determined from several glass standards. A CMAS+Ti glass from run 224SAM21 containing 1.65 +/- 0.13 wt. % Ba as determined on the Caltech 733 JEOL electron microprobe was used as a Ba standard and TI-G quartz diorite glass with 2.4 ppm Be served as a Be standard.

The concentration of a trace element measured by SIMS may be calculated from the following equation:

$$C_i (\text{ppm}) = F \left(\frac{I_i}{I_{^{40}\text{Ca}}} \right) \left(\frac{\text{CaO}_i}{\text{CaO}_{\text{std}}} \right). \quad (\text{A1})$$

F represents a calibration factor, I_i is the ion intensity of the trace element of interest (i) (counts/s), $I_{^{40}\text{Ca}}$ is the measured ion intensity for ^{40}Ca , CaO_i is the concentration of CaO in the sample material, and CaO_{std} is the CaO concentration in the standard for which the calibration factor was determined. The success of F accurately converting measured ion intensity of the trace element into concentration depends on how similar ^{40}Ca sputtering is to that of the trace element i .

The SIMS analyses generated more precise Ba and Sr data, but subsequent 400 nA analyses of points within and around several ion probe analysis pits, which were 30–50 μm in diameter, indicated nontrivial heterogeneity in the anorthite crystals that would not be spatially well resolved by ion probe. Since the electron microprobe has a more focused beam than the ion probe even at 400 nA, the trace element partitioning study of chapter 2 was conducted using starting materials doped with 3000 ppm Ba, 1000 ppm Sr. A 400 nA beam current was used to obtain trace element compositions at the rims of anorthite crystals and those edge regions were assumed to be near chemical equilibrium with the surrounding glass compositions. Further analytical and experimental details are given in Section 2.2.4.

Despite the above results, comparison of the overall SIMS D_{Ba} data with our adopted EMP rim analyses (Table A1.1) indicates acceptable agreement (everything within 30 %). Only composition 5 has a higher SIMS D_{Ba} than that from the rim EMP analyses by more than two standard deviations of the propagated standard deviations.

Five out of six compositions showed higher D_{Ba} using the SIMS data for crystal centers, which is consistent with some disequilibrium partitioning for the center data. However, unlike the EMP center-rim comparison above, there are likely systematic error differences between the SIMS and EMP data, so systematic offsets cannot be interpreted statistically. The effect of such systematic SIMS-EMP differences is illustrated by the D_{Sr} data in Table A1.1. With D_{Sr} approximately 1, all data are expected to be insensitive to disequilibrium partitioning effects. The D_{Sr} from SIMS are systematically higher than the rim EMP D_{Sr} by amounts ranging from 6 to 18 %. However, when regarding the measured standard deviations as uncertainties, the SIMS-EMP rim difference only exceeds 2σ for composition 5 (as for Ba).

A1.2.3 Be Partitioning

Plagioclase/melt partition coefficients for Be have been determined by Bindeman et al. (1998), who measured natural Be abundances of approximately 50–500 ppb by ion microprobe in 1 atm experimental charges from Drake and Weill (1975). Those partition coefficients (D^{molar}) range from 0.17 ± 0.07 for an intermediate plagioclase composition ($An_{44.8}$) at the lowest experimental temperature of 1153 °C to 0.56 ± 0.08 in the most anorthitic ($An_{77.2}$) composition and highest temperature (1297 °C) of the study. The least square approximation parameters for Be partitioning according to their equation,

$$RT \ln(D_i) = a \cdot X_{An} + b$$

are $a = 28.2 \pm 6.1$ and $b = -29.5 \pm 4.1$, in units of kJ. This predicts a Be partition coefficient of 0.90 for pure anorthite, well above the values measured in our study. Combined a and b parameter error yields a prediction uncertainty of ± 0.2 , but this fails to

reconcile the model with our measured partition coefficients at higher concentration levels. Caution is warranted because the systematic errors introduced in our data by the use of the quartz diorite glass TI-G as the SIMS standard are unknown.

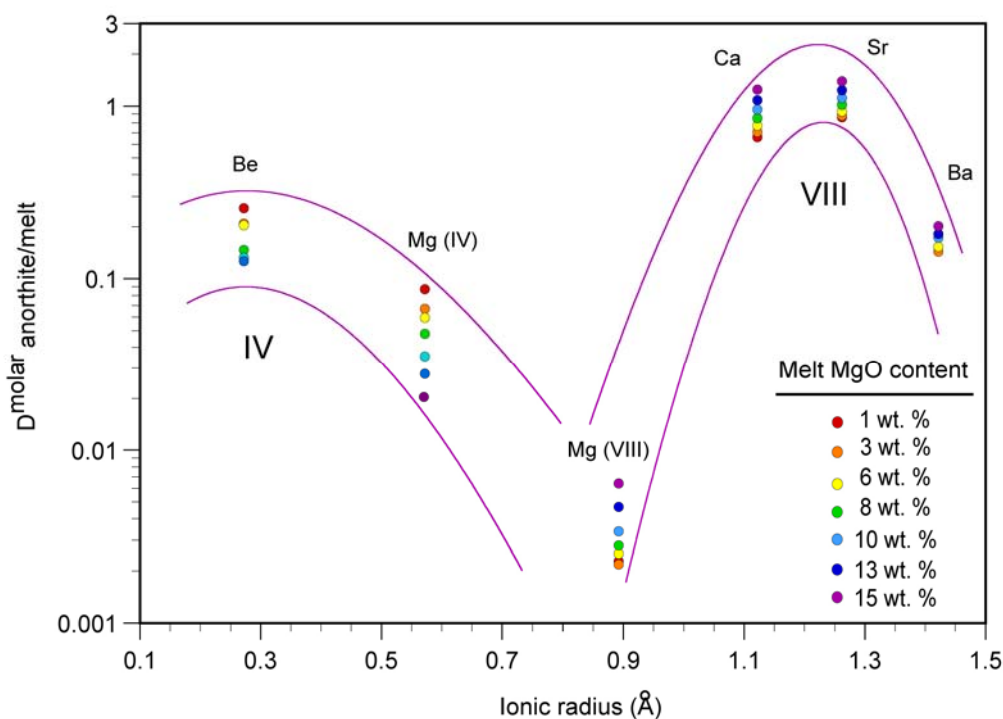


Figure A1.3. Anorthite/silicate melt divalent element partitioning of tetrahedral and cubic coordination site occupancy for CMAS2 compositions.

The Be partition coefficients measured in the compositions of this study show a systematic decrease from 0.27 in the least magnesian melt composition 2-1 (~1 wt. % MgO) to 0.13 in the 2-6 experimental charge, which contains an initial melt content of ~12 wt. % MgO. This trend mirrors that of the magnesium population calculated to partition onto the tetrahedral (IV-fold) site of the anorthite structure using equation (2.16) in Section 2.3.3, as may be expected since Be is tetrahedrally coordinated in plagioclases (Smith and Brown, 1988). Error bars are omitted for clarity in Figure A1.3, but 1 σ uncertainties for these partition coefficients are reported for bulk Mg in Table 2.3 of

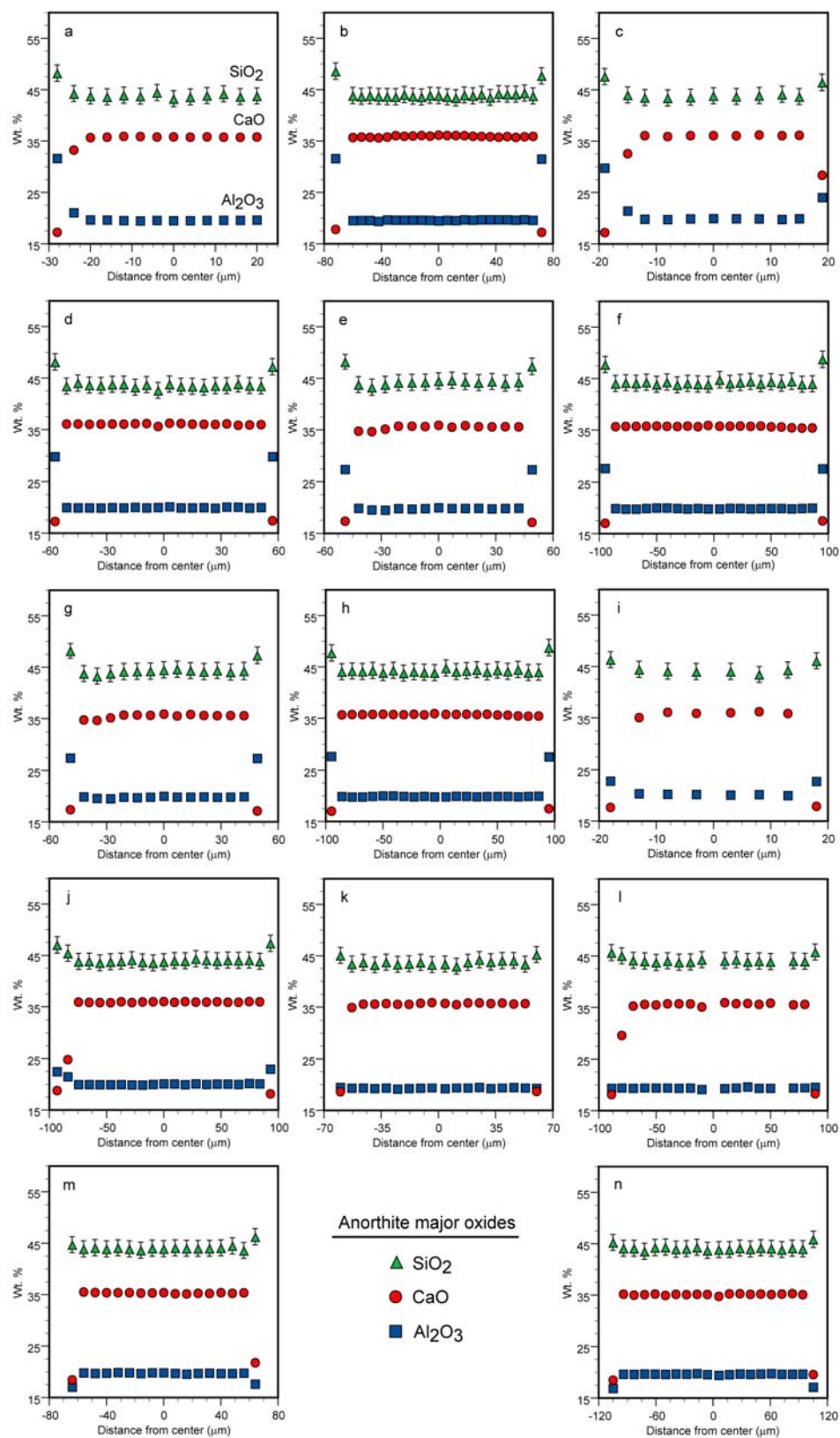
chapter 2 and the last column of Table A1.1 for Be. The split of Mg into both tetrahedrally and octahedrally coordinated sites within the anorthite crystal lattice due to its intermediate size likely exists for a number of similar divalent cations with ionic radii between 0.55 and 0.66 Å, including Ni, Cu, Co, Cd, Zn, Fe, and Mn (Shannon, 1976).

A1.3 Major Element Crystal Homogeneity

Identifying the effect of melt composition on partitioning requires varying melt compositions of experimental charges while simultaneously holding temperature, pressure, and crystal chemistry constant. To verify that the major element compositions of the anorthites were not varying between experiments or within individual laths, points across transects of two crystals from each of the seven controlled cooling experiments in the CMAS2b suite were analyzed for CaO, Al₂O₃, and SiO₂ by electron microprobe using a synthetic anorthite standard, 25 nA beam, 15 keV, and 30 s on peak and 15 s background. The wt. % data plotted in Figure A1.4 indicate no major element crystal heterogeneity within analytical precision. Points furthest from the crystal centers that are elevated (Al₂O₃ and SiO₂) or low (CaO) are at the edges of the crystals and either represent partial or full analyses of the surrounding glass composition.

Figure A1.4 (next page). Major element traverses from rim to rim across representative anorthite crystals from CMAS2b experiments: (a) and (b) 2b-1-2, (c) and (d) 2b-2-2, (e) and (f) 2b-3-2, (g) and (h) 2b-4-2, (i) and (j) 2b-5-2, (k) and (l) 2b-6-2, and (m) and (n) from 2b-7-2. Error bars represent 1 σ analytical uncertainty; those not visible lie within symbol size shown.

Figure A1.4 (cont.)



A2 CRYSTAL SELECTION

A2.1 Selection of Most Equant Crystal Cross Sections for Detailed Compositional Study

Collecting trace element composition data from crystal rims by selecting individual points to analyze can be a tedious process, so 2-D polygonal grids of 100-200 points across the short dimensions of anorthite laths were programmed for trace element (Mg, Sr, Ba) analysis as described in Section 2.2.4. This approach generated spatial data sets for identifying any compositional zoning present as well as measurements closest to the crystal edges without evidence of melt contamination. Crystals from which anorthite rim data were used to calculate partition coefficients are shown for the seven melt compositions in Figure A2.1.

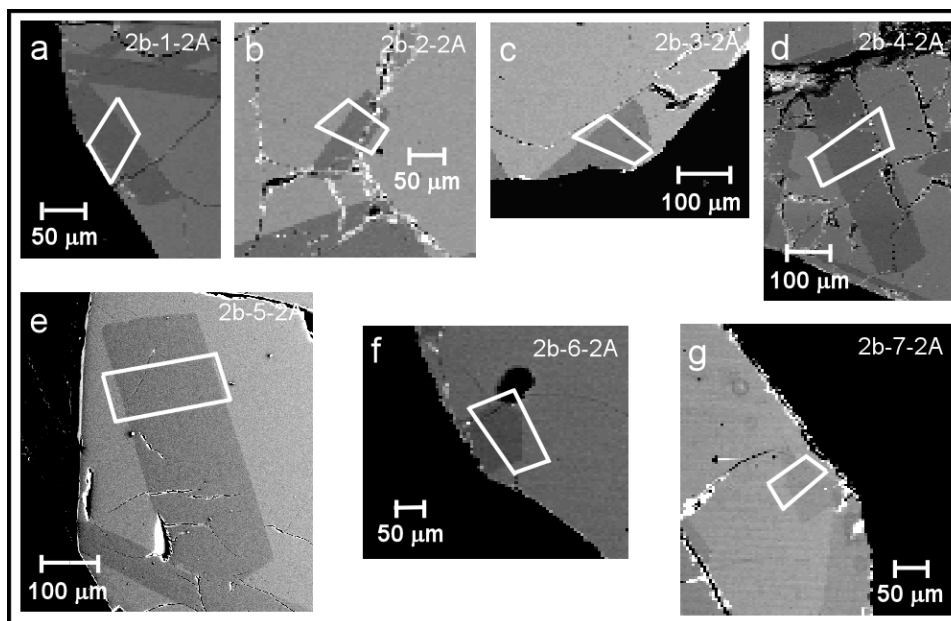


Figure A2.1. BSE imaging of locations of 2-D grid analyses of the most equant crystal (labeled A) from each of the seven CMAS2b compositions, with grid areas marked in white. (a) composition 2b-1, (b) composition 2b-2, (c) composition 2b-3, (d) composition 2b-4, (e) composition 2b-5, (f) composition 2b-6, and (g) composition 2b-7.

A.2.2 Trace Element Compositional Maps

Compositional maps of MgO, SrO, and BaO contents of crystals from the seven melt compositions studied in chapter 2 are plotted on the next seven pages. Analytical uncertainty for each datum is either at or less than the resolution of the legend color scale gradient shown for each element. Solid white lines delineate the boundaries between points completely contained within the crystal and those overlapping with, or fully containing glass, as determined both by composition and careful inspection of SEM imaging of probe spot burn marks in the sample carbon coat. Dashed white lines indicate regions within crystals that display anomalous compositions due to the presence of surficial features such as fractures. One dimensional summary transects were calculated from the 2-D data by averaging data points along lines roughly perpendicular to the A-B lines marked in each figure. Summary transects are plotted in Section A2.3.

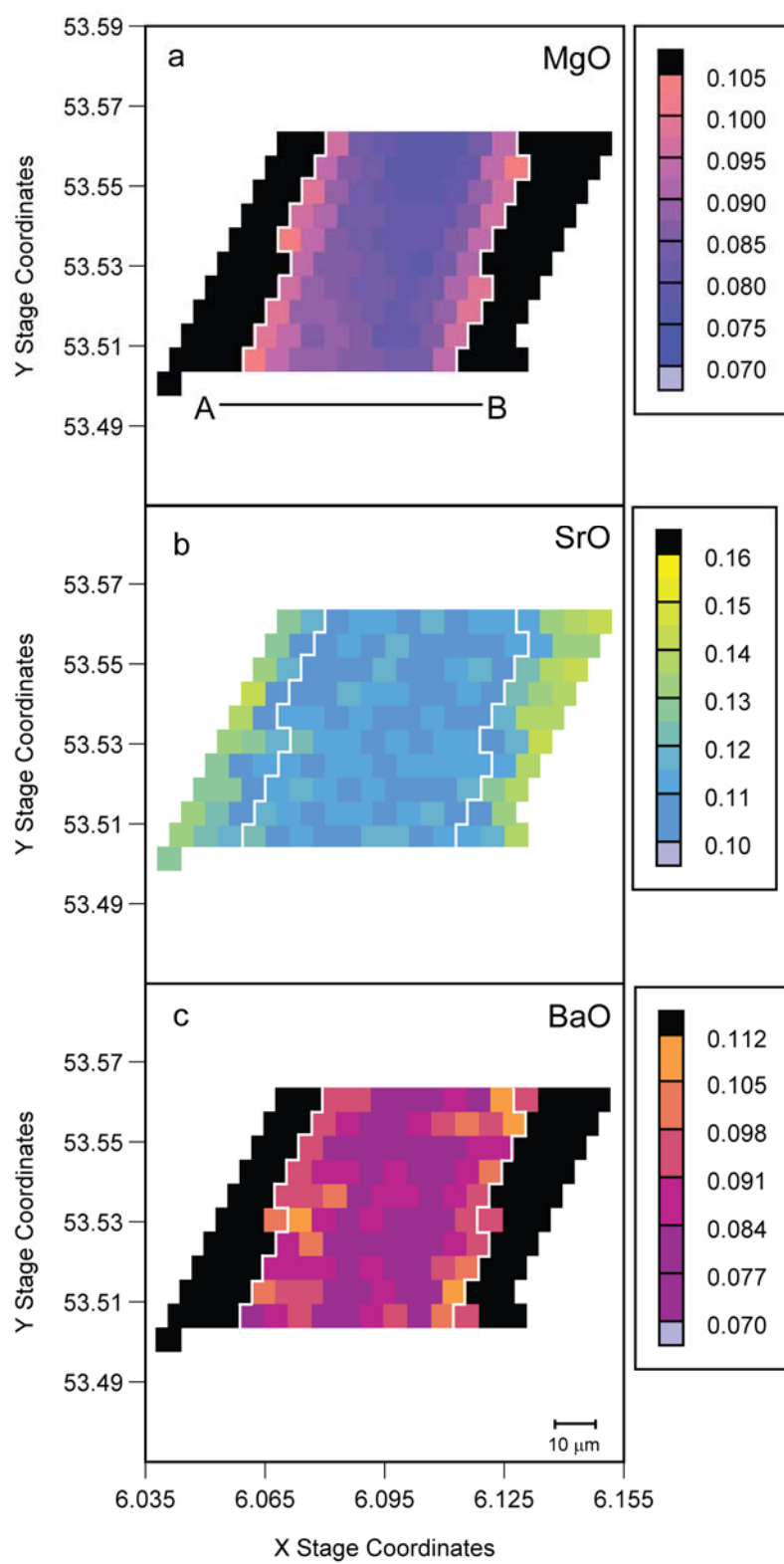


Figure A2.2. Sample 2b-1-2 (a) MgO, (b) SrO, (c) BaO maps (wt. %).

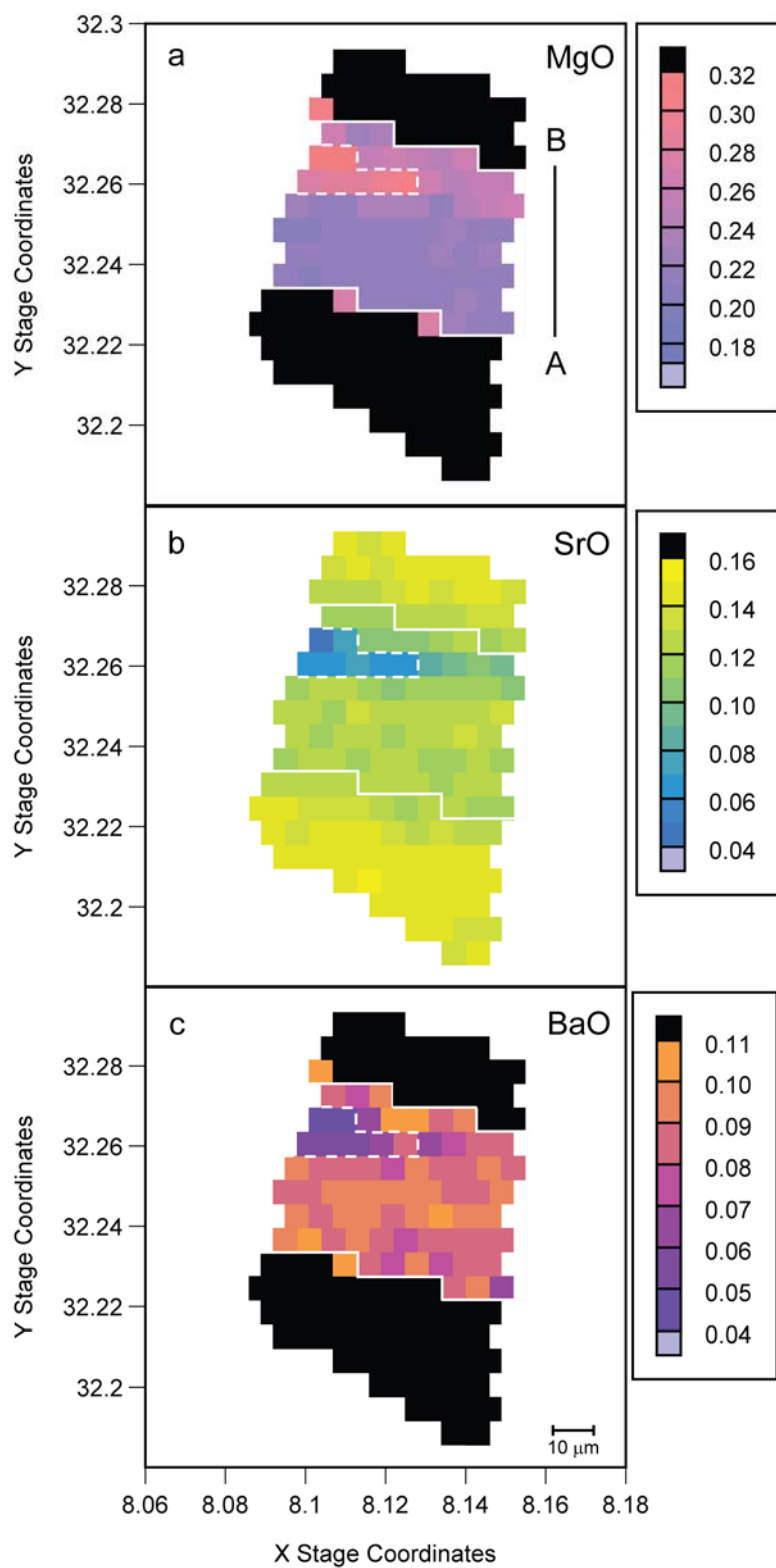


Figure A2.3. Sample 2b-2-2 (a) MgO, (b) SrO, (c) BaO maps (wt. %).

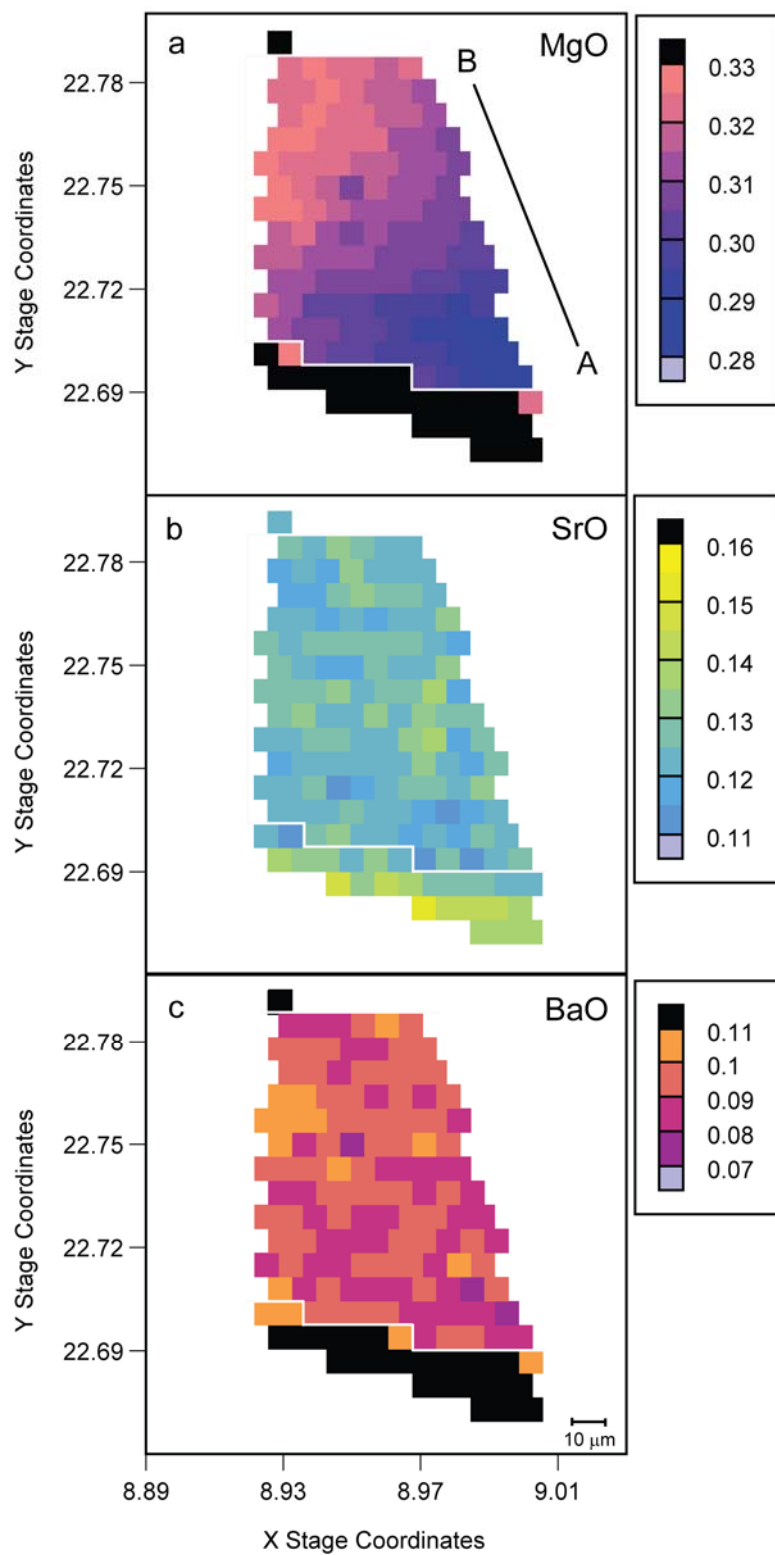


Figure A2.4. Sample 2b-3-2 (a) MgO, (b) SrO, (c) BaO maps (wt. %).

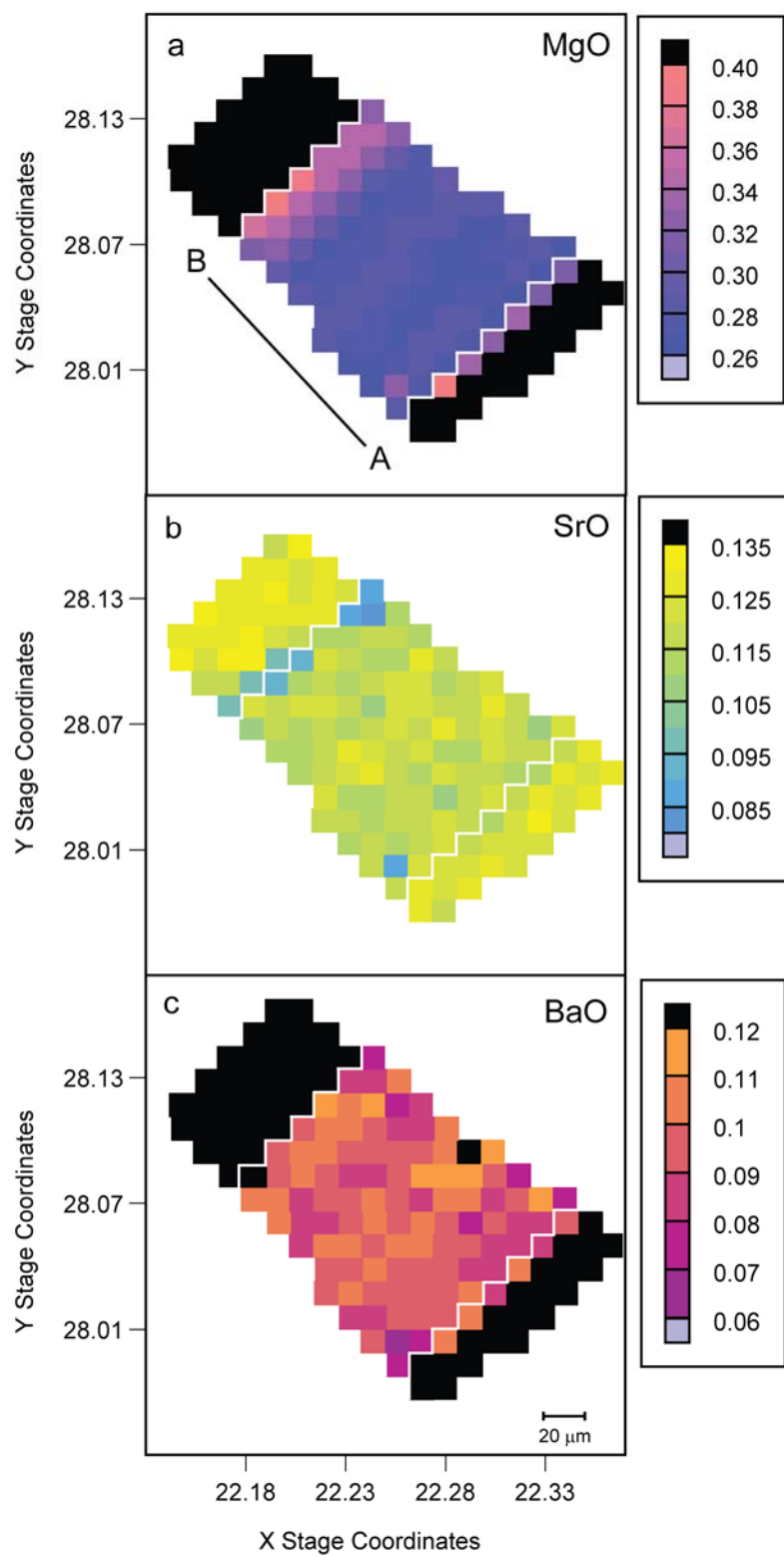


Figure A2.5. Sample 2b-4-2 (a) MgO, (b) SrO, (c) BaO maps (wt. %).

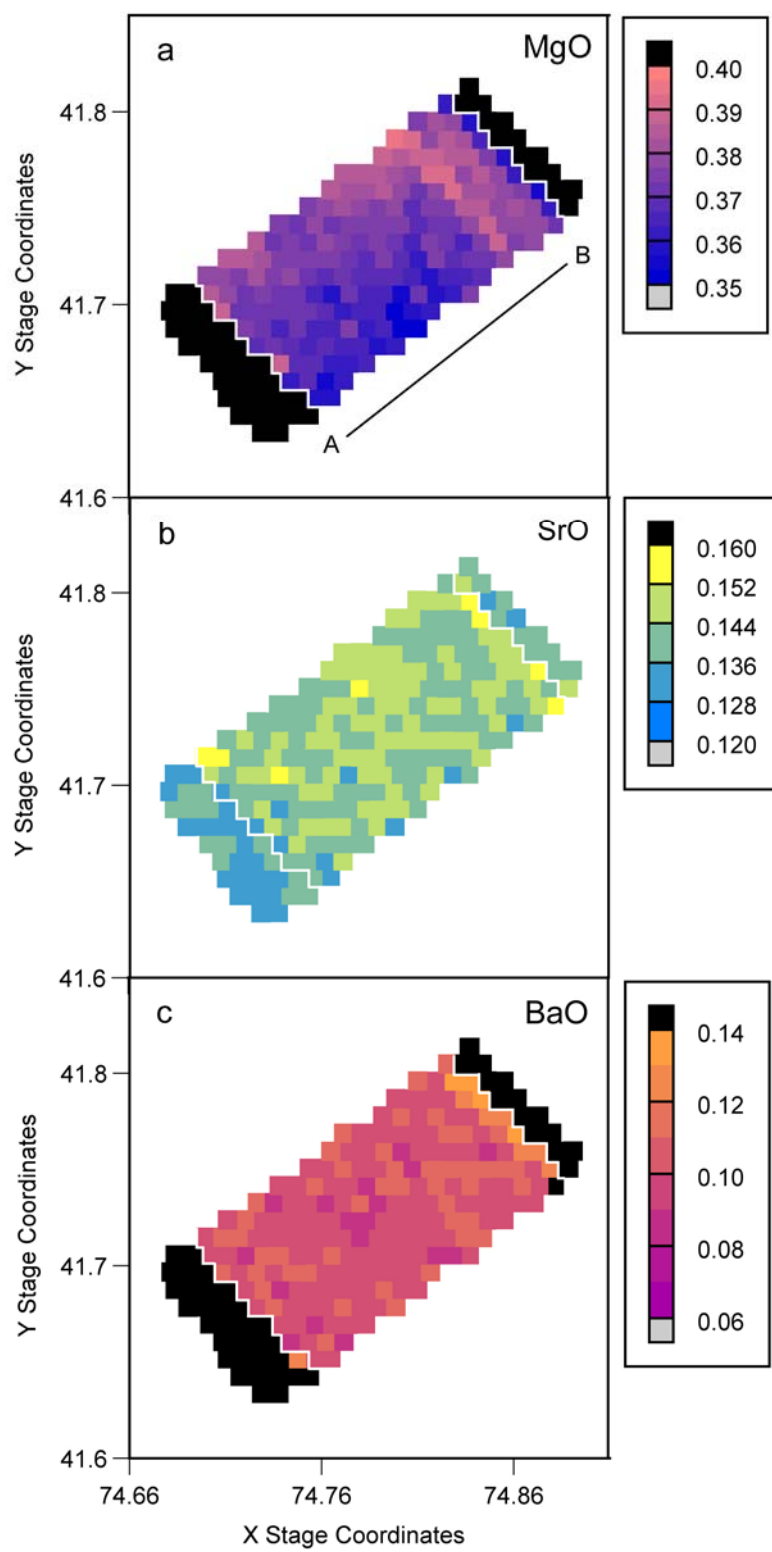


Figure A2.6. Sample 2b-5-2 (a) MgO, (b) SrO, (c) BaO maps (wt. %).

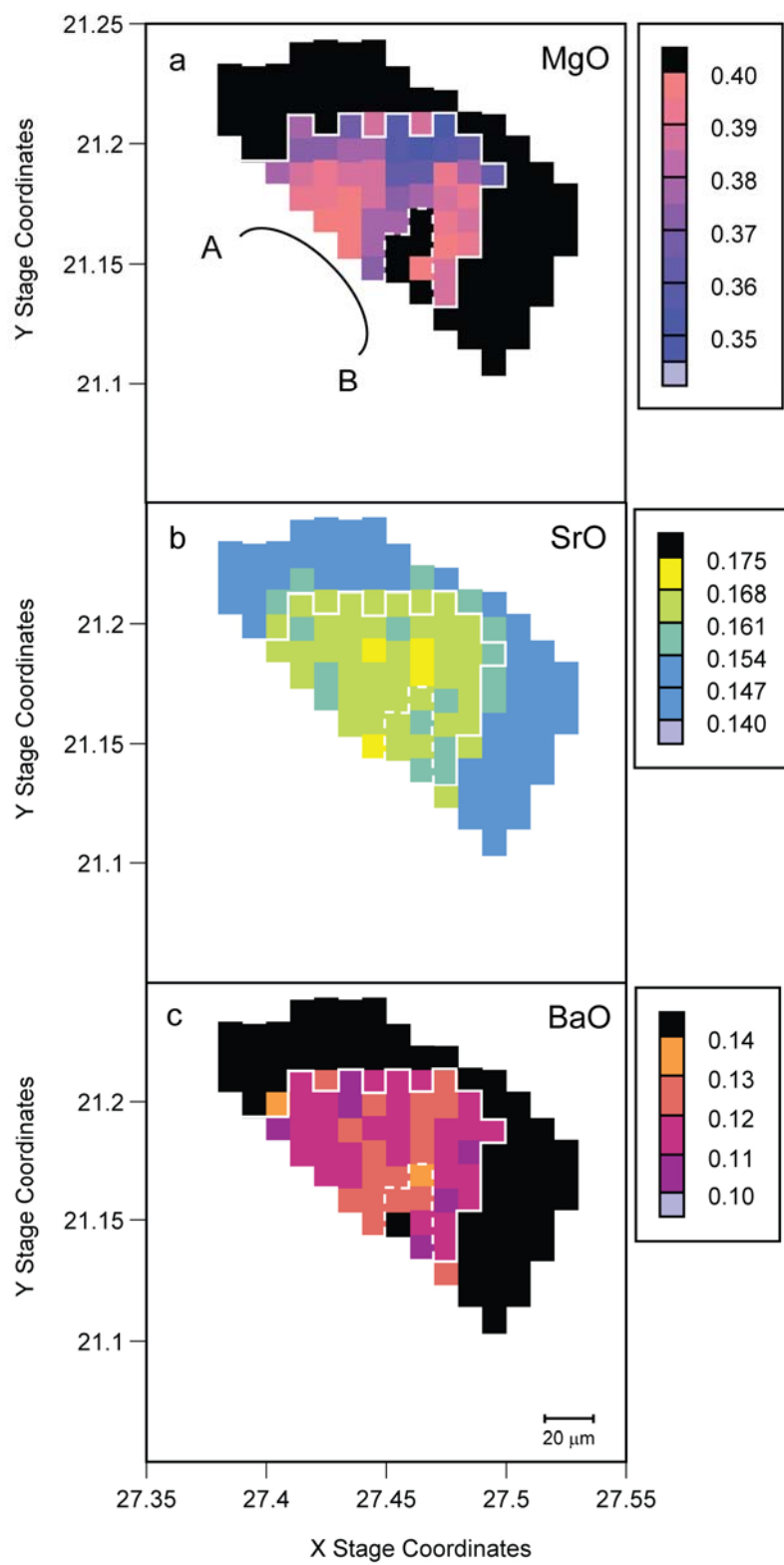


Figure A2.7. Sample 2b-6-2 (a) MgO, (b) SrO, (c) BaO maps (wt. %).

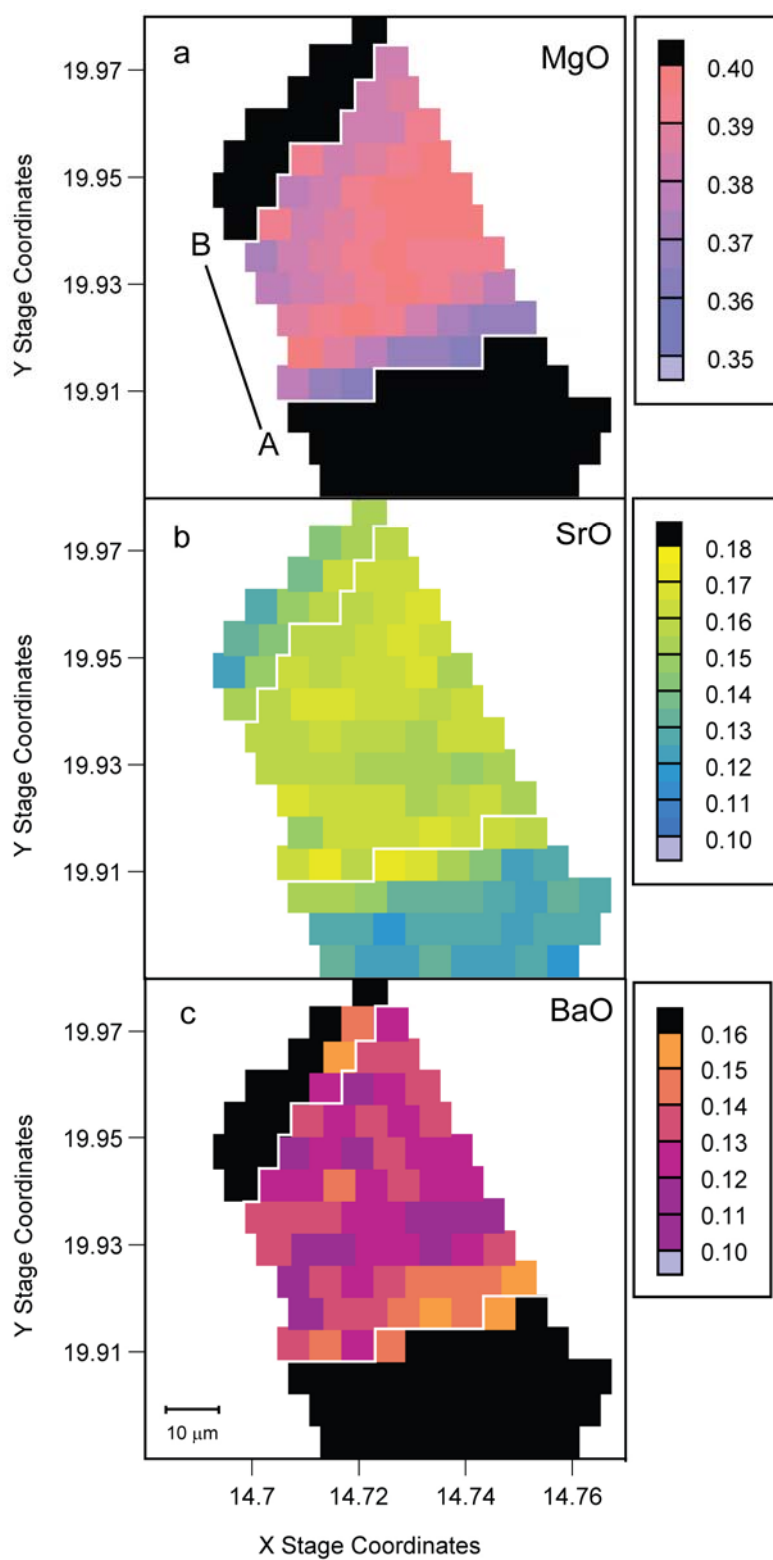


Figure A2.8. Sample 2b-7-2 (a) MgO, (b) SrO, (c) BaO maps (wt. %).

A2.3 Trace Element Summary Transects from 2-D Data of A2.2

While no evidence of major element zoning exists for anorthite crystals grown in the experiments described in chapter 2, the trace elements Mg, Sr, and Ba all display some degree of heterogeneity from core to rim in at least several of the sample transect summaries (Figure A2.9). SrO and BaO contents tend to display similar zoning behavior except for the crystal of 2b-1-2 in (a), where MgO and BaO closely track one another. Systematic trace element heterogeneity is not ubiquitous throughout this sample set and is barely present in several crystals, in particular (e) and (f). MgO zoning is most pronounced in (b) and (d), and in cases where one edge of a crystal clearly displayed higher MgO than the other, partition coefficients were calculated using data from the rim with the lower MgO content. Since the specific growth histories of each crystal are unknown, this approach assumed that growth may have been more rapid early during crystal formation and thus more likely to produce disequilibrium partitioning with higher levels of trace elements incorporated into the crystal structure.

Three crystals, labeled 'B' crystals, in 2b-1-2, 2b-4-2, and 2b-7-2, were also compositionally mapped to test if other crystals in these experiments would produce the same partition coefficients as the 'A' crystals. Results from the 'B' crystals confirmed the D values calculated from the 'A' data.

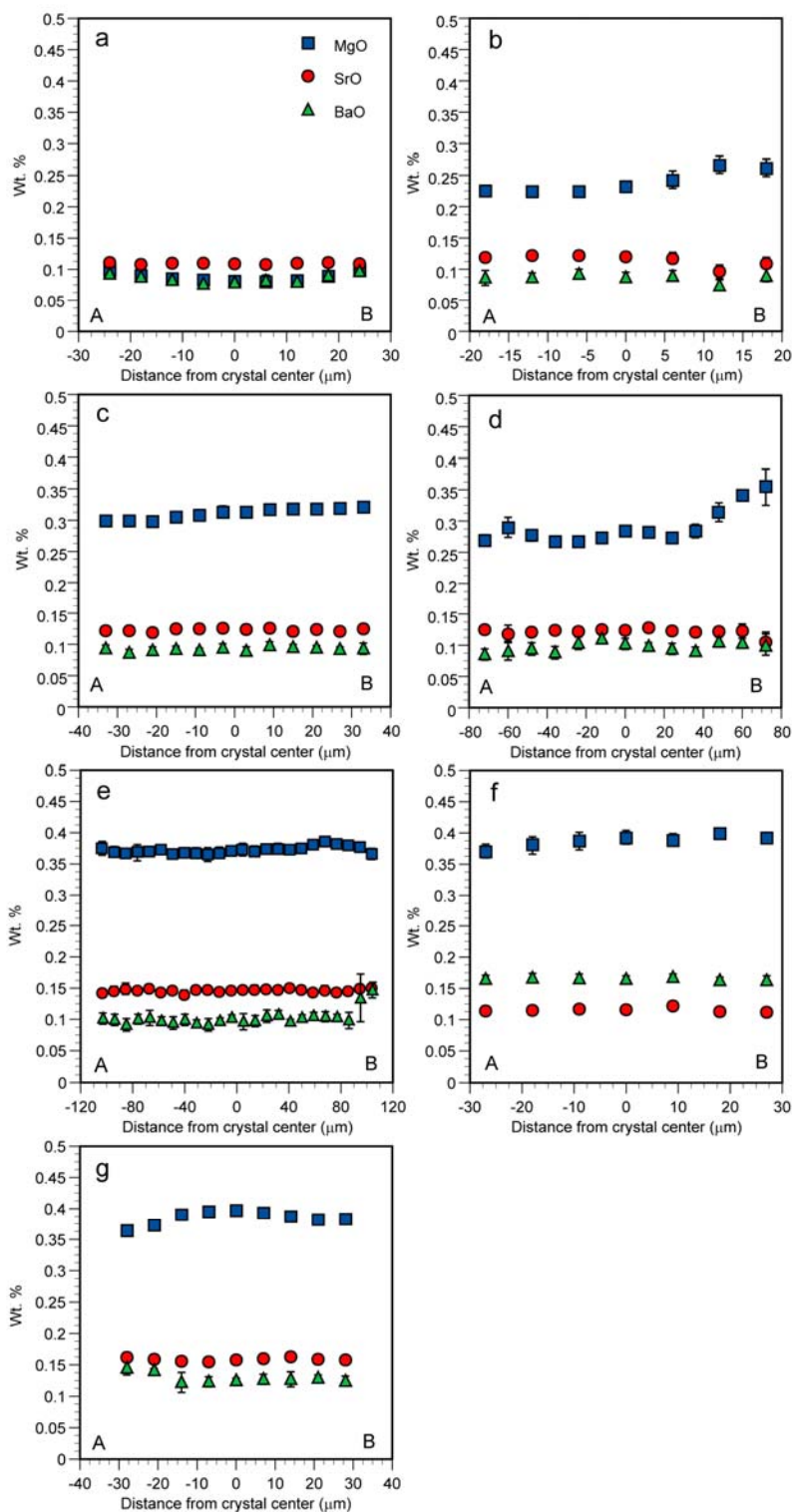


Figure A2.9. MgO (squares), SrO (circles), and BaO (triangles) transects summarizing zoning trends in the ‘A’ crystals of the seven melt composition grids in Section A2.2. 1 σ error is contained within the size of the symbols except where shown. (a) 2b-1-2, (b) 2b-2-2, (c) 2b-3-2, (d) 2b-4-2, (e) 2b-5-2, (f) 2b-6-2, (g) 2b-7-2.

A3 CRYSTAL GROWTH DYNAMICS

A3.1.1 Study of Crystal Growth During 2 °C/hr Dynamic Crystallization Experiments

Growth of an individual crystal cannot be visually tracked over the course of a controlled cooling experiment, but representative snapshots of crystallization progress during the thermal history of this study were obtained by stopping runs and quenching the run products at intermediate time points. Figure A3.1 shows charges from composition 2b-1 that were stopped at three separate times: (a) was quenched immediately after the completion of the first 2 °C/hr cooling step, (b) after the 24 hr hold interval in the middle of the run between the two cooling steps, and (c) immediately after the second 2 °C/hr cooling step. These images confirmed that crystallization had commenced prior to the intermediate 24 hour hold interval, which likely prevented major amounts of delayed nucleation and any resulting rapid disequilibrium growth, as discussed in Section 2.2.5, from influencing the bulk of the crystal formation or the rim compositions.

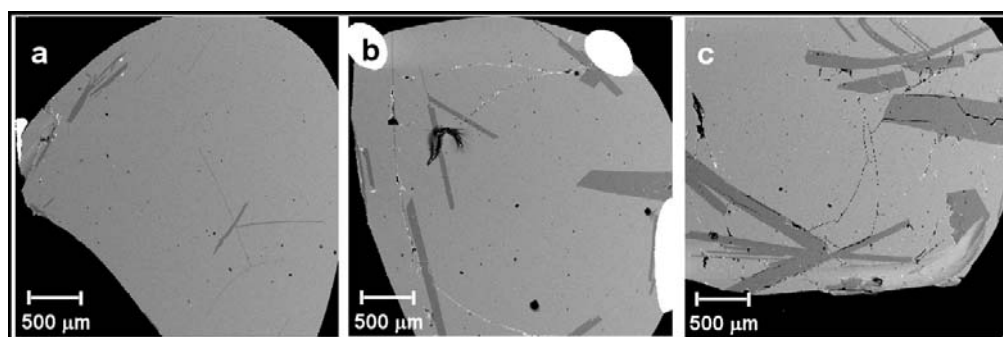


Figure A3.1. Representative BSE crystal images (2b-1-3, 2b-1-4, 2b-1-5) quenched at three intermediate time points (a) 20.5, (b) 44.5, and (c) 67 hours during the controlled cooling thermal regime of this study

A3.1.2 Glass Composition Evolution During Dynamic Crystallization Experiments

Average compositions based on random data points throughout the sample glass are reported for the initial fused compositions (Table A3.1); the three intermediate times of 20.5, 44.5, and 67 hours (Table A3.2); and the final melt composition at 96 hours (Table A3.3). These times represent the inflection points on the thermal history shown in Figure A1.2 both before and after controlled cooling intervals. Points for Table A3.2 were only analyzed for major elements Ca, Mg, Al, and Si, but the analytical conditions were the same as described in Section A1.3 for the major element transect analyses of the anorthite crystals. Analytical conditions for the initial and final melt compositions are given in Section 2.2.4.

Table A3.1. Starting compositions of glasses fused for three hours as analyzed by electron microprobe. 1 σ standard deviation uncertainty is shown in parentheses and applies to the final digit of each value.

| | 2b-1-1 n = 10 | 2b-2-1 n = 10 | 2b-3-1 n = 10 | 2b-4-1 n = 10 | 2b-5-1 n = 10 | 2b-6-1 n = 10 | 2b-7-1 n = 10 |
|--------------------------------|------------------|------------------|------------------|------------------|------------------|------------------|------------------|
| SiO ₂ | 46.6 (2) | 46.79 (9) | 46.6 (2) | 46.4 (2) | 45.8 (3) | 45.9 (2) | 46.0 (1) |
| Al ₂ O ₃ | 21.56 (6) | 21.79 (5) | 22.15 (5) | 22.56 (7) | 23.07 (7) | 24.02 (6) | 25.44 (9) |
| MgO | 0.99 (2) | 2.57 (5) | 4.30 (5) | 5.9 (1) | 7.78 (8) | 9.2 (2) | 10.1 (1) |
| CaO | 30.26 (7) | 28.4 (1) | 26.46 (7) | 24.4 (1) | 22.41 (8) | 20.37 (9) | 18.35 (9) |
| SrO | 0.13 (3) | 0.13 (3) | 0.14 (4) | 0.13 (3) | 0.13 (3) | 0.15 (3) | 0.12 (3) |
| BaO | 0.50 (8) | 0.5 (1) | 0.49 (4) | 0.51 (7) | 0.53 (6) | 0.52 (6) | 0.54 (9) |
| Na ₂ O | 0.01 (1) | 0.02 (1) | 0.02 (1) | 0.01 (1) | 0.02 (1) | 0.02 (1) | 0.01 (1) |
| K ₂ O | <u>0.023 (5)</u> | <u>0.025 (5)</u> | <u>0.023 (6)</u> | <u>0.023 (6)</u> | <u>0.025 (7)</u> | <u>0.022 (8)</u> | Na |
| | 100.07 | 100.23 | 100.10 | 99.93 | 99.77 | 100.20 | 100.56 |

na = not analyzed

Table A3.2. Major element glass compositions analyzed by EMP at three intermediate time steps along the dynamic crystallization path of Figure A1.2. 1 σ standard deviation of the analyses (not error of mean) is shown in parentheses and applies to the final digit of each value.

| | 20.5 hours | | | 44.5 hours | | | 67 hours | | |
|--------------------------------|------------------|------------------|------------------|-----------------|------------------|------------------|-----------------|------------------|------------------|
| | 2b-1-3 n = 30 | 2b-4-3 n =30 | 2b-7-3 n =30 | 2b-1-4 n =30 | 2b-4-4 n =30 | 2b-7-4 n =30 | 2b-1-5 n =30 | 2b-4-5 N =30 | 2b-7-5 n =30 |
| SiO ₂ | 47.3 (2) | 47.1 (2) | 45.9 (3) | 47.7 (2) | 47.6 (3) | 46.1 (3) | 48.0 (3) | 48.0 (3) | 46.6 (3) |
| Al ₂ O ₃ | 21.2 (2) | 21.9 (2) | 24.4 (2) | 20.5 (1) | 20.40 (7) | 23.40 (6) | 18.5 (3) | 18.3 (1) | 21.2 (2) |
| MgO | 0.99 (2) | 6.05 (7) | 10.6 (1) | 1.01 (2) | 6.62 (6) | 11.79 (7) | 1.14 (3) | 7.50 (7) | 13.6 (1) |
| CaO | <u>30.5 (1)</u> | <u>24.54 (8)</u> | <u>18.35 (9)</u> | <u>30.8 (1)</u> | <u>25.04 (7)</u> | <u>18.10 (7)</u> | <u>32.4 (1)</u> | <u>25.71 (9)</u> | <u>17.82 (6)</u> |
| | 99.99 | 99.59 | 99.25 | 100.01 | 99.66 | 99.39 | 100.04 | 99.51 | 99.22 |

Table A3.3. Final melt compositions after 96.5 hours from EMP analyses of glass points distributed throughout melt. 1 σ standard deviation uncertainty is shown in parentheses and applies to the final digit of each value. Note that these runs were held for 30 hours at the final temperature.

| | 2b-1-2 n = 10 | 2b-2-2 n =10 | 2b-3-2 n =10 | 2b-4-2 n =10 | 2b-5-2 n =10 | 2b-6-2 n =10 | 2b-7-2 n =10 |
|--------------------------------|------------------|------------------|-----------------|------------------|------------------|-----------------|-----------------|
| SiO ₂ | 48.0 (1) | 47.4 (3) | 47.86 (9) | 47.6 (3) | 46.3 (3) | 46.3 (3) | 46.4 (1) |
| Al ₂ O ₃ | 18.14 (9) | 17.8 (1) | 17.9 (2) | 18.03 (8) | 18.80 (7) | 19.8 (1) | 20.97 (6) |
| MgO | 1.17 (2) | 3.24 (4) | 5.5 (1) | 7.8 (1) | 10.40 (8) | 12.2 (2) | 14.2 (2) |
| CaO | 32.5 (2) | 30.7 (1) | 28.1 (1) | 25.9 (1) | 23.20 (8) | 20.25 (5) | 17.6 (1) |
| SrO | 0.13 (3) | 0.14 (3) | 0.14 (3) | 0.14 (3) | 0.11 (2) | 0.14 (3) | 0.13 (3) |
| BaO | 0.63 (9) | 0.57 (8) | 0.61 (9) | 0.64 (6) | 0.66 (4) | 0.71 (6) | 0.65 (7) |
| Na ₂ O | 0.01 (1) | 0.02 (1) | 0.02 (1) | 0.02 (1) | 0.02 (1) | 0.02 (1) | 0.02 (1) |
| K ₂ O | <u>0.021 (6)</u> | <u>0.019 (7)</u> | na | <u>0.026 (7)</u> | <u>0.023 (5)</u> | na | Na |
| | 100.60 | 99.89 | 100.13 | 100.16 | 99.51 | 99.42 | 99.97 |

na = not analyzed

The fraction of crystal growth for compositions 2b-1, 2b-4, and 2b-7 quenched at each time step shown in Figure A3.1 was calculated from the evolving melt compositions according to the fractional crystallization equation,

$$C_{i(t)} = C_{o(t)}(1-F)^{(D-1)}, \quad (\text{A2})$$

where the final composition of the liquid C_i is a function of the initial liquid concentration (C_o), the fraction crystallized (F), and the bulk partition coefficient

between the solid and liquid phases (D). The amounts of crystallization for the least magnesian (2b-1), most magnesian (2b-7), and an intermediate (2b-4) composition at five time points along the controlled cooling path of the experiments is shown in Figure A3.2.

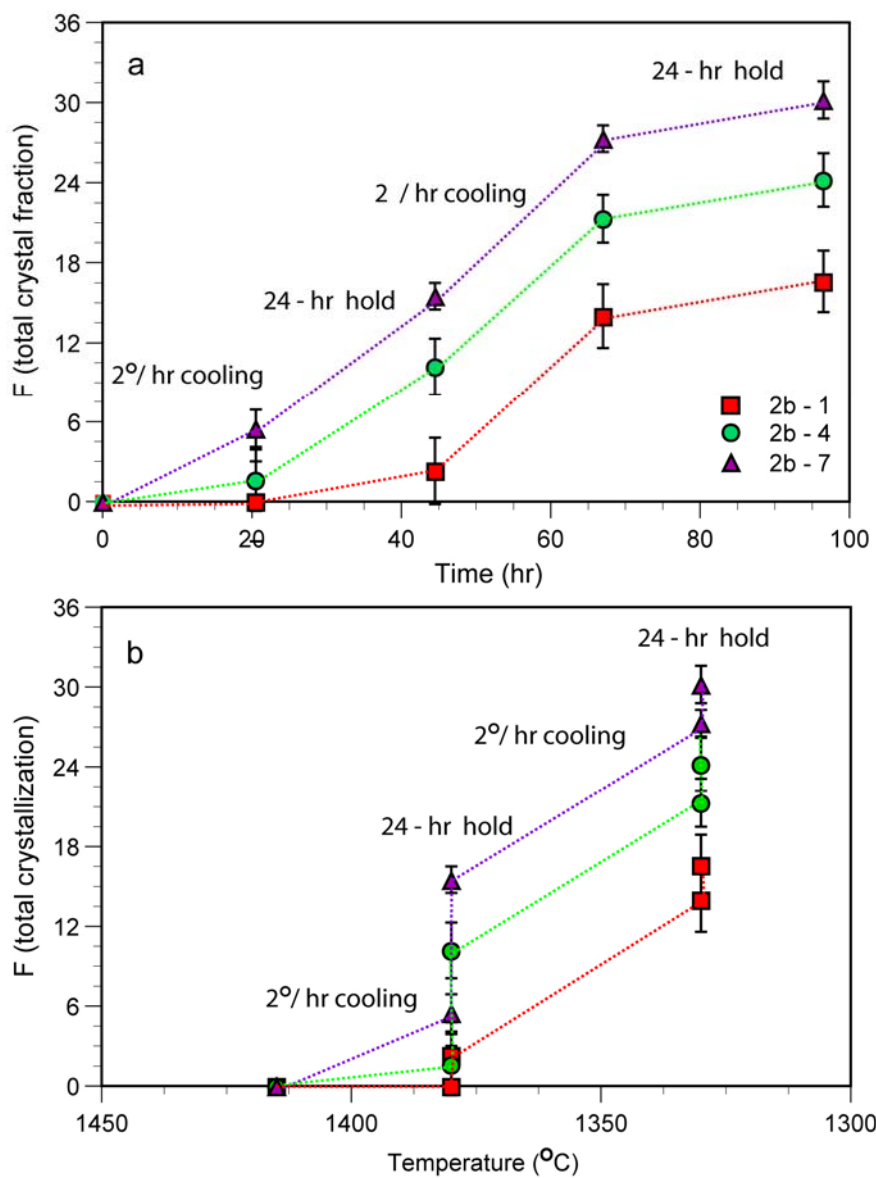


Figure A3.2. Calculated crystal fraction increases during the controlled cooling experiments for compositions 2b-1 (least magnesian), 2b-4, and 2b-7 (most magnesian) over ~ 100 hours as a function of (a) time and (b) temperature.

Plot (a) shows the progress of crystallization as a function of time spent in the furnace, and (b) represents the overall fraction of crystallization as a function of temperature, where crystallization occurring during isothermal periods appears as discontinuous jumps. MgO partition coefficients were used to calculate F since the differences in F generated by approximating apparent D values using initial vs. final melt compositions are small. Uncertainty in crystallization (1σ) was generally less than 0.03 of the fraction crystallized.

While extent of crystallization at each temperature is clearly different for each composition, with the least magnesian composition crystallizing less than the most magnesian, no large increase in crystallization between 67 and 96 hours is observed within error, as expected if crystal growth is continuous and does not lag as cooling proceeds. This offers some confidence that the systems are not rapidly growing crystals that are clearly out of equilibrium with their surrounding melts.

A3.1.3 Melt Homogeneity During Controlled Cooling Experiments

Alternating intervals of controlled cooling with 24 hr isothermal periods in the thermal program shown in Figure A1.2 were designed to slow crystallization progress over the course of experiments and avoid rapidly growing crystals significantly out of equilibrium with the coexisting melt phase. It was expected that crystallization would produce liquid inhomogeneities, and allowing the melts to rehomogenize during isothermal periods eliminates the need to select from varying final liquid composition data a particular composition to use with crystal rim data in calculating partition

coefficients. Analyzing major element glass contents of samples quenched at specific time points during a typical controlled cooling experiment offers an opportunity to evaluate the extent of liquid heterogeneities produced and how effectively diffusion during 24 hr isothermal holding removes them at the temperatures of this study.

To track global melt composition variations, we developed a heterogeneity index (HI) defined as HI = (1 σ of 10-30 random melt points)/(1 σ analytical error), reported as %. The standard deviations of glass major element composition data (Table A3.1 through A3.3) have been divided by the average instrumental counting statistics uncertainties for the analyses. Analytical error is calculated from the raw X-ray count electron microprobe data according to the following equation reported in (Kremser):

$$\varepsilon_{P-B} = \sqrt{\frac{N_P}{t_P^2} + \frac{N_B}{t_B^2}} / \left(\frac{N_P}{t_P} - \frac{N_B}{t_B} \right), \quad (\text{A3})$$

where N_P is the total number of on-peak counts, N_B the total number of background counts, t_P the on-peak count time, and t_B the background count time. HI values < 2 indicate a homogeneous material.

Plots of melt heterogeneity at the various time steps of the dynamic crystallization thermal regime described earlier in this section are shown for compositions 2b-1, 2b-4, and 2b-7 in Figure A3.3. Time = 20.5 hours represents quenching after the first 2 °/hr controlled cooling period, time = 44.5 hours was quenched after the first 24 hr hold at ~1380 °C, 67 hours = immediately after the second 2 °/hr controlled cooling period, and a final 30 hr hold (minimum of 24 hours for this step) was completed after 96 hours. CaO remains relatively homogeneous throughout the experiments, whereas Al₂O₃ exhibits the greatest variations in melt composition with peaks corresponding to times immediately after intervals of 2 °/hr reductions in temperature, as discussed above. Generally, the

Al₂O₃ inhomogeneities caused by crystallization present after 20.5 and 67 hours were removed by the isothermal periods completed at 44.5 and 96 hours. For all other elements, diffusion and/or convection efficiently erased heterogeneities as they were produced by crystallization. Other non-systematic variations present between the three melt compositions are interpreted as small (% level) inhomogeneities. Since 1 σ ratios are compared here, $0.5 < HI < 2$ are not considered significant.

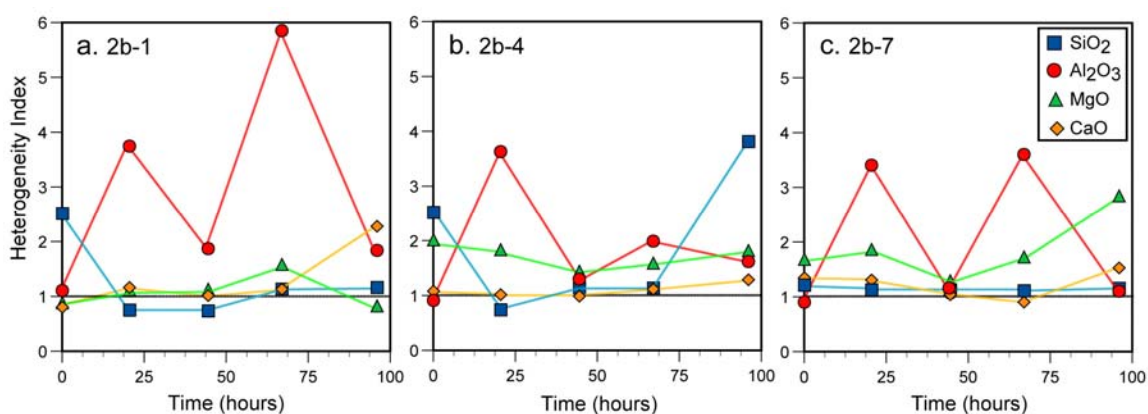


Figure A3.3. Heterogeneity index (HI) for melt major element oxide contents for compositions (a) 2b-1, (b) 2b-4, and (c) 2b-7 as a function of time in the controlled cooling program, where $HI = \% 1 \sigma$ of 10-30 random melt points / $\% 1 \sigma$ analytical error.

MgO heterogeneities are less pronounced but appear related to those of Al₂O₃, perhaps indicating a charge-compensating role for Mg²⁺ near Al³⁺ complexes in the melt structure. SiO₂ data are generally less precise than that of the other major oxides despite silica abundance, so differences in analytical error and compositional uncertainty arising from glass heterogeneity are less resolved. The HI values of Figure A3.3 show either little SiO₂ variation in the melts or, in the case of panel (b), apparently significant heterogeneity at 0 hours and 96 hours due to a combination of 70 % lower analytical error for those analyses and smaller number of analyses (10) than at 20.5, 44.5, and 67 hours

(30). Given that Si, as a network-former in melts, likely diffuses more slowly than Ca or Mg, the HI at times 0 and 96 may be better representations of general SiO₂ heterogeneity in these experiments than the HI calculated for the intermediate times.

Table A3.4 provides another view of Al₂O₃ heterogeneity development over the course of a typical controlled cooling experiment in this study. Al₂O₃ standard deviations exceed the instrumental error (0.3 % relative) after cooling intervals and return close to analytical uncertainty after the isothermal periods. The progressive return of Al₂O₃ variations to within analytical uncertainty at time = 96.5 hours as a function of melt major element composition (0.50, 0.44, 0.29 from least magnesian to most magnesian) suggests that diffusion rates may be higher in more magnesian compositions..

Table A3.4. Comparison of Al homogeneity in melt at time steps plotted in Figure A3.2. Typical analytical error ($\sqrt{\text{avg counts}}$ as % avg.) for Al₂O₃ is 0.3 %.

| Experiment # | Time in furnace (hrs) | Melt Al ₂ O ₃ Average wt. % | 1 σ as % avg. |
|--------------|-----------------------|---|----------------------|
| 2b-1-1 | Fuse (3) | 21.56 (6) | 0.28 |
| 2b-1-3 | 20.5 | 21.2 (2) | 0.94 |
| 2b-1-4 | 44.5 | 20.5 (1) | 0.49 |
| 2b-1-5 | 67 | 18.5 (3) | 1.62 |
| 2b-1-2 | 96.5 | 18.14 (9) | 0.50 |
| 2b-4-1 | Fuse (3) | 22.56 (7) | 0.31 |
| 2b-4-3 | 20.5 | 21.9 (2) | 0.91 |
| 2b-4-4 | 44.5 | 20.40 (7) | 0.34 |
| 2b-4-5 | 67 | 18.3 (1) | 0.55 |
| 2b-4-2 | 96.5 | 18.03 (8) | 0.44 |
| 2b-7-1 | Fuse (3) | 25.44 (9) | 0.35 |
| 2b-7-3 | 20.5 | 24.4 (2) | 0.82 |
| 2b-7-4 | 44.5 | 23.40 (6) | 0.26 |
| 2b-7-5 | 67 | 21.2 (2) | 0.94 |
| 2b-7-2 | 96.5 | 20.97 (6) | 0.29 |

These results indicate that except for Al₂O₃ even random melt points some distance from the anorthite crystals do not show any measurable degree of compositional variation 67

hours into the thermal program, when the furnace stops at a final temperature and anorthite crystallization apparently ceases.

A3.2 Near-Crystal Melt Homogeneity Test

Two dimensional compositional maps similar to those described in Section 2.2.4 for the anorthite crystals were analyzed for MgO, SrO, and BaO. The samples were 2b-1-5, 2b-4-5, and 2b-7-5, which had been quenched after 67 hours (Table A3.2). Analytical conditions were identical to those of Section 2.2.4 except that since most of analyses were on glass, the beam current was reduced to from 400 to 200 nA. The trace element grids extended from the outermost crystal edges approximately 100 μm into the melt, perpendicular to the crystal-melt interface. Two grids per sample were analyzed and their locations are shown in Figure A3.4. Polygonal point data for MgO, SrO, and BaO are reported in wt. % and crystal boundaries and summary transects were constructed as described in Section A2.2 for the anorthite 2-D compositional maps.

Figure A3.5 of 2b-1-2 melt grids shows a possible very slight elevation in MgO and BaO in the glass nearest the crystal-melt interface in (a) and (c), but this variation is not statistically significant in the summary transects of (d), and the melt grid data in the right column indicate no systematic concentration gradients parallel to the crystal edge. Little evidence of growth-related melt composition gradients exists for sample 2b-4-5 (Figure A3.6), though some MgO heterogeneity perpendicular to the interface is shown in (e) of that figure. The clearest demonstration of melt concentration gradients produced by crystal growth are found around anorthite laths in composition 2b-7, where MgO melt

contents in both (a) and (e) are elevated 1–7% near the crystal-melt interface relative to those of glass analyses 15–20 μm further away. SrO and BaO contents show no variation, though in all six melt grids analyzed it is possible, and even likely, that trace element concentration gradients exist within 5 μm of the interface below the spatial resolution of the electron beam. Improvements in quantitative TEM EDS technology may make these regions accessible to further study.

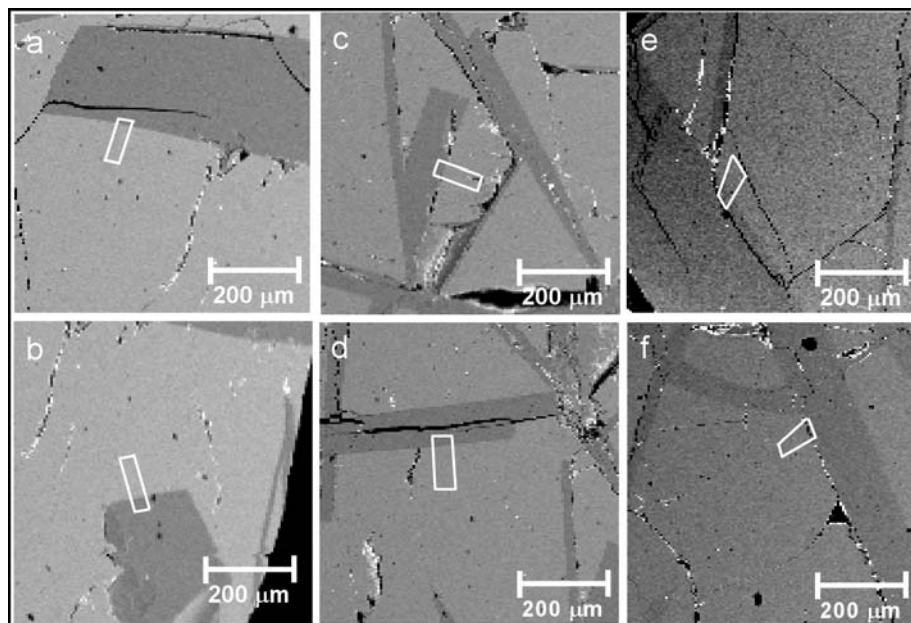


Figure A3.4. BSE imaging of melt grid locations for runs quenched 67 hours into a controlled cooling experiment of the thermal regime shown in Figure A1.2. (a) and (b): sample 2b-1-5, (c) and (d): sample 2b-4-5, and (e) and (f): sample 2b-7-5.

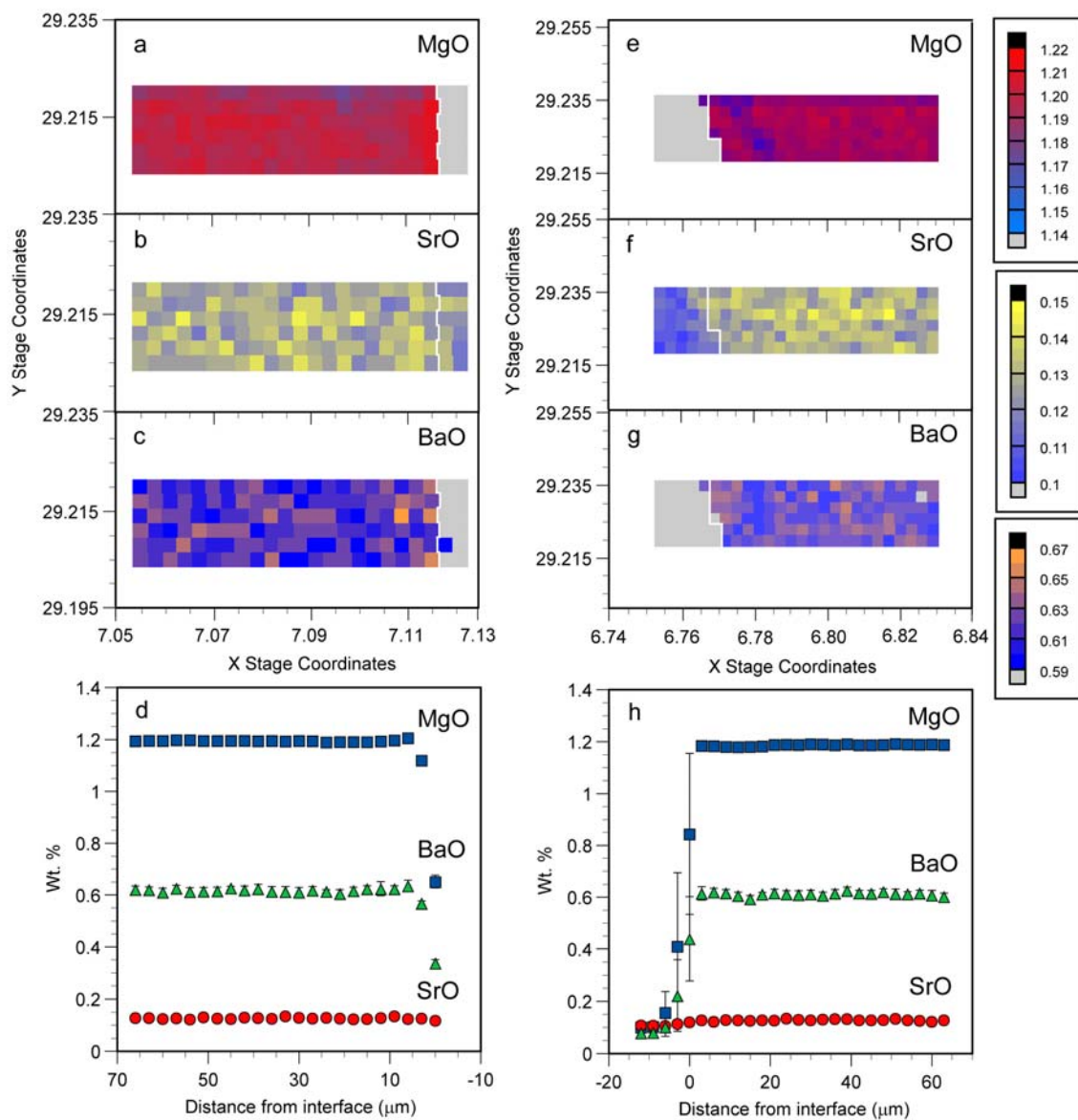


Figure A3.5. Sample 2b-1-5: Two grid melt maps of MgO, SrO, BaO wt. % data and summary transect for each grid.

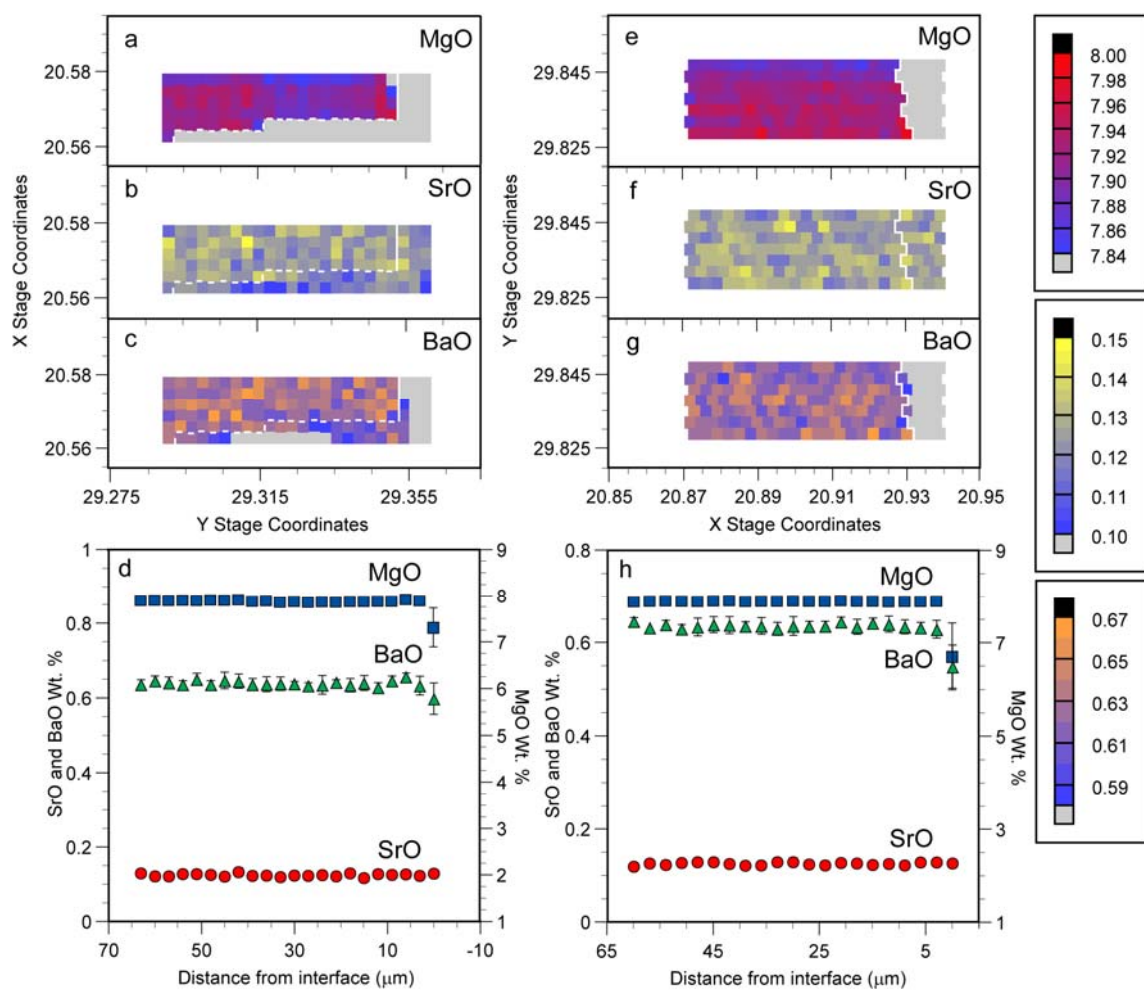


Figure A3.6. Sample 2b-4-5: Two grid melt maps of MgO, SrO, BaO wt. % data and summary transect for each grid.

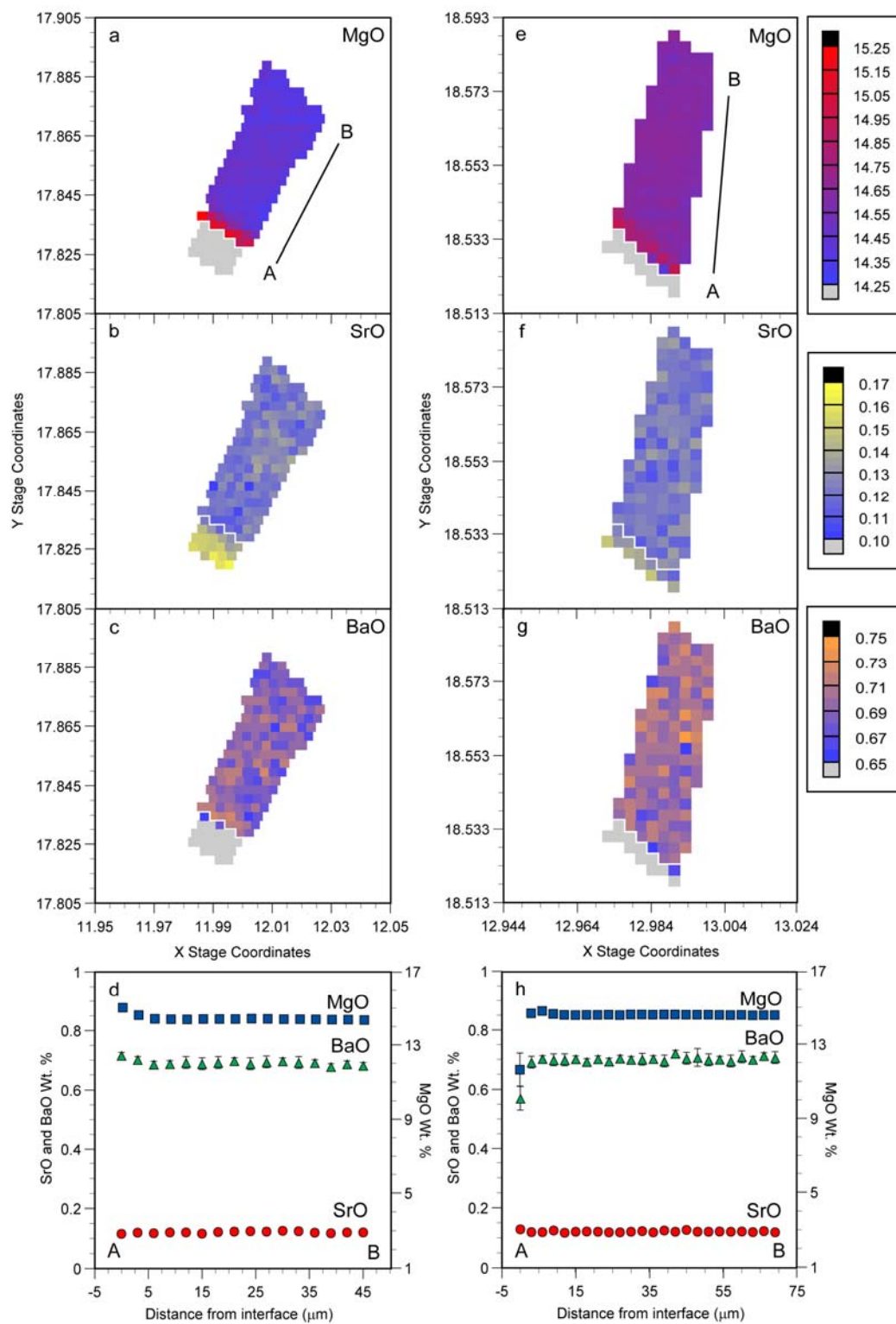


Figure A3.7. Sample 2b-7-5: Two grid melt maps of MgO, SrO, BaO wt. % data and summary transect for each grid.

A3.3 Effects of Crystal Growth Rate on Partitioning: Rapid (20 °/hr) Controlled Cooling Partitioning Study and Crystal Growth Dynamics

Rapid crystal growth can significantly influence apparent partition coefficients by incorporating elevated amounts of slow-diffusing incompatible trace elements into the crystal structure. When the time necessary to fully equilibrate crystal contents with the surrounding melt exceeds experimental feasibility, consideration of crystal growth effects on partitioning in the specific system(s) of interest becomes important. This section compares partition coefficients obtained by the controlled cooling thermal regime shown in Figure A1.2, which consisted of isothermal intervals and two 2 °C/hr cooling steps, and partition coefficients calculated for experimental runs in which crystals were grown by reducing the furnace temperature by 20 °C/hr to approximately the same final temperature as the 2 °C/hr cooling runs. The 20 °C/hr cooling experiments (2b-1-7, 2b-4-7, 2b-7-9) included no isothermal intervals and total run durations were 5-6 hours, as shown in Table A6.1.

A3.3.1 Compositional Data for Rapid Growth (20 °C/hr Cooling) Experiments

Trace element contents of the anorthite crystals and surrounding glass from the 20 °C/hr cooling experiments were obtained according to the methods detailed in Section 2.2.4 and A2.1, except these samples were analyzed using the new Caltech JEOL JXA-8200 electron microprobe. The analytical error associated with single point analyses of anorthite and glass MgO, SrO, and BaO contents are reported in Table A3.5. Average instrumental errors for data from the intermediate composition 2b-4 are represented by experiment 2b-4-2 data, measured using the older JEOL 733 electron microprobe, and

2b-4-7 using the new JEOL JXA-8200. MgO and SrO instrumental error is similar for both probes, but the JEOL JXA-8200 detected higher count rates in the $L\alpha$ LiF crystal X-ray line region for Ba, producing better BaO data.

Table A3.5. Percent analytical error for anorthite and glass trace elements analyzed on the new JEOL JXA-8200 electron microprobe compared to that on the older JEOL 733 model.

| | MgO | SrO | BaO |
|---------------------------|------|-----|-----|
| 2b-4-2 with JEOL 733 | | | |
| Anorthite: | 0.4 | 3.5 | 7.1 |
| Glass: | 0.07 | 3.3 | 1.6 |
| 2b-4-7 with JEOL JXA-8200 | | | |
| Anorthite: | 0.4 | 3.2 | 4.1 |
| Glass: | 0.07 | 3.3 | 0.9 |

Locations of the 2-D polygonal analysis grids for the three 20 °C/hr cooling experiment samples are shown in Figure A3.8.

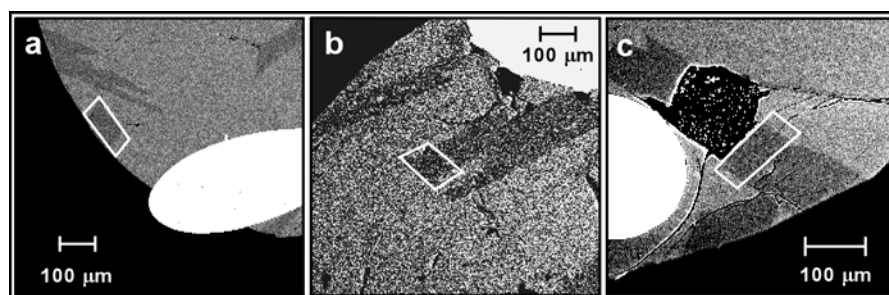


Figure A3.8. BSE imaging of 2-D compositional mapping grids (outlined in white) for trace element (MgO, SrO, BaO) analysis of 20 °C/hr cooling experiments: (a) 2b-1-7, (b) 2b-4-7, and (c) 2b-7-9.

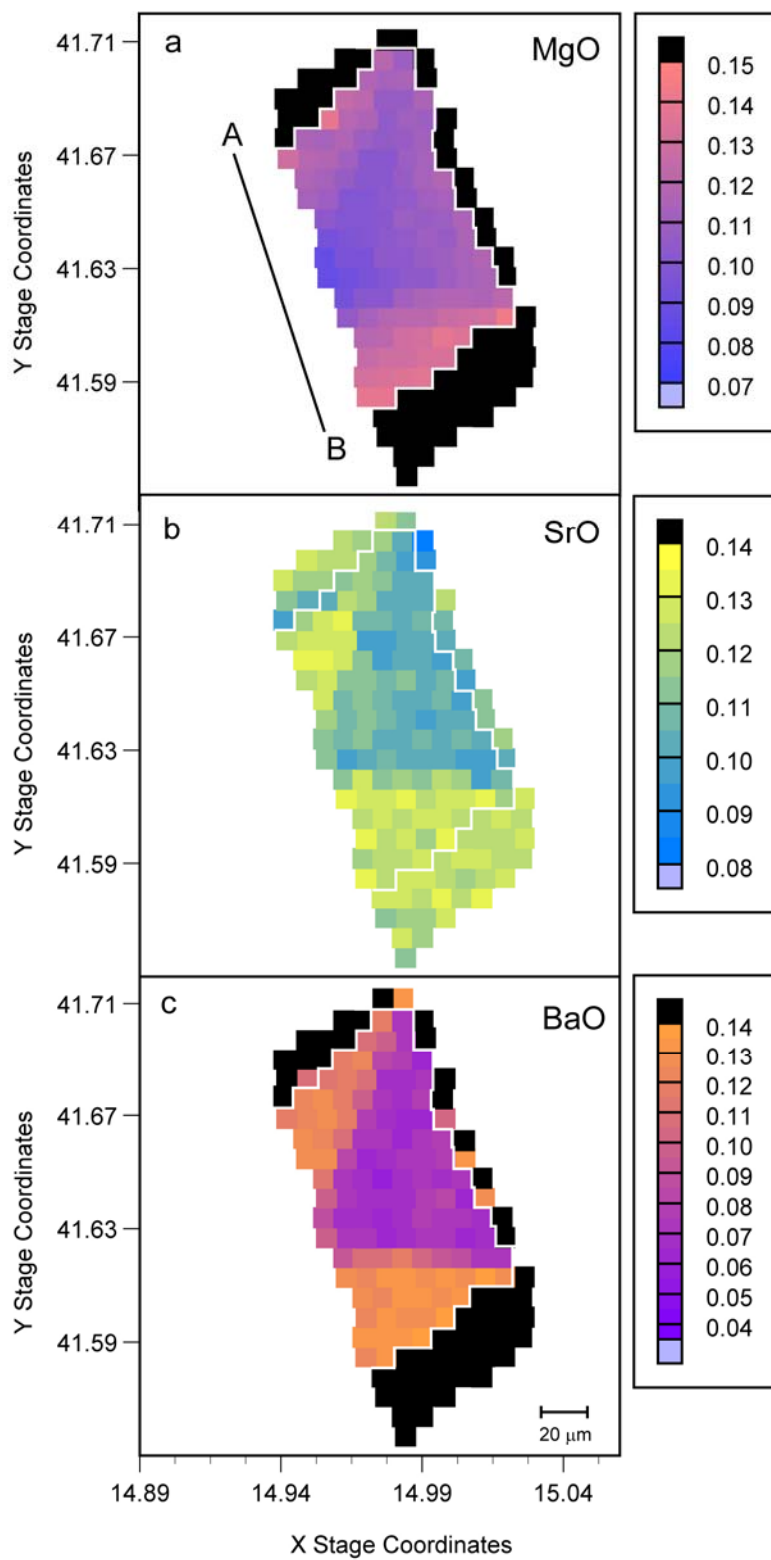


Figure A3.9. Sample 2b-1-7 (a) MgO, (b) SrO, (c) BaO maps (wt. %).

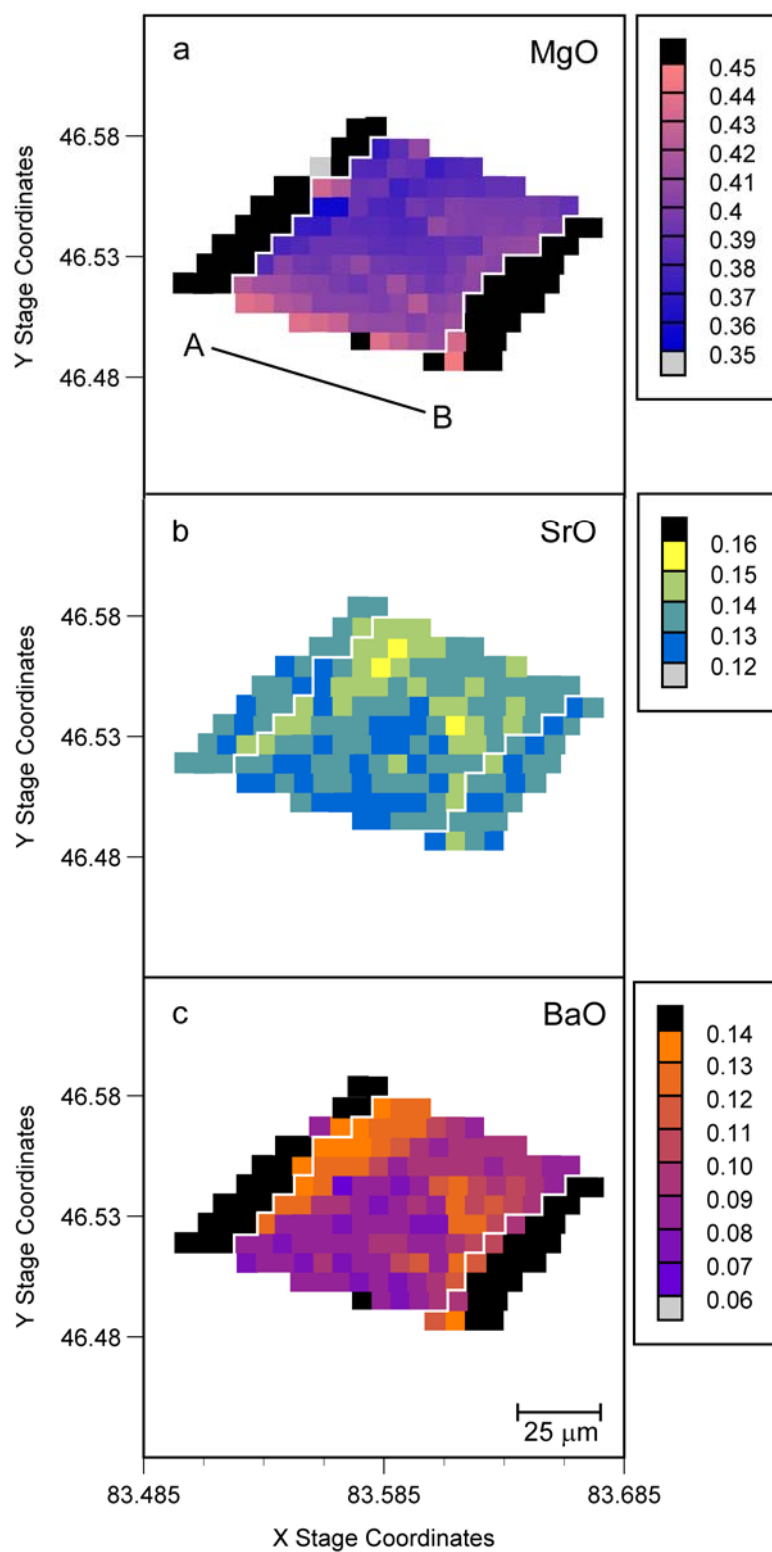


Figure A3.10. Sample 2b-4-7 (a) MgO, (b) SrO, (c) BaO maps (wt. %).

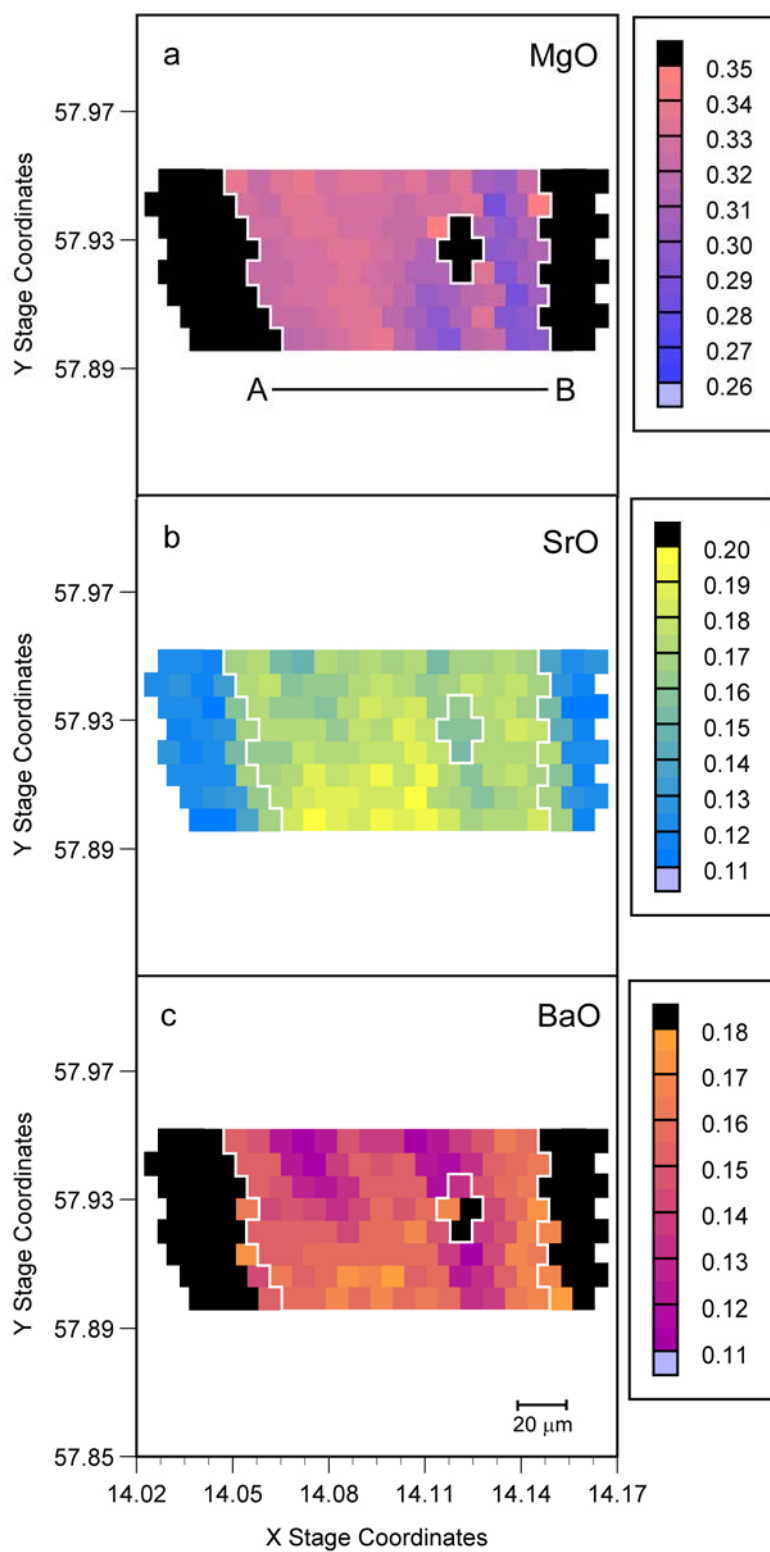


Figure A3.11. Sample 2b-7-9 (a) MgO, (b) SrO, (c) BaO maps (wt. %)

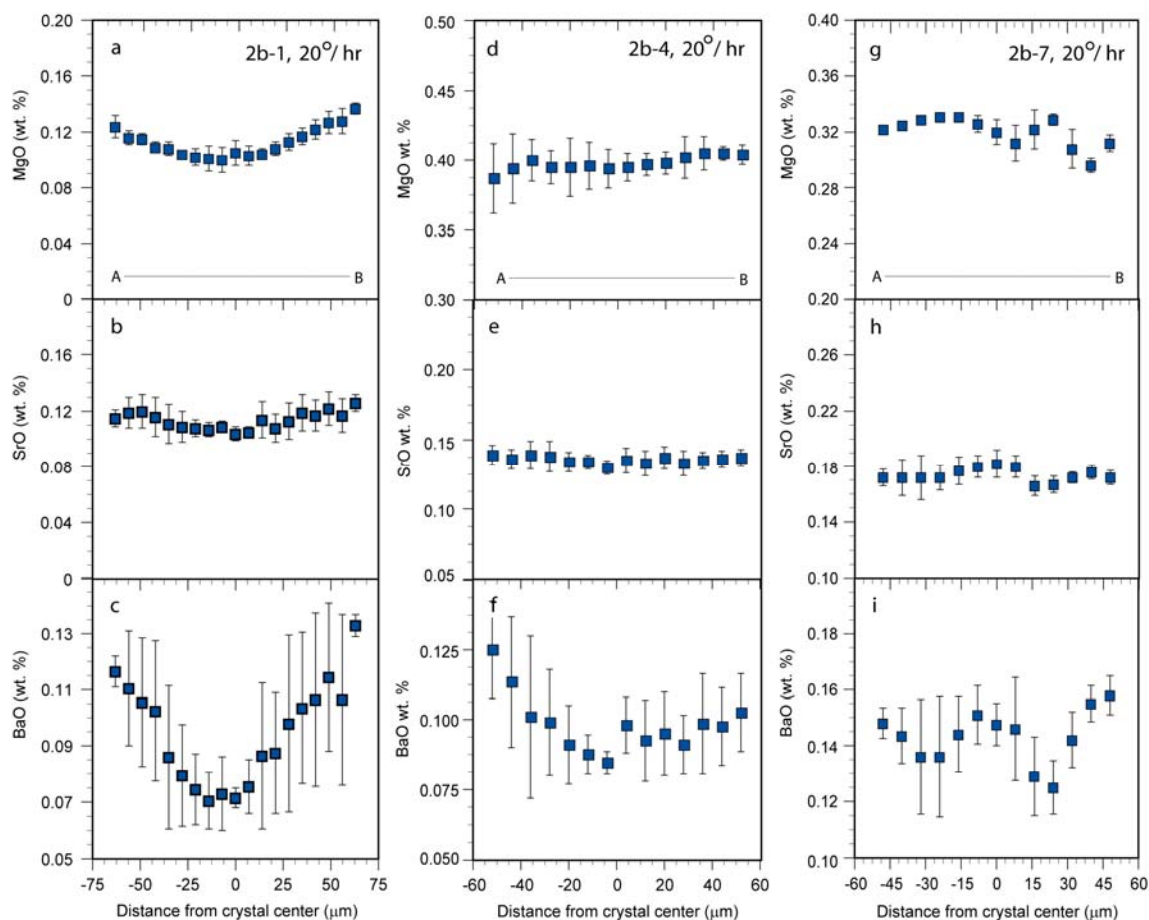


Figure A3.12. Trace element summary transects from grid data of 2b-1-7, 2b-4-7, and 2b-7-9.

Maps of individual wt. % data points for MgO, SrO, and BaO are given in Figures A3.9, A3.10, and A3.11 for sample charges 2b-1-7, 2b-4-7, and 2b-7-9, respectively. Summary transects across the crystals (rim to rim) that average data rows perpendicular to the A-B lines shown on the map figures are plotted in Figure A3.12. Note that summary transects suppress some compositional structure resulting from sector zoning.

The 20 °C/hr cooling experiment trace element data reveal formation of distinct sector zoning in 2b-1-7 and 2b-4-7, particularly in the SrO and BaO data, that was not

apparent in the maps of crystals grown under 2 °C/hr conditions. Composition 2b-7 may also be capable of producing crystals with this classic kinetic disequilibrium feature; 2b-7-9 composition maps (Figure A3.11) show clear variations in trace element distributions but the availability of well-formed, semi-equant laths in the polished cross section of the sample, which would have been better candidates for observing sector zoning, was limited.

Table A3.6 below summarizes molar partitioning data for trace elements Mg, Sr, and Ba from quantitative electron microprobe mapping of most equant crystals and surrounding glass from runs 2b-1-2 and 2b-1-2 (2 °C/hr cooling) and runs 2b-1-7 and 2b-7-9 (20 °C/hr) cooling. Partition coefficients are calculated from the crystal rim data and the adjacent glass. Composition 2b-1 starting material has the least magnesium (~1 wt. %) and 2b-7 has the most (~12 wt. %). Numbers in parentheses are 1 σ uncertainties on the final digit of each value.

Table A3.6. Comparison of 20 °C/hr to 2 °C/hr Mg, Sr, Ba D rim values for 2b-1, 2b-4, and 2b-7.

| <u>2b-1</u> | | <u>2 °C/hr</u> | <u>20 °C/hr</u> |
|-------------|-----------------|----------------|-----------------|
| | D^{mol}_{MgO} | 0.091 (5) | 0.120 (8) |
| | D^{mol}_{SrO} | 0.90 (5) | 1.02 (7) |
| | D^{mol}_{BaO} | 0.18 (2) | 0.25 (1) |
| <u>2b-4</u> | | | |
| | D^{mol}_{MgO} | 0.052 (4) | 0.058 (2) |
| | D^{mol}_{SrO} | 1.06 (5) | 1.19 (6) |
| | D^{mol}_{BaO} | 0.18 (2) | 0.21 (3) |
| <u>2b-7</u> | | | |
| | D^{mol}_{MgO} | 0.029 (1) | 0.027 (1) |
| | D^{mol}_{SrO} | 1.45 (6) | 1.66 (9) |
| | D^{mol}_{BaO} | 0.21 (2) | 0.29 (1) |

D^{mol} values of the 20 °C/hr cooling experiments are slightly elevated relative to those of the 2 °C/hr cooling runs, and this proportional elevation appears correlated with ionic radius, in particular in composition 2b-7, which shows no difference in D^{mol}_{MgO} but some for SrO and BaO. It should be noted that the partition coefficients reported in Table A3.5 represent the maximum observed effect the 20 °C/hr cooling rate could have on apparent partitioning behavior, since in the case of 2b-1-7 and 2b-4-7 composition data from the edges with the highest trace element abundances were used to calculate the D values shown. If those sectors grow before the sector(s) with lower trace element contents, the latter may represent the true crystal contents grown in closer equilibrium with the surrounding melt and the D values will be closer to those calculated from the 2 °C/hr cooling experiments. Either way, a significantly more pronounced effect on partition coefficients with cooling rate was observed by LaTourrette (1993) for U and Th clinopyroxene-melt partition coefficients ($fO_2 = QFM$), as shown in Table A3.7.

Table A3.7. Clinopyroxene-melt D_U and D_{Th} for experiments cooled at 0.1 °C/hr and 1.7 °C/hr (LaTourrette, 1993).

| D2-TUBAS | 0.1 °C/hr | 1.7 °C/hr |
|----------|------------|-------------|
| D_U | 0.0033 (3) | 0.0058 (8) |
| D_{Th} | 0.0069 (8) | 0.0120 (15) |

The D2-TUBAS partition coefficients are averages of 2-3 crystals because they derive from fission (^{235}U) and alpha (^{230}Th) track counting within crystal interior areas at least 20 μm from the edges, and thus each crystal represents one measurement of trace

element concentration in the solid phase. The differences in U and Th D values due to a factor of ~ 20 in cooling rate resulted in a doubling of the partition coefficients, which is a significantly greater effect than we observe for the alkaline earths in our experiments.

A3.3.2 Rapid Growth Effects on Lattice Strain Model Parameterizations

Lattice strain parameters D_o , r_o , and E from the crystal chemical partitioning model of Blundy and Wood (1994) have been calculated using the divalent element partition coefficients of SrO and BaO from the 20 °C/hr cooling experiment data and compared with partitioning behavior observed for the 2 °C/hr cooling experiments, as reported in Table 2.3 of section 2.3.1. Parameter fitting follows procedures described in Section 2.3.4 using the NMinimize function of Mathematica, which employ Nelder-Mead solution methods for non-linear equations.

Table A3.8. Lattice strain parameterizations for compositions 2b-1, 2b-4, and 2b-7 under 2 °C/hr and 20 °C/hr cooling conditions using the molar partition coefficient data for SrO and BaO from Table A3.3.1 and that of CaO from chapter 2.

| | | D_o | E (GPa) | r_o (Å) |
|---|------|---------|-----------|-----------|
| <u>2 °C/hr</u> | 2b-1 | 0.961 | 107.5 | 1.217 |
| | 2b-4 | 1.173 | 109.6 | 1.209 |
| | 2b-7 | 1.652 | 111.4 | 1.200 |
| <u>20 °C/hr</u> | 2b-1 | 1.014 | 99.5 | 1.229 |
| | 2b-4 | 1.278 | 115.7 | 1.218 |
| | 2b-7 | 1.807 | 112.2 | 1.214 |
| Effect of increasing cooling rate by factor of 10, from 2 °C/hr to 20 °C/hr, on parameterization: | | | | |
| | 2b-1 | + 5.5 % | - 7.4 % | + 1 % |
| | 2b-4 | + 9.0 % | + 5.6 % | + 0.8 % |
| | 2b-7 | + 9.4 % | + 0.7 % | 1.1 % |

Because D_{MgVIII} values have not been experimentally determined, 2 °C/hr and 20 °C/hr cooling data parameterizations are restricted in this section to SrO, BaO, and CaO, assuming that CaO partitioning behavior will be identical for both thermal regimes. Since only three partition coefficients are used to fit three parameters, the resulting Onuma curves have no misfit. The calculated parameters are listed in Table A3.8, which indicates that the greatest influence the slightly higher partition coefficients of the 20 °C/hr cooling experiments have on crystal chemical model parameters is elevating the D_o value. This effect is modest: within 10% of the 2 °C/hr cooling values. Effects on the strain parameter E are non-systematically variable, and changes in r_o are minimal.

D vs. ionic radius plots of these data are shown in Figure A3.13. Bulk magnesium partition coefficients are plotted at the ionic radius of Mg in cubic coordination (0.89 Å) (Shannon, 1976) but were not part of the curve parameterizations.

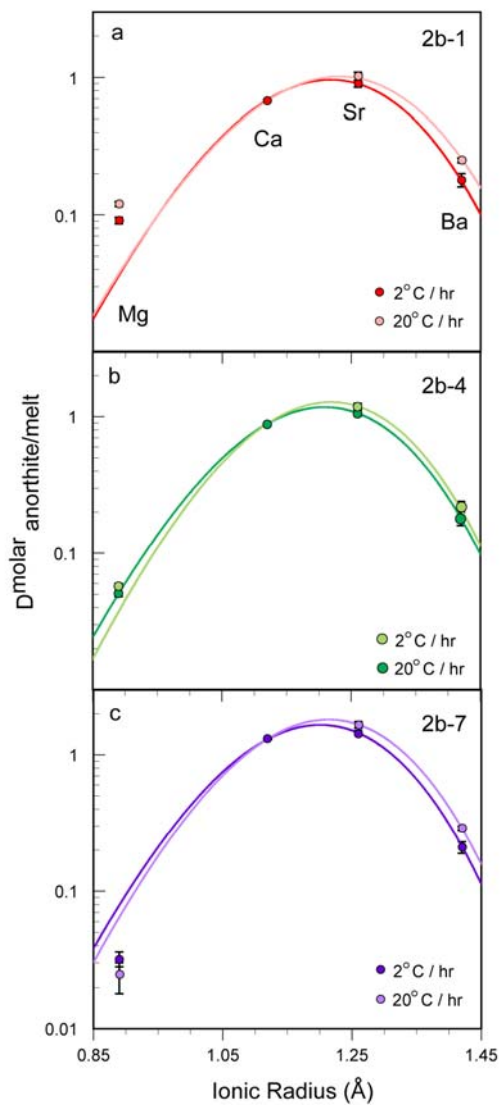


Figure A3.13. D vs. ionic radius curve parameterizations of Table A3.8 from 2 °C/hr and 20 °C/hr cooling data for compositions (a) 2b-1, (b) 2b-4, and (c) 2b-7. Partition coefficient 1 σ uncertainty is within symbol size except where shown.

A4 CAI COMPOSITION: DIVALENT ELEMENT PARTITIONING AND CATHODOLUMINESCENCE

A4.1 Anorthite and Melt compositions for Synthetic CAI Composition 224SAM

Anorthite-melt partitioning of divalent elements MgO, CaO, SrO, and BaO was also studied in the CMAST system based on the synthetic CAI-like composition 224 (Simon et al., 1994), which has been shown to readily crystallize anorthite under experimental conditions. Materials were prepared according to the procedures described in Miller et al. (2003) except that the starting material was also doped with 750 ppm Eu, which was present in concentrations just barely above detection limits. Since experiments were performed at ambient air oxygen fugacity, most (but not necessarily all) of the Eu would likely be trivalent and not relevant to divalent element partitioning systematics. Thus Eu contents of 224SAM21 phases were not analyzed.

Table A4.1. Glass and anorthite compositions for 224SAM run products analyzed by EMP. Glass uncertainty reported as standard error of the mean and anorthite error is 1 σ standard deviation.

| Wt. % | 224SAM1 | 224SAM21 | 224SAM21 |
|--------------------------------|----------------------|------------------|---------------------|
| | Fused Glass n = 5 | Glass n = 20 | Anorthite n = 20 |
| SiO ₂ | 44.6 (2) | 45.02 (5) | 43.3 (2) |
| TiO ₂ | 1.76 (6) | 2.01 (2) | 0.05 (3) |
| Al ₂ O ₃ | 20.05 (6) | 16.14 (2) | 35.8 (2) |
| Eu ₂ O ₃ | 0.09 (3) | na | na |
| MgO | 3.86 (3) | 4.760 (9) | 0.27 (4) |
| CaO | 28.03 (2) | 29.68 (3) | 19.9 (1) |
| SrO | 0.07 (1) | 0.07 (1) | 0.08 (3) |
| BaO | 1.35 (3) | 1.65 (3) | 0.36 (9) |
| Na ₂ O | <u>0.035 (4)</u> | <u>0.025 (2)</u> | <u>0.027 (9)</u> |
| | 99.78 | 99.36 | 99.79 |

na = not analyzed

Electron microprobe conditions and standards are the same as those presented in Section 2.2.4 for low (25 nA) beam current analyses. Compositions (wt. %) of the fused starting material (run 224SAM1) and coexisting anorthite and glass in the controlled cooling experiment 224SAM21 are given in Table A4.1. Table A6.1 lists run conditions for these experiments.

Table A4.2. Modeled divalent element partition coefficients for anorthite rims and coexisting CAI melt (CMAST), run 224SAM21, compared with data and parameterization for run 2b-2-2 (CMAS) of similar major element composition. D^{m}_{MgVIII} uncertainty assumed to be 10%; all other error (1 σ) given in parentheses and applies to the last digit shown. $\chi^2 = [(\ln D^{data} - \ln D^{model}) / \ln \sigma^{data}]^2$ for each parameterization.

| | D^{m}_{MgVIII} | D^{m}_{CaO} | D^{m}_{SrO} | D^{m}_{BaO} |
|------------|------------------|---------------|---------------|---------------|
| 224SAM21 | 0.013 (1) | 0.728 (4) | 1.05 (40) | 0.27 (7) |
| CMAS2b-2-2 | 0.008 (1) | 0.738 (4) | 0.92 (4) | 0.15 (2) |
| | D_o | E (GPa) | r_o (Å) | χ^2 |
| 224SAM21 | 1.13 | 121 (13) | 1.223 (4) | 2.79 |
| CMAS2b-2-2 | 1.04 | 134 (11) | 1.209 (2) | 6.21 |

Molar partition coefficients of divalent elements in 224SAM21 are tabulated in Table A4.2, with D^{m}_{MgVIII} for this composition estimated according to the site occupancy modeling of Section 2.3.3, assuming that several wt. % TiO₂ has little effect on the thermodynamics predicted by the Berman (1983) CMAS melt model and any reoptimization (chapter 3) thereof. Lattice strain parameterizations shown in Table A4.2 were calculated from the partitioning data shown (including D^{m}_{MgVIII}) and equation (2.1) of chapter 2. Results are compared to values obtained from partitioning observed in

CMAS2b-2, the composition of those studied in chapter 2 most like 224SAM. Since the compositions are not identical in major element contents, the observed variations in D_o , E , and r_o cannot be conclusively attributed to addition of TiO_2 . However, the similarities in lattice strain model parameters within analytical uncertainty do suggest that whatever effects TiO_2 may have are likely minor.

A4.2 Anorthite Zoning and Cathodoluminescence Intensity Imaging by SEM

The occurrence of bright cathodoluminescence (CL) with intensity variations resembling compositional zoning in crystals grown from 224SAM melt prompted a reconnaissance investigation into the feasibility of using CL as a quick method of identifying anorthite crystal heterogeneity. CL is known to be a common feature in volcanic and metamorphic feldspars (Gotze et al., 2000; Marshall, 1988), so greater understanding of CL mechanisms potentially provide further insight into crystal growth in natural systems.

Trace constituents may serve to activate, enhance, or quench mineral luminescence in response to electron beam interactions depending on their electronic structure, location in a mineral, and concentration (Marshall, 1988). Sources of CL in materials are difficult to isolate when abundances of activators can be well below detection limits of many *in situ* analytical techniques, and thus many CL phenomena remain poorly understood. However, this sensitivity to structural defects and low abundances of trace elements in crystals make CL a powerful tool in recognizing complex zonation patterns that offer unique records of magma chamber dynamics and

mixing inaccessible by other analytical methods (e.g., Slaby and Gotze, 2004; Stirling et al., 1999; Vanko and Laverne, 1998). Specific wavelengths of CL emissions have been attributed to the presence of specific cations and valence states, though observations here are restricted to intensity. The Caltech LEO 1550 VP FE-SEM currently does not have CL emission wavelength imaging capabilities, but some variations in CL intensity are detectable. Images in Figures A4.1 through A4.5 were obtained by removing the electron detector (EBSD) and observing light emitted in response to a 14-15 kV accelerating voltage with the variable pressure secondary electron detector (VPSE) signal.

Figure A4.1 (a) and (b) show that in addition to emitting striking CL intensity relative to the surrounding melt, anorthite crystals in sample 224SAM21 also contain internal light intensity variations. A 2-D polygonal point grid across a crystal containing an especially bright zone was analyzed for major and trace elements at low (25 nA) beam current on an electron microprobe, with the standards and operating conditions described in Section 2.2.4. Compositional maps (c) and (d) and the correlation plot Figure A4.2 (a) indicate that the region of elevated CL intensity corresponds to an increase in MgO content and decrease in Al₂O₃, suggesting the substitution mechanism,



where Ti⁴⁺ would also participate in place of Si⁴⁺.

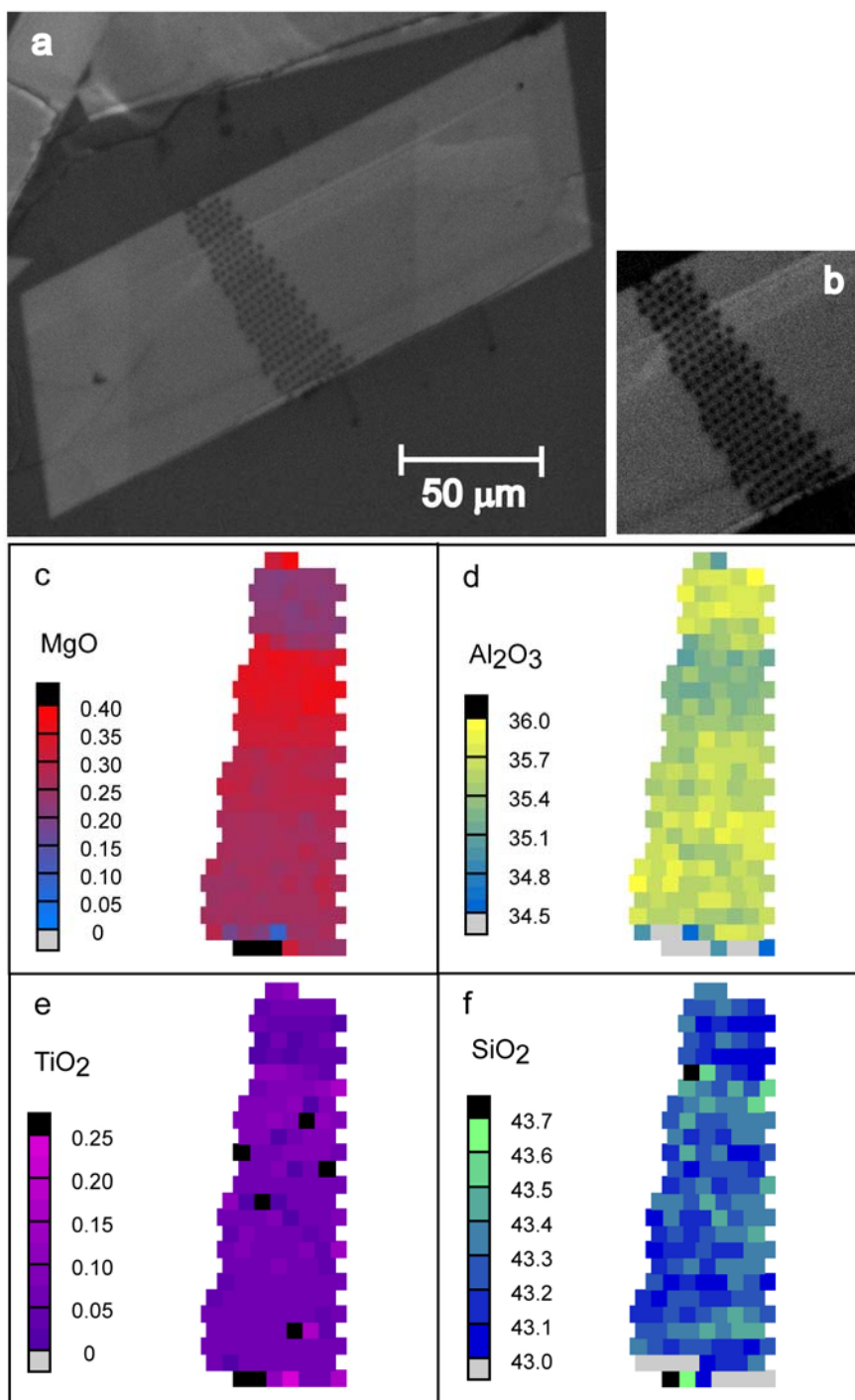


Figure A4.1. (a) SEM cathodoluminescence intensity variations in representative anorthite lath of 224SAM21. (b) Zoom in on band on greater CL intensity and EMP beam burn marks on carbon coat. (c) MgO content (wt. %) of 2-D polygonal grid represented by beam spots of (a) and (b). (d) Al₂O₃ (wt. %), (e) TiO₂ (wt. %), and (f) SiO₂ (wt. %).

Visual inspection of Figure A4.1 (e) and (f) suggests a faint elevation of both TiO_2 and SiO_2 in the region of the crystal corresponding to elevated Mg content. Increased TiO_2 as a function of MgO becomes more apparent in Figure A4.2 (c), though evidence of a SiO_2 -MgO correlation from the data shown in Figure A4.2 (b) is equivocal. Likewise, plots (d), (e), and (f) show little MgO dependence on Na_2O , CaO , or BaO in the anorthite crystal.

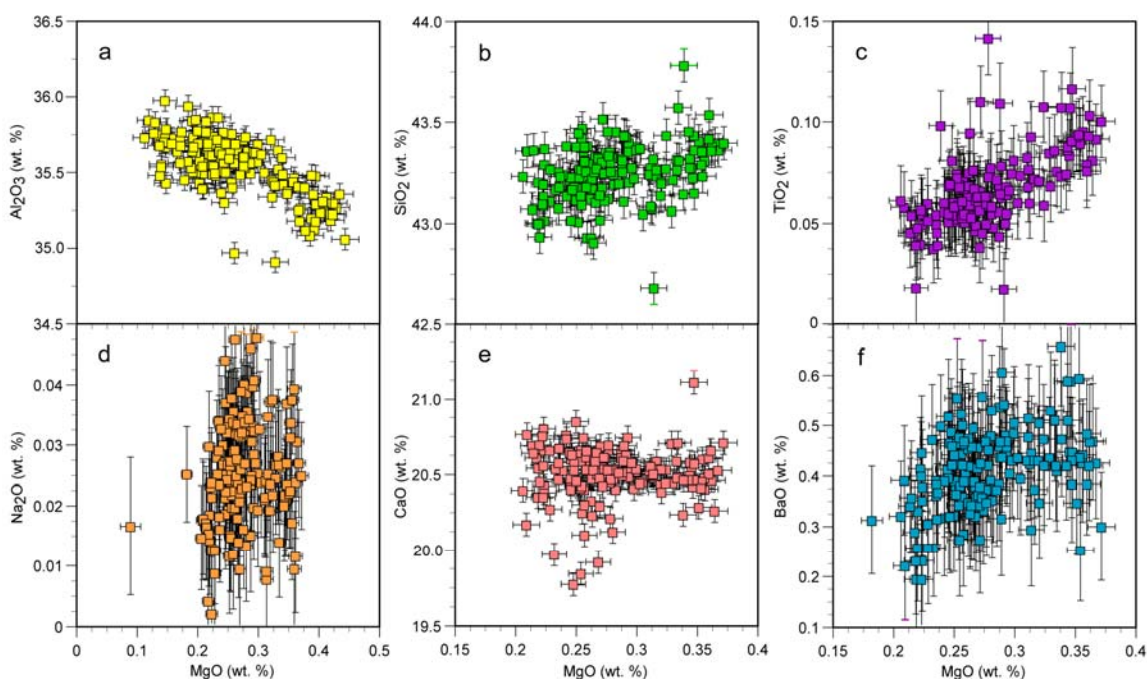


Figure A4.2. Anorthite lath of 224SAM21 correlation plots against MgO content (wt. %) for (a) Al_2O_3 , (b) SiO_2 , (c) TiO_2 , (d) Na_2O , (e) CaO , and (f) BaO . Analytical error for each analysis is 1σ .

Several controlled cooling experiments using major element compositions 224SAM and CMAS2-2 doped with different concentrations of trace and minor elements were conducted to further investigate sources of CL in synthetic anorthites and explore whether CL could be used as a zoning marker for divalent element heterogeneity in

studies of anorthite like that discussed in chapter 2. Doping concentrations for each run are given in Table A4.3, though sample products were only inspected visually by SEM and no concentrations have been confirmed by quantitative analysis.

Synthetic anorthites grown from CMAS melts doped with Sr and Ba emit no cathodoluminescence, and this is true for both CMAS1 samples (Figure A4.5abc) as well as CMAS2 compositions (not shown). This narrows the potential source of CL emissions from the 224SAM composition to the presence of Ti^{4+} and/or Eu^{3+} under the highly oxidizing (air) atmospheric conditions of this study or possible structural defects associated with their substitution into the crystal.

Table A4.3. Summary table of cathodoluminescence reconnaissance study controlled cooling experiments, with run labels indicating major element starting material compositions. Approximate doping concentrations of trace elements and whether or not anorthite crystals displayed any CL intensity are also listed.

| Run label | Trace/minor element doping concentrations | CL? |
|------------|--|-----|
| 224SAM-Eu | ~2 wt. % TiO_2 , 750 ppm Eu, 750 ppm Sr, 1500 ppm Ba | Yes |
| CMAS2-2-Ti | 1000 ppm Ti | No |
| CMAS2-2-Eu | 750 ppm Eu | No |
| CMAS2-2-Mn | 1000 ppm Mn, 1000 ppm Sr, 1500 ppm Ba | No |
| CMAS2-2-Ge | ~2 wt. % GeO_2 | No |

Previous observations of CL in synthetic anorthites grown from composition 224 melts have found that luminescence intensity correlates with decreases in MgO and Na_2O abundance, with no apparent relationship to TiO_2 content (Steele et al., 1997). Small differences in anorthite Na_2O content in CMAS1 run products ($An_{99.7}$, $An_{95.8}$, $An_{95.8}$ for runs 1-1-2, 1-3-9, and 1-6-8) do not appear to generate any CL variations, as shown in

Figure A4.5, though the CMAS1 abundances span the range of sodium contamination reported in Steele et al. (1997).

Steele et al. (1997) also inspected run products ES55 and ES60, which had oxygen fugacities of C/CO ($\sim 10^{-19}$) and air, respectively, from Peters et al. (1995) with identical results, suggesting the source of CL in those samples was unrelated to any particular cation valence state. They found these observations consistent with those of an Allende anorthite study by Hutcheon et al. (1978), and Vanko and Laverne (1998) also noticed lower CL intensity with higher MgO contents in MOR plagioclases. These works lie in stark contrast to the results of this study, as documented in Figures A4.1 and A4.2, which show CL intensity increasing with MgO and TiO₂ content.

The primary difference between the Steele et al. (1997)/Peters et al. (1995) compositions and that of this study is that 224SAM was doped with ~ 750 ppm Eu. Eu in open air experiments is likely to be mostly trivalent and assuming $D_{Eu} \sim 0.1$ (Bindeman et al., 1998), Eu contents of anorthite here were likely on the order of 50-100 ppm. Distinctive CL in synthetic anorthite doped with ~ 200 ppmw Eu²⁺ has been observed (Mariano and Ring, 1975), but doping the initial melt composition CMAS2-2 with ~ 750 ppm Eu³⁺ produced no CL in anorthite (Figure A4.3a). CMAS2-2 was chosen for doping because it is the closest CMAS analogue of composition 224 available from the CMAS1 and CMAS2 materials. Although some reports attribute an intense blue CL emission to the presence of Ti⁴⁺ (e.g. Mariano et al., 1973; Marshall, 1988; Stirling et al., 1999), spiking an aliquot of CMAS2-2 with 1000 ppm Ti did not result in growing luminescent anorthites, at least within the ability of the SEM to detect CL (see Figure A4.3b). The concentration of Ti in CMAS2-2-Ti anorthite may have been too low to produce

detectable CL, since D_{Ti} anorthite/melt values (Peters et al., 1995) suggest that these anorthites likely contained ~50 ppm Ti and previous work has found that 0.05–0.1 wt. % TiO_2 was necessary to produce CL in feldspars (Mariano et al., 1973).

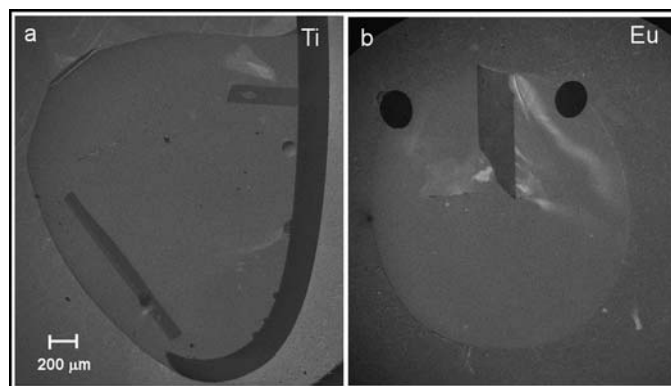


Figure A4.3. SEM CL intensity images of (a) CMAS2-2-Ti, and (b) CMAS2-2-Eu. Bright wisps are likely surface contamination features. Anorthite crystals are dark gray and semi-rectangular, while Pt wire appears as black hook (a) and ovals (b).

Since manganese is well known for generating a distinctive green/yellow CL in plagioclase (e.g. Geake et al., 1973; Gotze et al., 2000; Mariano et al., 1973; Slaby and Gotze, 2004; Stirling et al., 1999; Telfer and Walker, 1978), another aliquot of CMAS2-2 was spiked with 1000 ppm Mn and run under reducing Ar gas flow, though exact f_{O_2} was not monitored. Although Mn^{2+} CL activation occurs at concentrations below 20 ppm (Gotze, 1998; Gotze et al., 2000), no CL was detected in anorthites of run CMAS2-2-Mn (Figure A4.4b).

Some workers have speculated that a wide blue band of CL in feldspars, and common to silicates in general, results from an intrinsic luminescence produced by structural defects (Geake et al., 1973; Marshall, 1988). Pack and Palme (2003) observed ubiquitous CL in synthetic forsterites grown from both undoped CMAS and CMAS+Ti compositions, with intensity correlating with increased TiO_2 in the Ti-bearing systems

and Al_2O_3 content of forsterite in the CMAS compositions. An EPR (electron paramagnetic resonance) investigation of feldspars observed that high anorthite content seems to prevent formation of Al-O^- -Al defect centers (Speit and Lehmann, 1982), which are attributed to the 450-480 nm CL emission band (Gotze et al., 2000). The fact that anorthites of this study have a pure end-member composition and, except for 224SAM anorthites, show no CL would be consistent with a lack of CL-producing Al^{3+} defects.

“ $\text{Si-O}^- \dots \text{M}^{2+}$ ” defects associated with a 500–510 nm band could also be a candidate for producing the 224SAM CL, since this defect is characterized by an oxygen hole next to a divalent ion in an adjacent tetrahedral site (Speit and Lehmann, 1982) and CL in this study is correlated with Mg content. The bulk of Mg in plagioclase likely resides on the tetrahedral site (Longhi et al., 1976; Miller et al., 2006; Peters et al., 1995), though this cannot be the primary source of CL in these experiments when tetrahedral Mg occurs in all the anorthites of the 224SAM, CMAS1, CMAS2, and CMAS2b compositions but only 224SAM produces CL. CMAS2 melt compositions were also spiked with ~500 ppm Be, another divalent element populating anorthite T sites, and those anorthites exhibited no CL.

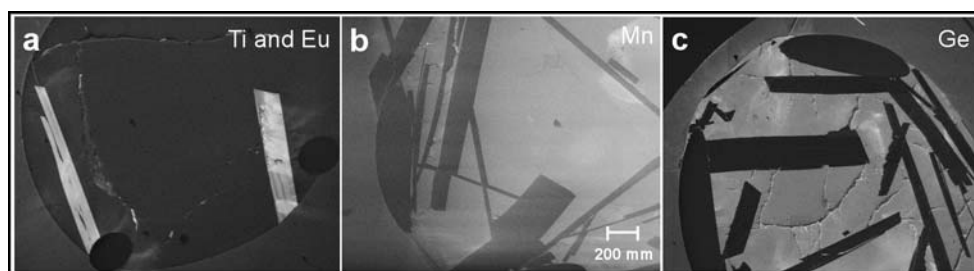


Figure A4.4. SEM-CL images of (a) striking intensity of anorthite crystals from 224SAM-Eu-1, (b) no CL intensity in CMAS2-2-Mn, and (c) no CL intensity in the crystals of CMAS2-2-Ge.

The hypothesis that Ti^{4+} might enhance defect-related luminescence was tested by doping CMAS2-2 with an amount of GeO_2 comparable to the TiO_2 content of 224SAM (~2 wt. %). Since Ge^{4+} has an ionic radius similar to that of Ti^{4+} (0.39 and 0.42 Å, respectively) and the same valence state, it seemed reasonable that the partition coefficients and structural positions of these ions would be similar in anorthite. As seen in Figure A4.4c, the Ge-doped crystals emit no CL. Furthermore, excess silica in the anorthite structure also appears to have no role in generating CL emissions (Figure A4.5). The source(s) of CL in the 224SAM anorthite crystals remain unknown.

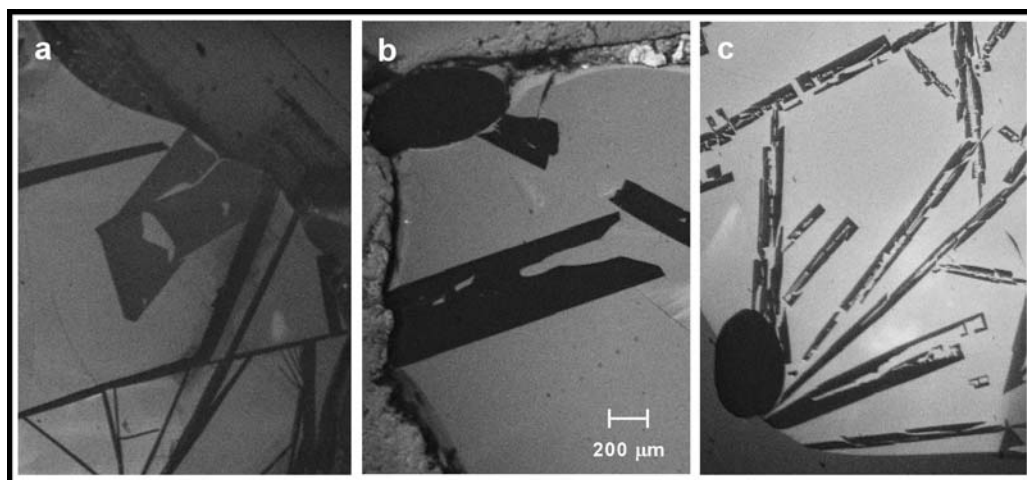


Figure A4.5. SEM CL intensity images comparing the effect varying extents of structural excess silica in anorthite on cathodoluminescence intensity. (a) CMAS1-1-6, (b) CMAS1-3-9, and (c) CMAS1-6-8.

A5 ANORTHITE-MELT PARTITIONING OVER A RANGE (40-60 WT.%) OF MELT SILICA CONTENT

A5.1 Composition Selection of Variable SiO₂ Melts (CMAS1 Suite) for Partitioning Experiments

A study of anorthite-melt partitioning with six melt compositions (CMAS1) varying in SiO₂ content was attempted, since magma in natural systems generally evolves from mafic to more felsic compositions. However, this section demonstrates that melt influence on partitioning could not be isolated in these experiments due to resulting covariance in crystal and melt chemistry. As discussed in Section 2.2.1, anorthite crystals synthesized at low pressure can incorporate up to 15 wt. % excess silica component into their structures (Bruno and Facchinelli, 1974) depending on the silica content of the coexisting melt and crystal growth rate (Beaty and Albee, 1980). This proved true for the anorthites grown from the CMAS1 compositions.

Figure A5.1 shows the locations of the starting compositions for the six CMAS1 melts projected onto the CAS ternary. Although these compositions all contain ~1 wt. % MgO, a CAS diagram is a reasonably accurate simplification of the composition space. Materials were prepared according to the procedures outlined in Section 2.2.4 except that the doping concentrations were 1500 ppm Ba and 1000 ppm Sr. Isothermal experiments were conducted to constrain the liquidus and confirmed all were at or near the 1400 °C anorthite liquidus as predicted by the Berman (1983) CMAS thermodynamic melt model. Liquidus temperatures for the six CMAS1 compositions are displayed in Table A5.1.

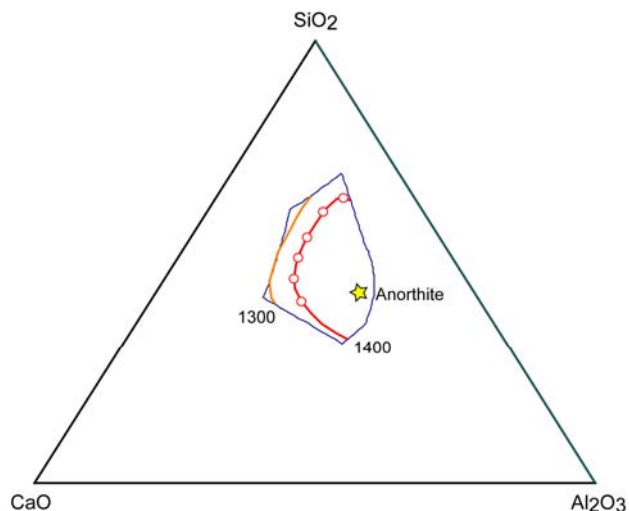


Figure A5.1. CMAS1 melt compositions shown in red circles on the 1400 °C liquidus isotherm within the anorthite stability field (outlined in blue) projected onto the CAS ternary (wt. %). The 1300 °C liquidus isotherm is shown in orange.

A5.2 CMAS1 Anorthite and Melt Composition Data and Evidence of SiO₂ and Na₂O Solid Solution

Compositions of phases present in the CMAS1 experimental charges (run conditions listed in Table A6.1) were measured with the Caltech 733 electron microprobe using analytical conditions and standards described in Section A1.3 and Section 2.2.4, respectively. Table A5.1 lists the starting material contents, which, for the purposes of calculating partition coefficients for these experiments, are assumed to be the melt compositions from which the centers of anorthite crystals initially grew.

Anorthite and coexisting glass contents of select dynamic crystallization experiments of each melt composition are listed in Table A5.2 and Table A5.3. The dependence of excess silica component incorporation into the anorthite structure on melt SiO₂ content is shown in Figure A5.2. When melt compositions contain less than 50

wt. % SiO₂ the excess []Si₄O₈ component varies little within analytical uncertainty, but at higher melt silica contents silica solid solution increases significantly.

Table A5.1. Initial melt compositions (wt. %) determined by EMP analysis of glass points. Uncertainty reported as standard error of the mean in parentheses and applies to the last digit shown. Liquidus uncertainties are ± 5 °C.

| | 1-1-1 n = 5 | 1-2-1 n = 5 | 1-3-1 n = 5 | 1-4-1 n = 5 | 1-5-1 n = 5 | 1-6-1 n = 5 |
|--------------------------------|-----------------|-----------------|-----------------|-----------------|-----------------|-----------------|
| Liquidus (°C) | 1393 | 1395 | 1407 | 1407 | 1407 | 1417 |
| SiO ₂ | 39.73 (6) | 44.5 (1) | 49.72 (6) | 53.59 (7) | 59.2 (2) | 62.1 (3) |
| Al ₂ O ₃ | 27.16 (9) | 23.39 (9) | 21.12 (4) | 20.96 (4) | 21.1 (1) | 22.6 (1) |
| MgO | 0.94 (1) | 0.92 (1) | 0.92 (1) | 0.94 (1) | 0.92 (1) | 0.96 (1) |
| CaO | 30.66 (5) | 29.76 (5) | 26.26 (5) | 23.06 (4) | 17.12 (6) | 12.63 (7) |
| SrO | 0.12 (1) | 0.14 (1) | 0.11 (3) | 0.12 (1) | 0.08 (2) | 0.12 (1) |
| BaO | 0.19 (2) | 0.17 (2) | 0.19 (3) | 0.16 (1) | 0.21 (3) | 0.22 (2) |
| Na ₂ O | <u>0.96 (1)</u> | <u>1.06 (1)</u> | <u>1.25 (3)</u> | <u>1.38 (1)</u> | <u>1.72 (1)</u> | <u>1.64 (2)</u> |
| | 99.81 | 99.99 | 99.59 | 102.2 | 100.33 | 100.24 |

Table A5.2. CMAS1 anorthite compositions (wt. %) determined by EMP analyses of random points in crystal centers. 1 σ error parentheses apply to the last digit shown.

| | 1-1-2 n = 10 MgO, SrO, BaO: n = 30 | 1-2-2 n = 10 MgO, SrO, BaO: n = 30 | 1-3-9 n = 10 MgO, SrO, BaO: n = 30 | 1-4-11 n = 10 MgO, SrO, BaO: n = 30 | 1-5-9 n = 10 MgO, SrO, BaO: n = 30 | 1-6-8 n = 10 MgO, SrO, BaO: n = 30 |
|--------------------------------|---|---|---|--|---|---|
| SiO ₂ | 42.8 (4) | 43.4 (4) | 44.7 (2) | 45.6 (5) | 47.1 (6) | 48.2 (7) |
| Al ₂ O ₃ | 36.5 (3) | 36.3 (4) | 35.3 (3) | 34.8 (5) | 33.0 (5) | 33.1 (4) |
| MgO | 0.009 (9) | 0.019 (5) | 0.083 (7) | 0.088 (7) | 0.08 (1) | 0.058 (9) |
| CaO | 20.3 (2) | 20.14 (9) | 19.4 (1) | 18.89 (9) | 18.4 (1) | 18.1 (3) |
| SrO | 0.11 (1) | 0.114 (6) | 0.118 (6) | 0.100 (6) | 0.101 (6) | 0.107 (6) |
| BaO | 0.04 (1) | 0.03 (1) | 0.027 (9) | 0.020 (7) | 0.015 (9) | 0.016 (9) |
| Na ₂ O | <u>0.03 (2)</u> | <u>0.19 (3)</u> | <u>0.46 (5)</u> | <u>0.51 (2)</u> | <u>0.50 (3)</u> | <u>0.43 (3)</u> |
| | 99.78 | 100.19 | 100.09 | 100.01 | 99.20 | 100.01 |

Table A5.3. CMAS1 glass compositions (wt. %) determined by EMP analysis of random points throughout the sample charge. 1σ error parentheses apply to the last digit shown.

| | 1-1-2 n = 10 | 1-2-2 n = 10 | 1-3-9 n = 10 | 1-4-11 n = 10 | 1-5-9 n = 10 | 1-6-8 n = 10 |
|--------------------------------|-----------------|-----------------|-----------------|------------------|-----------------|-----------------|
| SiO ₂ | 38.2 (4.4) | 44.7 (6) | 51.0 (2) | 55.3 (7) | 62.0 (3) | 66.0 (2.2) |
| Al ₂ O ₃ | 25.1 (2.3) | 18.9 (3) | 18.3 (1) | 18.6 (4) | 18.4 (3) | 19.6 (1.4) |
| MgO | 1.23 (8) | 1.25 (2) | 1.12 (2) | 1.13 (3) | 1.12 (2) | 1.4 (1) |
| CaO | 34.8 (2.0) | 34.1 (2) | 28.6 (1) | 24.08 (1) | 17.3 (2) | 11.4 (8) |
| SrO | 0.11 (5) | 0.12 (4) | 0.12 (3) | 0.13 (3) | 0.13 (4) | 0.12 (2) |
| BaO | 0.24 (7) | 0.21 (8) | 0.19 (6) | 0.20 (7) | 0.19 (8) | 0.33 (6) |
| Na ₂ O | <u>0.25 (2)</u> | <u>0.34 (9)</u> | <u>0.43 (2)</u> | <u>0.48 (3)</u> | <u>0.53 (2)</u> | <u>0.63 (5)</u> |
| | 99.93 | 99.62 | 99.76 | 99.92 | 99.67 | 99.48 |

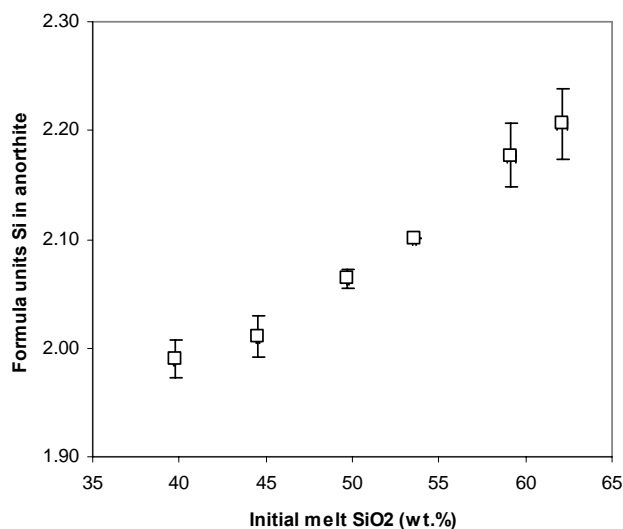


Figure A5.2. Incorporation of excess silica component []Si₄O₈ into anorthite structure reported as increase in formula units of Si measured in CMAS1 suite anorthites as a function of initial melt SiO₂ content. Error bars represent 1σ uncertainty in anorthite composition analysis. Melt analysis error is within symbol size.

Although no Na₂O was included in the starting material, some run products of Pt wire experiments that remained in the furnace without any gas flow for durations longer than 15 minutes experienced over 1.5 wt. % sodium contamination (Figure A5.3). Since maintaining uniform crystal chemistry in anorthites from all six CMAS1 compositions

was necessary to isolate the effect of melt composition on partitioning, having varying levels of sodium contamination in the furnace proved problematic. Anorthite data in Table A5.2 indicate that the crystals on average contain between 0.2 % and 5 % of an albitic component. Neutralizing this effect by subjecting experimental charges for all six compositions to the same furnace conditions by running them concurrently was not an option, as the differences in liquidus temperatures for the starting materials was great enough to require slightly different controlled cooling programs in order to grow crystals. Use of Pt capsules and flows of various gases (Ar, CO, and compressed air) all reduced sodium contamination to within or just above EMP detection limits, though the anorthite and glass data for the CMAS1 compositions were all collected on samples run in stagnant air prior to this discovery. Subsequent experiments involving the CMAS2 and CMAS2b compositions all used some form of gas flow to minimize sodium partial pressure in the furnace during runs.

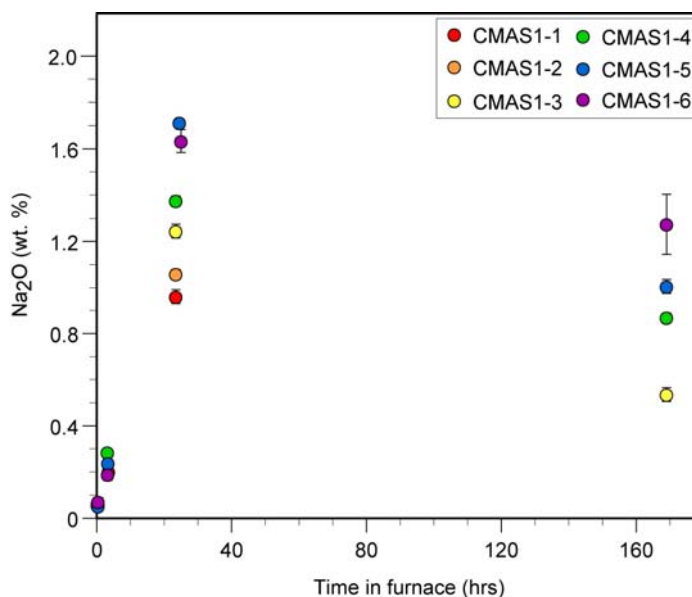


Figure A5.3. Glass Na₂O (wt. %) content change as a function of time in furnace.

Estimates of Mg distribution between IV- and VIII-fold coordinated sites in anorthite for partition coefficient modeling followed the method described in Section 2.3.3. Compositional data for CMAS1 are less precise than those of CMAS2b (chapter 2) due to use of a lower beam current during analysis and only collecting data points from crystal interiors, which may be more heterogeneous than crystal rims. Both these factors likely contribute to the large uncertainties shown in Figure A5.3. Although the equations relating Mg site occupancy to melt chemistry in Section 2.3.3 do not explicitly account for the presence of excess silica in the anorthite phase, the Berman (1983) melt model may be assumed to have incorporated the effects of this solid solution on activity coefficients because it was calibrated and tested using liquidus data from anorthite-melt experiments throughout the anorthite stability field, which includes high silica melts (>50 wt. % SiO₂). This study and others (e.g., Bruno and Facchinelli, 1974; Ito, 1976; Longhi and Hays, 1979; Murakami et al., 1992) have shown such melts produce anorthite with an excess silica component likely not recognized without careful quantitative compositional analysis of crystals larger than those generated in near-liquidus experiments. The D^m_{MgO} -melt major activity product relationship used to predict D^m_{MgVIII} in CMAS1 compositions is plotted in Figure A5.4.

CMAS1 anorthite-melt molar partition coefficients for major and trace elements are listed in Table A5.4. D values are calculated using the initial starting compositions of Table A5.1 and anorthite center point averages reported in Table A5.2. $D^m_{MgOVIII}$ and D^m_{CaO} both increase as the melts become progressively siliceous, but the errors associated with the SrO partitioning data are too large to identify a similar trend for that element.

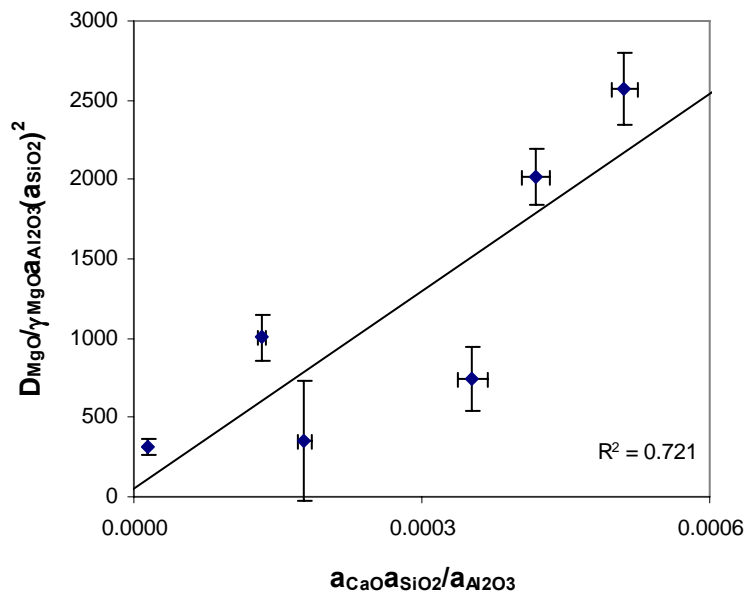


Figure A5.4. Relationship observed D_{MgO}^m and melt activity products (from Berman (1983) CMAS melt model) expected for Mg^{2+} partitioning onto IV- and VIII-fold coordination sites of anorthite crystal lattice. 1σ error bars for activity products are propagations of activity uncertainties due to compositional uncertainty. No estimate is made of systematic errors inherent in the activity model.

Table A5.4. Anorthite/melt partitioning in CMAS1 compositions at ~ 1400 °C. D_{MgO}^{m} values are calculated following the method outlined in chapter 2, using the linear relationship between D_{MgO}^m and major element activity products to predict Mg site occupancy in anorthite. Uncertainties are propagations of the standard error of the mean and 1σ analytical errors for the glass and anorthite phases, respectively, and are given in parentheses, referring to the final digit reported for each value.

| | $D_{SiO_2}^m$ | $D_{Al_2O_3}^m$ | D_{MgO}^m | D_{MgO}^{mVIII} | D_{CaO}^m | D_{SrO}^m | D_{BaO}^m |
|--------|---------------|-----------------|-------------|-------------------|-------------|-------------|-------------|
| 1-1-2 | 1.14 (1) | 1.42 (1) | 0.01 (1) | 0.0015 | 0.700 (5) | 0.97 (9) | 0.22 (6) |
| 1-2-2 | 1.04 (1) | 1.66 (2) | 0.022 (5) | 0.0017 | 0.724 (3) | 0.87 (7) | 0.20 (7) |
| 1-3-9 | 0.961 (4) | 1.79 (2) | 0.096 (8) | 0.0021 | 0.792 (5) | 1.2 (3) | 0.15 (6) |
| 1-4-11 | 0.914 (1) | 1.78 (1) | 0.101 (8) | 0.0029 | 0.881 (1) | 0.89 (9) | 0.13 (5) |
| 1-5-9 | 0.85 (1) | 1.68 (3) | 0.09 (1) | 0.0053 | 1.153 (9) | 1.4 (3) | 0.08 (5) |
| 1-6-8 | 0.82 (1) | 1.54 (2) | 0.06 (1) | 0.0115 | 1.51 (2) | 0.9 (1) | 0.08 (4) |

Interestingly, D_{BaO}^m exhibits partitioning behavior opposite that of D_{MgO}^{mVIII} and D_{CaO}^m . It is unclear whether this difference results from the structural variations in

anorthite due to excess silica that promote incorporation of Ba or possible kinetic effects of crystal growth from increasingly viscous melts that could allow large Ba melt concentration gradients to develop around the crystals. Anorthite clearly grows differently from highly siliceous melts than in more mafic compositions under the same thermal regime, as indicated by the visible changes in crystal morphology shown in Figure A4.5, where crystal of experiment 1-6-8 (c) are less well formed than in 1-1-2 (a) or 1-3-9 (b).

A5.3 Lattice Strain Parameterizations of CMAS1 Divalent Element Partitioning Data

Lattice strain parameters were calculated from CMAS1 divalent element partitioning data according to the methods described in Section A4.1 and are given in Table A5.5. Goodness of fit, χ^2 , is relatively low compared to values calculated for parameterizations in chapter 2 because the analytical precision of the CMAS1 data is much lower. If changes in crystal structure are dominating the Ba partitioning behavior observed and the activity coefficient of Ba in the solid varies little, the strain parameter (E) calculated from the Ba data suggests that the anorthite structure around the large M site may become more rigid as silica content increases in the anorthite and/or melt. Parameterizations of the ideal ionic radius of the crystal site (r_o) for these compositions show no systematic variations. D_o , however, increases with increasing melt silica content in a manner primarily dictated by the partitioning systematics of $D^{MgO/VIII}$ and D^{CaO} . Parameterized curves (D vs. ionic radius) for CMAS1 are plotted in Figure A5.5 with the partitioning data of Table A5.5.

Table A5.5. Lattice strain model parameterization after Blundy and Wood (1994) for CMAS1 divalent element (Mg, Ca, Sr, Ba) partitioning data. Parameterization uses calculated $D^m MgO_{VIII}$ shown in Table A5.4 and assumes an uncertainty of 10% relative for those values. $\chi^2 = [(\ln D^{data} - \ln D^{model}) / \ln \sigma^{data}]^2$ for each parameterization.

| | D_o | E (GPa) | r_o (Å) | χ^2 |
|--------|-------|-----------|-----------|----------|
| 1-1-2 | 1.10 | 170 (20) | 1.213 (2) | 14.2 |
| 1-2-2 | 1.07 | 180 (20) | 1.203 (1) | 14.5 |
| 1-3-9 | 1.36 | 210 (20) | 1.212 (3) | 3.7 |
| 1-4-11 | 1.24 | 210 (20) | 1.192 (1) | 8.0 |
| 1-5-9 | 1.79 | 220 (20) | 1.200 (4) | 0.3 |
| 1-6-8 | 1.79 | 240 (20) | 1.169 (2) | 2.4 |

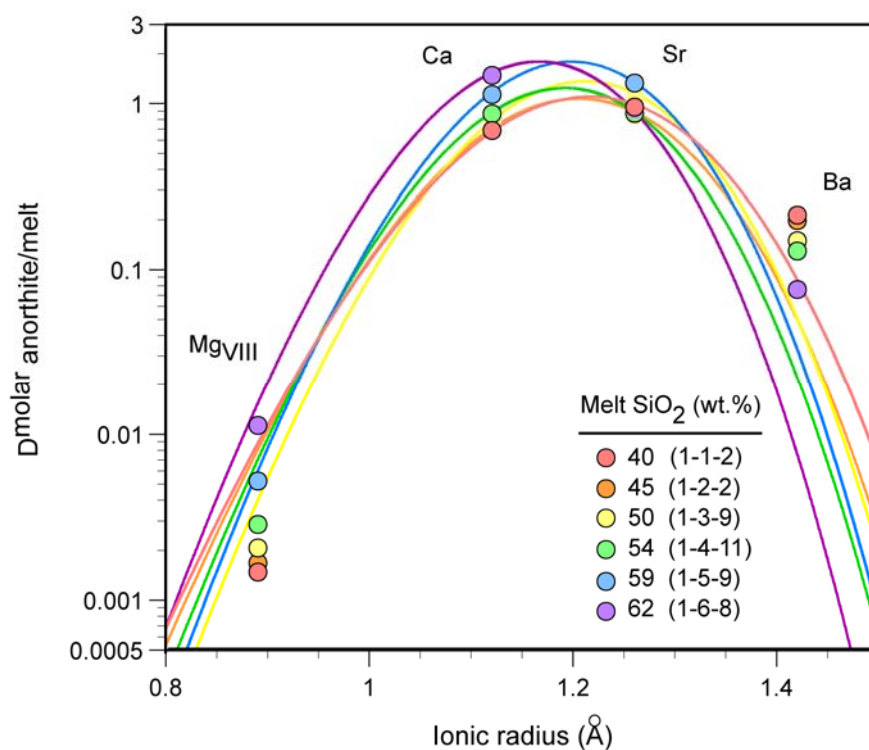


Figure A5.5. Onuma diagram of lattice strain parameterizations listed in Table A5.5 for divalent element (Mg, Ca, Sr, Ba) partitioning data of the CMAS1 melt compositions. Error bars on partition coefficients are omitted for clarity.

A6. THESIS RUN TABLE

Table A6.1. Run thermal histories of samples discussed in text. Temperature uncertainty = ± 5 °C. Air = compressed air flow from building. None = stagnant ambient air. CO = carbon monoxide. AG1 = Alphagaz1.

| | Gas Flow | Initial Temp | Initial Hold (hrs) | Cooling (°C/hr) | Intermediate Temp | Intermediate Hold (hrs) | Cooling (°C/hr) | Final Temp | Final Hold (hrs) |
|---|----------|--------------|--------------------|-----------------|-------------------|-------------------------|-----------------|------------|------------------|
| <u>CMAS2 suite (~1500 ppm Ba spike) dynamic crystallization experiments</u> | | | | | | | | | |
| 2-1-6 | Air | 1425 | 2 | 2 | 1380 | 24 | 2 | 1330 | 25 |
| 2-2-6 | Air | 1425 | 2 | 2 | 1380 | 24 | 2 | 1330 | 25 |
| 2-3-6 | Air | 1425 | 2 | 2 | 1380 | 24 | 2 | 1330 | 25 |
| 2-4-9 | Air | 1435 | 2 | 2 | 1400 | 24 | 2 | 1330 | 38 |
| 2-5-9 | Air | 1435 | 2 | 2 | 1400 | 24 | 2 | 1330 | 38 |
| 2-6-8 | Air | 1435 | 2 | 2 | 1400 | 24 | 2 | 1330 | 38 |
| 2-7-7 | Air | 1435 | 2 | 2 | 1400 | 24 | 2 | 1330 | 38 |
| <u>CMAS2b suite (~4500 ppm Ba spike) starting compositions</u> | | | | | | | | | |
| 2b-1-1 | Air | 1430 | 1 | - | - | - | - | - | - |
| 2b-2-1 | Air | 1430 | 1 | - | - | - | - | - | - |
| 2b-3-1 | Air | 1430 | 1 | - | - | - | - | - | - |
| 2b-4-1 | Air | 1430 | 1 | - | - | - | - | - | - |
| 2b-5-1 | Air | 1430 | 1 | - | - | - | - | - | - |
| 2b-6-1 | Air | 1430 | 1 | - | - | - | - | - | - |
| <u>CMAS2b suite dynamic crystallization experiments</u> | | | | | | | | | |
| 2b-1-2 | Air | 1415 | 1 | 2 | 1380 | 24 | 2 | 1330 | 28 |
| 2b-2-2 | Air | 1415 | 1 | 2 | 1380 | 24 | 2 | 1330 | 28 |
| 2b-3-2 | Air | 1415 | 1 | 2 | 1380 | 24 | 2 | 1330 | 28 |
| 2b-4-2 | Air | 1415 | 1 | 2 | 1380 | 24 | 2 | 1330 | 28 |
| 2b-5-2 | Air | 1415 | 1 | 2 | 1380 | 24 | 2 | 1330 | 28 |
| 2b-6-2 | Air | 1415 | 1 | 2 | 1380 | 24 | 2 | 1330 | 28 |
| 2b-7-2 | Air | 1415 | 1 | 2 | 1380 | 24 | 2 | 1330 | 28 |
| <u>Samples quenched at intermediate time points during controlled cooling thermal history</u> | | | | | | | | | |
| 2b-1-3 | Air | 1415 | 1 | 2 | 1380 | - | - | - | - |
| 2b-1-4 | Air | 1415 | 1 | 2 | 1380 | 24 | - | - | - |
| 2b-1-5 | Air | 1415 | 1 | 2 | 1380 | 24 | 2 | 1330 | - |
| 2b-4-3 | Air | 1415 | 1 | 2 | 1380 | - | - | - | - |
| 2b-4-4 | Air | 1415 | 1 | 2 | 1380 | 24 | - | - | - |
| 2b-4-5 | Air | 1415 | 1 | 2 | 1380 | 24 | 2 | 1330 | - |
| 2b-7-3 | Air | 1415 | 1 | 2 | 1380 | - | - | - | - |
| 2b-7-4 | Air | 1415 | 1 | 2 | 1380 | 24 | - | - | - |
| 2b-7-5 | Air | 1415 | 1 | 2 | 1380 | 24 | 2 | 1330 | - |

| | Gas Flow | Initial Temp | Initial Hold (hrs) | Cooling (°C/hr) | Intermediate Temp | Intermediate Hold (hrs) | Cooling (°C/hr) | Final Temp | Final Hold (hrs) |
|--|----------|--------------|--------------------|-----------------|-------------------|-------------------------|-----------------|------------|------------------|
| <u>Rapid cooling experiments</u> | | | | | | | | | |
| 2b-1-7 | Air | 1405 | 1 | 20 | - | - | - | 1330 | - |
| 2b-4-7 | Air | 1405 | 1 | 20 | - | - | - | 1330 | - |
| 2b-7-9 | Air | 1420 | 1 | 20 | - | - | - | 1330 | - |
| <u>CAI (CMAS_{Ti})</u> | | | | | | | | | |
| 224SAM1 | None | 1375 | 4 | - | - | - | - | - | - |
| 224SAM21 | Air | 1385 | 2 | 2 | 1345 | 24 | 2 | 1285 | 86 |
| <u>CMAS1 (SiO₂ ranging from ~40-60 wt. %) starting compositions</u> | | | | | | | | | |
| 1-1-1 | None | 1450 | 1 | 1000 | - | - | - | 1400 | 22 |
| 1-2-1 | None | 1450 | 1 | 1000 | - | - | - | 1400 | 22 |
| 1-3-1 | None | 1450 | 1 | 1000 | - | - | - | 1400 | 22 |
| 1-4-1 | None | 1450 | 1 | 1000 | - | - | - | 1400 | 22 |
| 1-5-1 | None | 1450 | 1 | 1000 | - | - | - | 1400 | 22 |
| 1-6-1 | None | 1450 | 1 | 1000 | - | - | - | 1400 | 22 |
| <u>CMAS1 dynamic crystallization experiments</u> | | | | | | | | | |
| 1-1-2 | None | 1415 | 2 | 2 | 1370 | 24 | 2 | 1320 | 90 |
| 1-2-2 | None | 1415 | 2 | 2 | 1370 | 24 | 2 | 1320 | 90 |
| 1-3-9 | None | 1430 | 2 | 2 | 1385 | 24 | 2 | 1325 | 24 |
| 1-4-11 | None | 1425 | 2 | 2 | 1385 | 24 | 2 | 1330 | 16 |
| 1-5-9 | None | 1440 | 2 | 2 | 1400 | 24 | 2 | 1330 | 26 |
| 1-6-8 | None | 1440 | 2 | 2 | 1400 | 24 | 2 | 1330 | 26 |
| <u>Pb and Bi volatility tests</u> | | | | | | | | | |
| 1-1-7 | None | 1415 | 2.0 | 2 | 1375 | 24 | 2 | 1325 | 13 |
| 1-1-8 | None | 1415 | 0.25 | - | - | - | - | - | - |
| 1-1-10 | CO | 1410 | 2.0 | 2 | - | - | - | 1360 | 21 |
| <u>Additional Na contamination tests</u> | | | | | | | | | |
| 1-1-9 | None | 1445 | 0.25 | - | - | - | - | - | - |
| 1-2-5 | None | 1445 | 0.25 | - | - | - | - | - | - |
| 1-3-2 | None | 1415 | 2 | 2 | 1370 | 24 | 2 | 1320 | 90 |
| 1-3-11 | None | 1445 | 0.25 | - | - | - | - | - | - |
| 1-3-2 | None | 1415 | 2 | 2 | 1370 | 24 | 2 | 1320 | 90 |
| 1-4-5 | None | 1415 | 3 | - | - | - | - | - | - |
| 1-4-10 | None | 1445 | 0.2 | - | - | - | - | - | - |
| 1-5-2 | None | 1415 | 2 | 2 | 1370 | 24 | 2 | 1320 | 90 |
| 1-5-4 | None | 1410 | 3 | - | - | - | - | - | - |
| 1-5-10 | None | 1445 | 0.2 | - | - | - | - | - | - |
| 1-6-2 | None | 1415 | 2 | 2 | 1370 | 24 | 2 | 1320 | 90 |
| 1-6-5 | None | 1415 | 3 | - | - | - | - | - | - |
| 1-6-9 | None | 1445 | 0.2 | - | - | - | - | - | - |

| | Gas Flow | Initial Temp | Initial Hold (hrs) | Cooling (°C/hr) | Intermediate Temp | Intermediate Hold (hrs) | Cooling (°C/hr) | Final Temp | Final Hold (hrs) |
|---|-------------|-----------------|--------------------------|--------------------|----------------------|----------------------------|--------------------|------------|------------------------|
| <u>CL intensity experiments</u> | | | | | | | | | |
| 224SAM-Eu | Ar | 1405 | 1 | 2 | 1375 | 24 | 2 | 1320 | 24 |
| CMAS2-2-Ti | None | 1420 | 1 | 2 | 1375 | 24 | 2 | 1350 | - |
| CMAS2-2-Eu | None | 1420 | 1 | 2 | 1375 | 24 | 2 | 1350 | - |
| CMAS2-2-Mn | Ar | 1405 | 1 | 2 | 1375 | 24 | 2 | 1320 | 24 |
| CMAS2-2-Ge | Ar | 1405 | 1 | 2 | 1375 | 24 | 2 | 1320 | 24 |
| <u>²²⁶Ra partitioning experiment</u> | | | | | | | | | |
| 2b-1*-FUSE | AG1 | 1450 | 1.5 | - | - | - | - | - | - |
| 2b-1*-1 (Ra-free) | Air | 1415 | 2 | 2 | 1375 | 24 | 2 | 1310 | 55 |
| 2b-1*-Ra | AG1 | 1410 | 1 | 2 | ~1380 | 24 | 2 | ~1330 | 30 |

REFERENCES

- Allred, A.L. (1961) Electronegativity values from thermochemical data. *Journal of Inorganic and Nuclear Chemistry*, 17, 215-221.
- Anderson, O. (1915) The system anorthite-forsterite-silica. *American Journal of Science*, 39, 407-454.
- Armstrong, J.T. (1988) Quantitative analysis of silicate and oxide materials: Comparison of Monte Carlo, ZAF, and $\phi(\rho z)$ procedures. In D.E. Newberry, Ed. *Microbeam Analysis*, p. 239-246. San Francisco Press.
- Bagnall, K.W. (1957) *Chemistry of the rare radioelements: polonium-actinium*. 177 p. Academic Press Inc., New York.
- Beattie, P. (1994) Systematics and energetics of trace-element partitioning between olivine and silicate melts: Implications for the nature of mineral/melt partitioning. *Chemical Geology*, 117, 57-71.
- Beattie, P.D., Drake, M., Jones, J., Leeman, W., Longhi, J., McKay, G., Nielsen, R., Palme, H., Shaw, D., Takahashi, E., and Watson, B. (1993) Terminology for trace-element partitioning. *Geochimica et Cosmochimica Acta*, 57, 1605-1606.
- Beatty, D.W., and Albee, A.L. (1980) Silica solid solution and zoning in natural plagioclase. *American Mineralogist*, 65, 63-74.
- Beckett, J.R. (2002) Role of basicity and tetrahedral speciation in controlling the thermodynamic properties of silicate liquids, Part I: The system CaO-MgO-Al₂O₃-SiO₂. *Geochimica et Cosmochimica Acta*, 66, 93-107.
- Beckett, J.R., and Stolper, E. (2000) The partitioning of Na between melilite and liquid; Part I, The role of crystal chemistry and liquid composition. *Geochimica et Cosmochimica Acta*, 64, 2509-2517.
- Bedard, J.H. (2005) Partitioning coefficients between olivine and silicate melts. *Lithos*, 83, 394-419.
- . (2006) Trace element partitioning in plagioclase feldspar. *Geochimica et Cosmochimica Acta*, 70, 3717-3742.
- Berman, R.G. (1983) A thermodynamic model for multicomponent melts, with application to the system CaO-MgO-Al₂O₃-SiO₂. Ph.D. Thesis, University of British Columbia.
- Berman, R.G., and Brown, T.H. (1984) A thermodynamic model for multicomponent melts, with application to the system CaO-Al₂O₃-SiO₂. *Geochimica et Cosmochimica Acta*, 48, 661-678.
- . (1987) Development of models for multicomponent melts: Analysis of synthetic systems. In I.S.E. Carmichael, and H.P. Eugster, Eds. *Thermodynamic modeling of geological materials: minerals, fluids, and melts*, 17, p. 405-442. Mineralogical Society of America.
- Bindeman, I.N., and Davis, A.M. (2000) Trace element partitioning between plagioclase and melt: Investigation of dopant influence on partition behavior. *Geochimica et Cosmochimica Acta*, 64, 2863-2878.
- Bindeman, I.N., Davis, A.M., and Drake, M.J. (1998) Ion microprobe study of plagioclase-basalt partition experiments at natural concentration levels of trace elements. *Geochimica et Cosmochimica Acta*, 62, 1175-1193.

- Bindeman, I.N., Davis, A.M., and Wickham, S.M. (1999) 400 my of basic magmatism in a single lithospheric block during cratonization: Ion microprobe study of plagioclase megacrysts in mafic rocks from Transbaikalia, Russia. *Journal of Petrology*, 40, 807-830.
- Blundy, J., and Dalton, J. (2000) Experimental comparison of trace element partitioning between clinopyroxene and melt in carbonate and silicate systems, and implications for mantle metasomatism. *Contributions to Mineralogy and Petrology*, 139, 356-371.
- Blundy, J., and Wood, B. (1994) Prediction of crystal-melt partition coefficients from elastic moduli. *Nature*, 372, 452-454.
- . (2003a) Mineral-melt partitioning of uranium, thorium and their daughters. In B. Bourdon, G.M. Henderson, C.C. Lundstrom, and S.P. Turner, Eds. *Uranium-series geochemistry*, 52, p. 59-123. Mineralogical Society of America.
- . (2003b) Partitioning of trace elements between crystals and melts. *Earth and Planetary Science Letters*, 210, 383-397.
- Blundy, J.D., Falloon, T.J., Wood, B.J., and Dalton, J.A. (1995) Sodium partitioning between clinopyroxene and silicate melts. *Journal of Geophysical Research*, 100, 15,501-15,515.
- Blundy, J.D., and Shimizu, N. (1991) Trace element evidence for plagioclase recycling in calc-alkaline magmas. *Earth and Planetary Science Letters*, 102, 178-197.
- Blundy, J.D., and Wood, B.J. (1991) Crystal-chemical controls on the partitioning of Sr and Ba between plagioclase feldspar, silicate melts, and hydrothermal solutions. *Geochimica et Cosmochimica Acta* 55, 193-209.
- Blundy, J.D., Wood, B.J., and Davies, A. (1996) Thermodynamics of rare earth element partitioning between clinopyroxene and melt in the system CaO-MgO-Al₂O₃-SiO₂. *Geochimica et Cosmochimica Acta*, 60, 359-364.
- Bocanegra, R., and Hopke, P.K. (1988) Radon adsorption on activated carbon and the effect of some airborne contaminants. *The Science of the Total Environment*, 76, 193-202.
- Boussieres, G. (1958) Radium. In P. Pascal, Ed. *Nouveau traite de chimie minerale*, IV, p. 931-955. Masson et Cie, Paris.
- Brenan, J.M., Shaw, H.F., Ryerson, F.J., and Phinney, D.L. (1995) Mineral-aqueous fluid partitioning of trace elements at 900°C and 2.0GPa: Constraints on the trace element chemistry of mantle and deep crustal fluids. *Geochimica et Cosmochimica Acta*, 59, 3331-3350.
- Brice, J.C. (1975) Some thermodynamic aspects of the growth of strained crystals. *Journal of Crystal Growth*, 28, 249-253.
- Bruno, E., and Facchinelli, A. (1974) Experimental studies on anorthite crystallization along the join CaAl₂Si₂O₈-SiO₂. *Bulletin de la Société Française de Minéralogie et de Cristallographie* 97, 422-432.
- . (1975) Crystal-chemical interpretation of crystallographic anomalies in lunar plagioclases. *Bulletin de la Société Française de Minéralogie et de Cristallographie* 98, 113-117.
- Bryan, W.B. (1974) Fe-Mg relationships in sector-zoned submarine basalt plagioclase. *Earth and Planetary Science Letters*, 24, 157-165.

- Cherniak, D.J. (2002) Ba diffusion in feldspar. *Geochimica et Cosmochimica Acta*, 66, 1641-1650.
- Colson, R.O., and Gust, D. (1989) Effects of pressure on partitioning of trace elements between low-Ca pyroxene and melt. *American Mineralogist*, 74, 31-36.
- Condomines, M., Gauthier, P.-J., and Sigmarrsson, O. (2003) Timescales of magma chamber processes and dating of young volcanic rocks. In B. Bourdon, G.M. Henderson, C.C. Lundstrom, and S.P. Turner, Eds. *Uranium-Series Geochemistry*, 52, p. 125-174. Mineralogical Society of America.
- Condomines, M., Gauthier, P.J., Tanguy, J.C., Gertisser, R., Thouret, J.C., Berthommier, P., and Camus, G. (2005) ^{226}Ra or $^{226}\text{Ra}/\text{Ba}$ dating of Holocene volcanic rocks: application to Mt. Etna and Merapi volcanoes. *Earth and Planetary Science Letters*, 230, 289-300.
- Condomines, M., Tanguy, J.-C., and Michaud, V. (1995) Magma dynamics at Mt. Etna: constraints from U-Th-Ra-Pb radioactive disequilibria and Sr isotopes in historical lavas. *Earth and Planetary Science Letters*, 132, 25-41.
- Cooper, K.M., Goldstein, S.J., Sims, K.W.W., and Murrell, M.T. (2003) Uranium-series chronology of Gorda Ridge volcanism: new evidence from the 1996 eruption. *Earth and Planetary Science Letters*, 206, 459-475.
- Cooper, K.M., and Reid, M.R. (2003) Re-examination of crystal ages in recent Mount St. Helens lavas: Implications for magma reservoir processes. *Earth and Planetary Science Letters*, 213, 149-167.
- Cooper, K.M., Reid, M.R., Murrell, M.T., and Clague, D.A. (2001) Crystal and magma residence at Kilauea Volcano, Hawaii: ^{230}Th - ^{226}Ra dating of the 1955 east rift eruption. *Earth and Planetary Science Letters*, 184, 703-718.
- CRC. (1993-1994) *CRC Handbook of Chemistry and Physics*. CRC Press, Cleveland, OH.
- Davies, R.H., Dinsdale, A.T., Chart, T.G., Barry, T.I., and Rand, M.H. (1990) Application of MTDATA to the modeling of multicomponent equilibria. *High Temperature Science*, 26, 251-262.
- Davis, A.M., Hashimoto, A., and Parsad, N. (1999) Trace element fractionation during evaporation in reducing atmospheres. *Lunar and Planetary Science Conference, XXX*, Houston, TX.
- De Capitani, C., and Brown, T.H. (1987) The computation of chemical equilibrium in complex systems containing non-ideal solutions. *Geochimica et Cosmochimica Acta*, 51, 2639-2652.
- DeVries, R.C., and Osborn, E.F. (1957) Phase equilibria in high-alumina part of the system $\text{CaO-MgO-Al}_2\text{O}_3\text{-SiO}_2$. *Journal of the American Ceramic Society*, 40, 6-15.
- Drake, M.J. (1976) Plagioclase-melt equilibria. *Geochimica et Cosmochimica Acta*, 40, 457-465.
- Drake, M.J., and Weill, D.F. (1975) Partition of Sr, Ba, Ca, Y, Eu^{2+} , Eu^{3+} , and other REE between plagioclase feldspar and magmatic liquid: An experimental study. *Geochimica et Cosmochimica Acta*, 39, 689-712.
- Dufek, J., and Cooper, K.M. (2005) $^{226}\text{Ra}/^{230}\text{Th}$ excess generated in the lower crust: Implications for magma transport and storage time scales. *Geology*, 33, 833-836.

- Duffy, J.A. (1993) A review of optical basicity and its application to oxidic systems. *Geochimica et Cosmochimica Acta*, 57, 3961-3970.
- Eugster, O., Armstrong, J.T., and Wasserburg, G.J. (1985) Identification of isobaric interferences-a computer-program for ion microprobe mass-spectral data. *International Journal of Mass Spectrometry of Ion Proceedings*, 66, 291-312.
- Feineman, M.D., and DePaolo, D.J. (2003) Steady-state $^{226}\text{Ra}/^{230}\text{Th}$ disequilibrium in mantle minerals: Implications for melt transport rates in island arcs. *Earth and Planetary Science Letters*, 215, 339-355.
- Fiske, P.S., and Stebbins, J.F. (1994) The structural role of Mg in silicate liquids: A high-temperature ^{25}Mg , ^{22}Na , and ^{29}Si NMR study. *American Mineralogist*, 79, 848-861.
- Fujinawa, A., and Green, T.H. (1997) Experimental study of partitioning of Hf and Zr between amphibole, clinopyroxene, garnet, and silicate melts. *Journal of Mineralogy, Petrology and Economic Geology*, 92, 69-89.
- Gaetani, G. (2004) The influence of melt structure on trace element partitioning near the peridotite solidus. *Contributions to Mineralogy and Petrology*, 147, 511-527.
- Geake, J.E., Walker, G., Telfer, D.J., Mills, A.A., and Garlick, G.F.J. (1973) Luminescence of lunar, terrestrial, and synthesized plagioclase, caused by Mn^{2+} and Fe^{3+} . *Proceedings of the Fourth Lunar and Planetary Science Conference*, 3, p. 3181-3189, Houston, TX.
- George, A.M., and Stebbins, J.F. (1998) Structure and dynamics of magnesium in silicate melts: A high-temperature ^{25}Mg NMR study. *American Mineralogist*, 83, 1022-1029.
- Ghiorso, M.S., and Sack, R.O. (1995) Chemical mass transfer in magmatic processes IV. A revised and internally consistent thermodynamical model for the interpolation and extrapolation of liquid-solid equilibria in magmatic systems at elevated temperatures and pressures. *Contributions to Mineralogy and Petrology*, 119, 197-212.
- Gibb, F.G.F. (1974) Supercooling and the crystallization of plagioclase from a basaltic magma. *Mineralogical Magazine*, 39, 641-653.
- Giletti, B.J., and Casserly, J.E.D. (1994) Strontium diffusion kinetics in plagioclase feldspars. *Geochimica et Cosmochimica Acta*, 58, 3785-3793.
- Gotze, J. (1998) Investigation of lunar plagioclases by cathodoluminescence microscopy and spectroscopy. *GSA Abstracts with Programs*, p. A-60.
- Gotze, J., Krbetschek, M.R., Habermann, D., and Wolf, D. (2000) High-resolution cathodoluminescence of feldspar minerals. In M. Pagel, V. Barbin, P. Blanc, and D. Ohnenstetter, Eds. *Cathodoluminescence in Geosciences*, p. 245-270. Springer-Verlag, Berlin, Heidelberg, New York, Tokyo.
- Halter, W.E., and Mysen, B.O. (2004) Melt speciation in the system $\text{Na}_2\text{O}-\text{SiO}_2$. *Chemical Geology*, 213, 115-123.
- Hashimoto, A. (1992) The effect of H_2O gas on volatilities of planet-forming major elements: I. Experimental determination of thermodynamic properties of Ca-, Al-, and Si-hydroxide gas molecules and its application to the solar nebula. *Geochimica et Cosmochimica Acta*, 56, 511-532.
- Hess, P.C. (1995) Thermodynamic mixing properties and the structure of silicate melts. In J.F. Stebbins, P.F. McMillan, and D.B. Dingwell, Eds. *Structure, Dynamics*

- and Properties of Silicate Melts, 32, p. 145-189. Mineralogical Society of America.
- Higuchi, H., and Nagasawa, H. (1969) Partition of trace elements between rock-forming minerals and the host volcanic rocks. *Earth and Planetary Science Letters*, 7, 281-287.
- Hill, E., Wood, B.J., and Blundy, J.D. (2000) The effect of Ca-Tschermaks component on trace element partitioning between clinopyroxene and silicate melt. *Lithos*, 53, 203-215.
- Hirschmann, M.M., and Ghiorso, M.S. (1994) Activities of nickel, cobalt, and manganese silicates in magmatic liquids and applications to olivine/liquid and to silicate/metal partitioning. *Geochimica et Cosmochimica Acta*, 58, 4109-4126.
- Hutcheon, I.D., Steele, I.M., Smith, J.V., and Clayton, R.N. (1978) Ion microprobe, electron microprobe and cathodoluminescence data for Allende inclusions with emphasis on plagioclase chemistry. *Proceedings of the Ninth Lunar and Planetary Science Conference*, 2, p. 1345-1368, Houston, TX.
- Ito, J. (1976) High temperature solvent growth of anorthite on the join $\text{CaAl}_2\text{Si}_2\text{O}_8\text{-SiO}_2$. *Contributions to Mineralogy and Petrology*, 59, 187-194.
- Johnson, M., Benziger, J., C., S., F., C., M., C., Darton, N., F., L., and Vogelaar, R.B. (1998) A ^{222}Rn source for low-background liquid scintillation detectors. *Nuclear Instruments and Methods in Physics Research Section A*, 414, 459-465.
- Kimata, M., Nishida, N., Shimizu, M., Saito, S., Matsui, T., and Arakawa, Y. (1995) Anorthite megacrysts from island arc basalts. *Mineralogical Magazine*, 59, 1-14.
- Kinzler, R.J., Grove, T.L., and Recca, S.I. (1990) An experimental study on the effect of temperature and melt composition on the partitioning of nickel between olivine and silicate melt. *Geochimica et Cosmochimica Acta*, 54, 1255-1265.
- Kirkpatrick, R.J. (1974) Kinetics of crystal growth in the system $\text{CaMgSi}_2\text{O}_6\text{-CaAl}_2\text{SiO}_6$. *American Journal of Science*, 274, 215-242.
- Klein, L., and Uhlmann, D.R. (1974) Crystallization behavior of anorthite. *Journal of Geophysical Research*, 79, 4869-4874.
- Kohn, S.C., and Schofield, P.F. (1994) The importance of melt composition in controlling trace-element behavior: An experimental study of Mn and Zn partitioning between forsterite and silicate melts. *Chemical Geology*, 117, 73-87.
- Kremser, D.T. *Advanced Topics in Probe for Windows*. *Probe for Windows* (32 bit) v. 5.35.
- Kushiro, I., and Walter, M.J. (1998) Mg-Fe partitioning between olivine and mafic-ultramafic melts. *Geophysical Research Letters*, 25, 2337-2340.
- Lange, R.L., and Carmichael, I.S.E. (1990) Thermodynamic properties of silicate liquids with emphasis on density, thermal expansion and compressibility. In J. Nicholls, and J.K. Russell, Eds. *Modern Methods of Igneous Petrology: Understanding Magmatic Processes*, 24. Mineralogical Society of America.
- LaTourrette, T. (1993) Experimental determination of U and Th partitioning between clinopyroxene, garnet, olivine, and natural and synthetic silicate melt. *Division of Geological and Planetary Sciences*, p. 373. California Institute of Technology, Pasadena, CA.

- LaTourrette, T., and Wasserburg, G.J. (1998) Mg diffusion in anorthite: Implications for the formation of early solar system planetesimals. *Earth and Planetary Science Letters*, 158, 91-108.
- Libourel, G. (1999) Systematics of calcium partitioning between olivine and silicate melts: Implications for melt structure and calcium content of magmatic olivines. *Contributions to Mineralogy and Petrology*, 136, 63-80.
- Libourel, G., Geiger, C.A., Merwin, L., and Sebald, A. (1992) ^{29}Si and ^{27}Al MAS-NMR spectroscopy of glasses in the system $\text{CaSiO}_3\text{-MgSiO}_3\text{-Al}_2\text{O}_3$. *Chemical Geology*, 96, 387-397.
- Linnen, R.L., and Keppler, H. (2002) Melt composition control of Zr/Hf fractionation in magmatic processes. *Geochimica et Cosmochimica Acta*, 66, 3293-3301.
- Lofgren, G. (1974a) An experimental study of plagioclase crystal morphology: Isothermal crystallization. *American Journal of Science*, 274, 243-273.
- . (1974b) Temperature induced zoning in synthetic plagioclase feldspar. In W.S. Mackenzie, and J. Zussmann, Eds. *The Feldspars*, p. 362-375. Manchester University Press, Manchester.
- Longhi, J., and Hays, J.F. (1979) Phase equilibria and solid solution along the join $\text{CaAl}_2\text{Si}_2\text{O}_8\text{-SiO}_2$. *American Journal of Science*, 279, 876-890.
- Longhi, J., Walker, D., and Hays, J. (1976) Fe and Mg in plagioclase. *Seventh Lunar Science Conference*, p. 1281-1300, Houston, TX.
- Mariano, A.N., Ito, J., and Ring, P.J. (1973) Cathodoluminescence of plagioclase feldspars. *GSA Abstracts with Programs*. 726.
- Mariano, A.N., and Ring, P.J. (1975) Europium-activated cathodoluminescence in minerals. *Geochimica et Cosmochimica Acta*, 39, 649-660.
- Marshall, D.J. (1988) *Cathodoluminescence of Geological Materials*. 146 p. Unwin Hyman, Boston.
- Merzbacher, C.I., Sherriff, B.L., Hartman, J.S., and White, W.B. (1990) A high-resolution ^{29}Si and ^{27}Al NMR study of alkaline-earth aluminosilicate glasses. *Journal of Non-Crystalline Solids*, 124, 194-206.
- Miller, S.A., Asimow, P.D., and Burnett, D.S. (2006) Determination of melt influence on divalent element partitioning between anorthite and CMAS melts. *Geochimica et Cosmochimica Acta*, 70, 4258-4274.
- Miller, S.A., Burnett, D.S., and Asimow, P.D. (2003) Experimental divalent element partitioning between anorthite and CAI melt. *Lunar and Planetary Science Conference XXXIV*, p. 1446, Houston, TX.
- Mills, K.C. (1993) The influence of structure on the physico-chemical properties of slags. *ISIJ International*, 33, 148-155.
- Momyer, F.F. (1960) *The radiochemistry of the rare gases*. 55 p. Subcommittee on Radiochemistry, National Academy of Sciences, National Research Council.
- Murakami, H., Kimata, M., Shimoda, S., Ito, E., and Sasaki, S. (1992) Solubility of $\text{CaMgSi}_3\text{O}_8$ and Si_4O_8 . *Journal of Mineralogy, Petrology and Economic Geology*, 87, 491-509.
- Mysen, B.O. (1997) Aluminosilicate melts: structure, composition, and temperature. *Contributions to Mineralogy and Petrology*, 127, 104-118.
- . (1999) Structure and properties of magmatic liquids: From haplobasalt to haploandesite. *Geochimica et Cosmochimica Acta*, 63, 95-112.

- . (2004) Element partitioning between minerals and melt, melt composition, and melt structure. *Chemical Geology*, 213, 1-16.
- Mysen, B.O., and Dubinsky, E.V. (2004) Melt structural control on olivine/melt partitioning of Ca and Mn. *Geochimica et Cosmochimica Acta*, 68, 1617-1633.
- Mysen, B.O., and Virgo, D. (1980) Trace element partitioning and melt structure: An experimental study at 1 atm pressure. *Geochimica et Cosmochimica Acta*, 44, 1917-1930.
- Mysen, B.O., Virgo, D., and Seifert, F.A. (1982) The structure of silicate melts: Implications for chemical and physical properties of natural magma. *Reviews of Geophysics and Space Physics*, 20, 353-383.
- Nakayama, Y., Nagao, H., Mochida, I., and Kawabuchi, Y. (1994) Adsorption of radon on active carbon. *Carbon*, 32, 1544-1547.
- Nielsen, R.L., and Dungan, M.A. (1983) Low pressure mineral-melt equilibria in natural anhydrous mafic systems. *Contributions to Mineralogy and Petrology*, 84, 310-326.
- O'Neill, H.S.C., and Eggins, S.M. (2002) The effect of melt composition on trace element partitioning: An experimental investigation of the activity coefficients of FeO, NiO, CoO, MoO₂ and MoO₃ in silicate melts. *Chemical Geology*, 186, 151-181.
- Onuma, N., Higuchi, H., Wakita, H., and Nagasawa, H. (1968) Trace element partitioning between two pyroxenes and the host lava. *Earth and Planetary Science Letters*, 5, 47-51.
- Osborn, E.F. (1942) The system CaSiO₃-diopside-anorthite. *American Journal of Science*, 240, 751-788.
- Osborn, E.F., DeVries, R.C., Gee, K.H., and Kraner, H.M. (1954) Optimum composition of blast furnace slag as deduced from liquidus data for the quaternary system CaO-MgO-Al₂O₃-SiO₂. *Transactions of the American Institute of Mining and Metallurgical Engineers*, 200, 33-45.
- Osborn, E.F., and Tait, D.B. (1952) The system diopside-forsterite-anorthite. *American Journal of Science*, 250A, 413-433.
- Pack, A., and Palme, H. (2003) Partitioning of Ca and Al between forsterite and silicate melt in dynamic systems with implications for the origin of Ca, Al-rich forsterites in primitive meteorites. *Meteoritics and Planetary Science*, 38, 1263-1281.
- Parrington, J.R., Knox, H.D., Brennan, S.L., Baum, E.M., and Feiner, R. (1996) Nuclides and isotopes: chart of the nuclides. 64 p. General Electric Co. and KAPL, Inc.
- Pauling, L. (1960) The nature of the chemical bond and the structure of molecules and crystals : An introduction to modern structural chemistry. 644 p. Cornell University Press, Ithaca, NY.
- Peters, M.T., Shaffer, E.E., Burnett, D.S., and Kim, S.S. (1995) Magnesium and titanium partitioning between anorthite and Type B CAI liquid: Dependence on oxygen fugacity and liquid composition. *Geochimica et Cosmochimica Acta*, 59, 2785-2796.
- Presnall, D.C., Gudfinnsson, G.H., and Walter, M.J. (2002) Generation of mid-ocean ridge basalts at pressures from 1 to 7 GPa. *Geochimica et Cosmochimica Acta*, 66, 2073-2090.
- Prince, A.T. (1954) Liquidus relationships on 10% MgO plane of the system lime-magnesia-alumina-silica. *Journal of the American Ceramic Society*, 37, 402-408.

- Prowatke, S., and Klemme, S. (2005) Effect of melt composition on the partitioning of trace elements between titanite and silicate melt. *Geochimica et Cosmochimica Acta*, 69(695-709).
- Purton, J.A., Allan, N.L., Blundy, J.D., and Wasserman, E.A. (1996) Isovalent trace element partitioning between minerals and melts: A computer simulation study *Geochimica et Cosmochimica Acta*, 60, 4977-4987.
- Purton, J.A., Blundy, J.D., and Allan, N.L. (2000) Computer simulation of high-temperature, forsterite-melt partitioning. *American Mineralogist*, 85, 1087-1091.
- Reagan, M.K., Volpe, A.M., and Cashman, K.V. (1992) ^{238}U - and ^{232}Th -series chronology of phonolitic fractionation at Mount Erebus, Antarctica. *Geochimica et Cosmochimica Acta*, 56, 1401-1407.
- Richter, F.M., Parsad, N., Davis, A.M., and Hashimoto, A. (1999) CAI cosmobarometry. Lunar and Planetary Science Conference XXX, Houston, TX.
- Rogers, N.W., Evans, P.J., Blake, S., Scott, S.C., and Hawkesworth, C.J. (2004) Rates and timescales of fractional crystallization from ^{238}U - ^{230}Th - ^{226}Ra disequilibria in trachyte lavas from Longonot volcano, Kenya. *Journal of Petrology*, 45, 1747-1776.
- Roskosz, M., Toplis, M.J., and Richet, P. (2005) Experimental determination of crystal growth rates in highly supercooled aluminosilicate liquids: Implications for rate-controlled processes. *American Mineralogist*, 90, 1146-1156.
- Ryerson, F.J., and Hess, P.C. (1978) Implication of liquid-liquid distribution coefficients to mineral-liquid partitioning. *Geochimica et Cosmochimica Acta*, 42, 921-932.
- Saal, A.E., and Van Orman, J.A. (2004) The ^{226}Ra enrichment in oceanic basalts: Evidence for melt-cumulate diffusive interaction processes within the oceanic lithosphere. *G³*, 5, doi:10.1029/2003GC000620.
- Schaefer, S.J., Sturchio, N.C., Murrell, M.T., and Williams, S.N. (1993) Internal ^{238}U -series systematics of pumice from the November 13, 1985 eruption of Nevado del Ruiz, Columbia. *Geochimica et Cosmochimica Acta*, 57, 1215-1219.
- Shannon, R.D. (1976) Revised effective ionic radii and systematic studies of interatomic distances in halides and chalcogenides. *Acta Crystallographica, A* 32, 751-767.
- Simon, S.B., Kuehner, S.M., Davis, A.M., Grossman, L., Johnson, M.L., and Burnett, D.S. (1994) Experimental studies of trace element partitioning in Ca, Al-rich compositions: anorthite and perovskite. *Geochimica et Cosmochimica Acta*, 58, 1507-1523.
- Simpson, J.J., and Grun, R. (1998) Non-destructive gamma spectrometric U-series dating. *Quaternary Geochronology*, 17, 1009-1022.
- Sims, K.W.W., Goldstein, S.J., Blincher-Toft, J., Perfit, M.R., Kelemen, P., Fornari, D.J., Michael, P., Murrell, M.T., Hart, S.R., DePaolo, D.J., Layne, G., Ball, L., Jull, M., and Bender, J. (2002) Chemical and isotopic constraints on the generation and transport of magma beneath the East Pacific Rise. *Geochimica et Cosmochimica Acta*, 66, 3481-3504.
- Singer, B.S., Dungan, M.A., and Layne, G.D. (1995) Textures and Sr, Ba, Mg, Fe, K, and Ti compositional profiles in volcanic plagioclase: Clues to the dynamics of calc-alkaline magma chambers. *American Mineralogist*, 80, 776-798.

- Slaby, E., and Gotze, J. (2004) Feldspar crystallization under magma-mixing conditions shown by cathodoluminescence and geochemical modeling—a case study from the Karkonosze pluton (SW Poland). *Mineralogical Magazine*, 68, 561-577.
- Smith, J.V., and Brown, W.L. (1988) *Feldspar Minerals*, Vol. 1. Springer-Verlag.
- Speit, B., and Lehmann, G. (1982) Radiation defects in feldspars. *Physics and Chemistry of Minerals*, 8, 77-82.
- Stebbins, J.F. (1995) Dynamics and structure of silicate and oxide melts: Nuclear magnetic resonance studies. In J.F. Stebbins, P.F. McMillan, and D.B. Dingwell, Eds. *Structure, Dynamics, and Properties of Silicate Melts*, 32, p. 191-246. Mineralogical Society of America, Washington, D.C.
- Steele, I.M., Peters, M.T., Shaffer, E.E., and Burnett, D.S. (1997) Minor element partitioning and sector zoning in synthetic and meteoritic anorthite. *Geochimica et Cosmochimica Acta*, 61, 415-423.
- Stirling, D., Duncan, A.M., Guest, J.E., and Finch, A.A. (1999) Petrogenesis of plagioclase phenocrysts of Mount Etna, Sicily, with particular reference to the 1983 eruption: Contribution from cathodoluminescence petrography. *Mineralogical Magazine*, 63, 189-198.
- Stolper, E., and Paque, J.M. (1986) Crystallization sequences of Ca-Al-rich inclusions from Allende: The effects of cooling rate and maximum temperature. *Geochimica et Cosmochimica Acta*, 50, 1785-1806.
- Telfer, D.J., and Walker, G. (1978) Ligand field bands of Mn^{2+} and Fe^{3+} luminescence centres and their site occupancy in plagioclase feldspars. *Modern Geology*, 6, 199-210.
- Toplis, M.J., and Corgne, A. (2002) An experimental study of element partitioning between magnetite, clinopyroxene and iron-bearing silicate liquids with a particular emphasis on vanadium. *Contributions to Mineralogy and Petrology*, 144, 22-37.
- Tsuchiyama, A. (1983) Crystallization kinetics in the system $CaMgSi_2O_6$ - $CaAl_2Si_2O_8$: The delay in nucleation of diopside and anorthite. *American Mineralogist*, 68, 687-698.
- Turner, S., Evans, P., and Hawkesworth, C. (2001) Ultrafast source-to-surface movement of melt at island arcs from ^{226}Ra - ^{230}Th systematics. *Science*, 292, 1363-1366.
- Turner, S.P., George, R., Jerram, D.A., Carpenter, N., and Hawkesworth, C. (2003) Case studies of plagioclase growth and residence times in island arc lavas from Tonga and the Lesser Antilles, and a model to reconcile discordant age information. *Earth and Planetary Science Letters*, 214, 279-294.
- Van Orman, J.A., Saal, A.E., Bourdon, B., and Hauri, E.H. (2006) Diffusive fractionation of U-series radionuclides during mantle melting and shallow-level melt-cumulate interaction. *Geochimica et Cosmochimica Acta*, 70, 4797-4812.
- van Westrenen, W., Allan, N.L., Blundy, J.D., Purton, J.A., and Wood, B.J. (2000) Atomistic simulation of trace element incorporation into garnets—comparison with experimental garnet-melt partitioning data. *Geochimica et Cosmochimica Acta*, 64, 1629-1639.
- van Westrenen, W., Blundy, J., and Wood, B. (1999) Crystal-chemical controls on trace element partitioning between garnet and anhydrous silicate melt. *American Mineralogist*, 84, 838-847.

- van Westrenen, W., Wood, B.J., and Blundy, J.D. (2001) A predictive thermodynamic model of garnet-melt trace element partitioning. *Contributions to Mineralogy and Petrology*, 142, 219-234.
- Vander Auwera, J., Longhi, J., and Duchesne, J.C. (2000) The effect of pressure on D_{Sr} (plag/melt) and D_{Cr} (opx/melt): Implications for anorthosite genesis. *Earth and Planetary Science Letters*, 178, 303-314.
- Vanko, D.A., and Laverne, C. (1998) Hydrothermal anorthitization of plagioclase within the magmatic/hydrothermal transition at mid-ocean ridges: examples from deep sheeted dikes (Hole 504B, Costa Rica Rift) and a sheeted dike root zone (Oman ophiolite). *Earth and Planetary Science Letters*, 162, 27-43.
- Volpe, A.M., and Hammond, P.E. (1991) ^{238}U - ^{230}Th - ^{226}Ra disequilibrium in young Mount St. Helens rocks: Time constraints for magma formation and crystallization. *Earth and Planetary Science Letters*, 107, 475-486.
- Voltaggio, M., Branca, M., Tedesco, D., Tuccimei, P., and Di Pietro, L. (2004) ^{226}Ra -excess during the 1631-1944 activity period of Vesuvius (Italy): a model of alpha-recoil enrichment in a metasomatized mantle and implications on the current state of the magmatic system. *Geochimica et Cosmochimica Acta*, 68, 167-181.
- Watson, B. (1976) Two-liquid partition coefficients: Experimental data and geochemical implications. *Contributions to Mineralogy and Petrology*, 56, 119-134.
- Watson, E.B., and Liang, Y. (1995) A simple model for sector zoning in slowly grown crystals: Implications for growth rate and lattice diffusion, with emphasis on accessory minerals in crustal rocks. *American Mineralogist*, 80, 1179-1187.
- Wood, B.J., and Blundy, J.D. (1997) A predictive model for rare-earth-element partitioning between clinopyroxene and anhydrous silicate melt. *Contributions to Mineralogy and Petrology*, 129, 166-181.
- (2001) The effect of cation charge on crystal-melt partitioning of trace elements. *Earth and Planetary Science Letters*, 188, 59-71.
- Yang, H.-Y., Salmon, J.F., and Foster, W.R. (1972) Phase equilibria of the join akermanite-anorthite-forsterite in the system CaO - MgO - Al_2O_3 - SiO_2 at atmospheric pressure. *American Journal of Science*, 272, 161-188.
- Zellmer, G., Turner, S., and Hawkesworth, C. (2000) Timescales of destructive plate margin magmatism: New insights from Santorini, Aegean volcanic arc. *Earth and Planetary Science Letters*, 174, 265-281.